ABSTRACT

ENSO FORCED CHANGES IN PRECIPITATION DISTRIBUTIONS AND RELATED GLOBAL CIRCULATION PATTERNS: GULF OF MEXICO REGION

by

Robert Munroe

July, 2010

Chair: Dr. Burrell Montz

Major Department: Geography

The El Nino Southern Oscillation (ENSO) forced precipitation is well documented in several regions around the world. Mid-latitude atmospheric circulations contribution towards extreme precipitation during ENSO is less well understood. One area that has a strong ENSO signal in extratropical and tropical storminess is the Gulf of Mexico. This region is influenced by high SSTs, the subtropical jet, and even polar intrusions. The objective of this research is to improve understanding of the link between ENSO, extreme precipitation, and the role of regional atmospheric circulations.

The probability density function, cumulative density function, Kolmogorov-Smirnov (KS) test and a hotspot analysis are employed to explore the independent and spatial statistics of precipitation distributions between phases of ENSO across the Gulf of Mexico region. The months of August through January are examined, but October and December display significant spatial patterns and are selected for a synoptic analysis of six grid boxes to represent five regions of large scale ENSO forcing. Our primary finding indicates subtropical jet stream winds are significantly different and stronger during El Nino, especially for the month of October. This

would suggest that El Nino would lead to more extremes throughout the Gulf of Mexico, which is not the case from the spatial autocorrelation analysis. Thus, other synoptic scale forcings must be at work. Differences in the cumulative distribution function (CDF) at lower rain rates seem to be more related to the strength and position of the polar jet and may be influenced by jet-interactions. Extreme precipitation during La Nina was traced to a weaker polar jet and the subtropical jet positioned away from the region of interest.

ENSO FORCED CHANGES IN PRECIPITATION DISTRIBUTIONS AND RELATED GLOBAL CIRCULATION PATTERNS: GULF OF MEXICO REGION

Presented to

The Faculty of the Department of Geography

East Carolina University

In Partial Fulfillment

of the Requirements for the Degree

Master of Arts in Geography

by

Robert Munroe

July, 2010

ENSO FORCED CHANGES IN PRECIPITATION DISTRIBUTIONS AND RELATED GLOBAL CIRCULATION PATTERNS: GULF OF MEXICO REGION

by

Robert Munroe

APPROVED BY:

DIRECTOR OF THESIS:_____

Dr. Scott Curtis

COMMITTEE MEMBER:_____

Dr. Ron L. Mitchelson

COMMITTEE MEMBER:_____

Dr. Jennifer Arrigo, PhD

CHAIR OF THE DEPARTMENT OF GEOGRAPHY:

_____

Dr. Burrell Montz, PhD

DEAN OF THE GRADUATE SCHOOL:

_____

Paul J. Gemperline, PhD

ACKNOWLEDGEMENTS

I would like to thank my advisor Dr. Scott Curtis for his tremendous support and guidance. I would also like to thank my friends and family whose support is instrumental in my success.

TABLE OF CONTENTS

LIST OF TABLES

LIST OF FIGURES

List of Equations

1. Introduction

The El Nino Southern Oscillation (ENSO) is an air-sea interaction over the Pacific Ocean. During an ENSO, anomalous sea surface temperatures (SST) and atmospheric circulations drive global climate change. In particular, changes in precipitation patterns frequently result in flooding and drought in various parts of the world that are detrimental to society.

Flooding can occur rapidly or over a few weeks. In contrast, a drought takes months or even years to develop and mature. This difference in spatial and temporal scales makes impacts difficult to trace back to the root atmospheric and oceanic mechanisms. The link between the ENSO in the Pacific to floods and droughts globally is an important teleconnection. The term teleconnection is used to describe changes in atmospheric circulations indirectly forced by distant sources such as the anomalous sea surface temperatures experienced during ENSO. Across longer time scales, ENSO explains some of the variation in precipitation patterns, in particular at low latitudes (e.g. Ropelewski and Halpert 1987, 1989, Curtis et al. 2007). Deviations in atmospheric circulations and sea surface temperatures (SST) during an ENSO event result in an increased tendency for extreme precipitation across certain regions of the world (e.g. Ropelewski and Halpert 1987, 1989, Curtis et al. 2007). For example, the Gulf of Mexico is one region that has experienced significant changes in the distribution of precipitation during the positive and negative phases of ENSO (e.g. Ropelewski and Halpert 1986, Gershunov and Barnett 1998, Curtis et al. 2007).

The following research questions are focused on gaining a better understanding of ENSO forced precipitation over the Gulf of Mexico.

1.1. Research Questions

1) What are the changes in precipitation distributions for ENSO events in the Gulf of Mexico region?

2) How do changes relate to:

a) characteristics of the subtropical jet streams

b) characteristics of polar jet streams

c) interaction of the jet streams

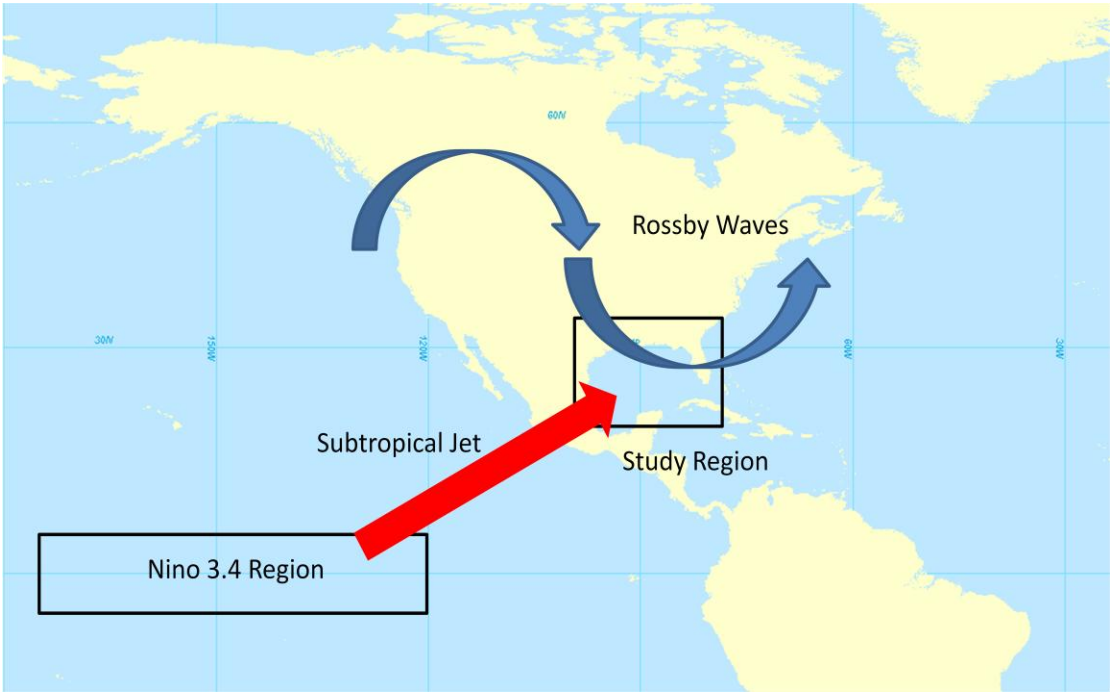

Figure 1. Schematic of Jet Stream Interaction and ENSO over the Study Area.

This schematic of the research design (Figure 1), describes the interaction of the subtropical and polar jet stream over the study region. The rectangle in the bottom left hand corner outlines the Nino 3.4 region, used to estimate ENSO.

2. Literature Review

There are close ties in existing research between ENSO and global warming, and the two climate phenomena have similar impacts. Both phenomena are accompanied by warming waters near the equator and exhibit an increase in extreme precipitation. Similar modifications to global circulations have also been suggested (e.g. Wentz et al. 2007, Allan and Soden 2008). In a similar capacity the global warming signal is suggested to be imbedded in the ENSO signal given the recent trend in the frequency, longevity, and intensity of the warm phase. However, this claim is difficult to verify. The Pacific Decadal Oscillation (PDO) (Mantua et al. 1997) forces anomalous sea surface temperatures, predominately in the northern Pacific, similar to ENSO (Zhang et al. 1997), but at higher latitudes. The PDO plays a significant role in a 20-30 year alternating trend of dominant positive and negative phases of ENSO. A positive PDO trend across the past several decades coincides with global warming. The positive phase of the PDO and global warming can explain the recent El Nino dominated trend. Consequently, isolation of the two signals is difficult.

Other studies suggest that ENSO and global warming impact global circulations in different ways. Some suggest that ENSO and global warming have an opposite impact on the Hadley Cell and midlatitude westerlies. These studies using ocean-atmospheric coupled models state that longitudinal warming of SSTs (ENSO alias) is responsible for Hadley Cell strengthening and contraction, while latitudinal warming (global warming alias) expands and weakens the Hadley Cell circulation while broadening and weakening the midlatitude westerlies (Lu et al. 2008, Gastineau et al. 2009). Some studies also suggest the frequency of extremes could increase. Understanding how this would impact precipitation distributions becomes a challenge, since spatial patterns of precipitation are likely to respond to changes in global

circulations. Despite possible dissimilarities between ENSO and global warming, ENSO has been used as an alias for global warming due to the similarities of sea surface temperatures (SST) near the equator. For this reason, research comparing the positive and negative phases of ENSO may also be applied towards the understanding of global climate change.

2.1 Precipitation

Precipitation provides valuable water resources. There are many different physical mechanisms in the atmosphere that produce precipitation, from small scale precipitation events, such as convectively driven thunderstorms, to large scale events such as tropical and extratropical cyclones. Regardless of the scale at which precipitation occurs, there are two main ingredients necessary to enable the process of precipitation. They are moisture and lift. The availability of moisture is sensitive to geographical location. For example, distance from large bodies of water, elevation, and latitude are important factors for seasonal precipitation over the long term. In addition to moisture, lift is necessary to produce clouds and precipitation. There are three lifting mechanisms; fronts, upslope flow over physical barriers, and convection.

2.1.1 Measurement

A traditional method of measuring precipitation is rain gauges. Gauges come in many shapes and forms from the relatively primitive wedge shaped gauges to the popular tipping buckets. Despite the many potential drawbacks of using rain gauges, it is still a direct, reliable form of measuring precipitation. Rain gauges also offer the capability of high resolution measurements both spatially and temporally. The one severe limitation is that rain gauge

networks are relatively sparse globally and only available over land with a strong bias towards dense population (Curtis et al. 2007).

More recent advancement in the understanding and production of satellite data has allowed for increasingly accurate precipitation estimates from space (Adler et al. 2003). The bird's eye viewpoint of satellites enables a nearly global coverage of data. Satellite derived precipitation datasets are void of common errors and biases found in measurements from rain gauges. However, a whole new set of errors and biases arise. The most noteworthy distinction between rain gauges and satellite estimated rainfall is that rain gauges measure precipitation directly, while satellites measure precipitation indirectly. Satellite data can use available gauge data to modify their algorithms. A second distinction lies in the point versus areal rainfall dilemma. Rain gauges offer point specific precipitation amounts while satellite data estimates precipitation across relatively large areas, adding a spatial component to precipitation estimates.

2.1.2 Physical Constraints

Beyond the physical properties of precipitation and its impact on humanity, it also acts as a tracer for climate modes (i.e. ENSO, PDO, etc.). The availability of nearly global satellite derived precipitation datasets has enabled scientists to pursue broader research questions. Such research endeavors include closing representations of the water budget and exploring trends in precipitation data. Precipitation is one of the climate variables used to describe changes in atmospheric circulations. The resulting precipitation tendencies are known as a signal. An ENSO signal is present across many parts of the world, implying a significant impact on global circulations.

Precipitation is an important part of the hydrologic cycle that not only provides invaluable water to humanity but also is an easily quantifiable aspect of the global climate system. As a result, it is often used as a parameter to assess climate sensitivity to global and regional circulations. Global climate models (GCM) are often dependent upon model oscillations in climate and climate change. GCMs are used to constrain different spatial, temporal, and physical parameters. Spatial and temporal constraints are chosen based on the scope of the problem being researched, available data, and computer resources and limitations. In particular, precipitation as a physical process is examined in a number of studies to observe and predict changes in climate (e.g. Allen and Ingram 2002, Wentz et al. 2007, Allan and Soden 2008). An example of a physical constraint includes the Clausius-Clapeyron's relationship with the atmosphere's ability to hold moisture in the form of water vapor. This relationship suggests that warming ocean surfaces will lead to a ~2 percent increase in precipitation per degree Kelvin at mid and high latitudes assuming little change in relative humidity (Allen and Ingram 2002).

2.2 The El Nino Southern Oscillation

The Southern Oscillation (SO), or see-saw in pressure between the East and West Pacific, was largely forgotten until the 1960s. In 1969, Bjerknes among others, revived interest in the SO. Bjerkness (1969) was a pioneer in realizing the air-sea interaction in the Pacific that today is known as the El Nino Southern Oscillation (ENSO). ENSO is forced by a coupling of the Pacific Ocean circulation and the Walker Circulation (Figure 2). During periods of neutral ENSO conditions, high pressure persists across the Eastern Pacific Ocean. Low pressure persists across the western Pacific Ocean. The sinking air from the subtropical high pressure feeds into the low

pressure at low levels, via low level east winds. The persistent winds act to pile up the warmest SST's into the western Pacific Ocean region. The warm waters and large scale low pressure create the ideal environment for widespread convection and precipitation. Across the eastern Pacific east winds create upwelling just offshore of the South American coastline. East winds spread the cold water originating from below the sea surface westward. The cold sea surface temperatures in combination with high pressure across the region result in the development of a strong inversion near the surface and sinking motion aloft.

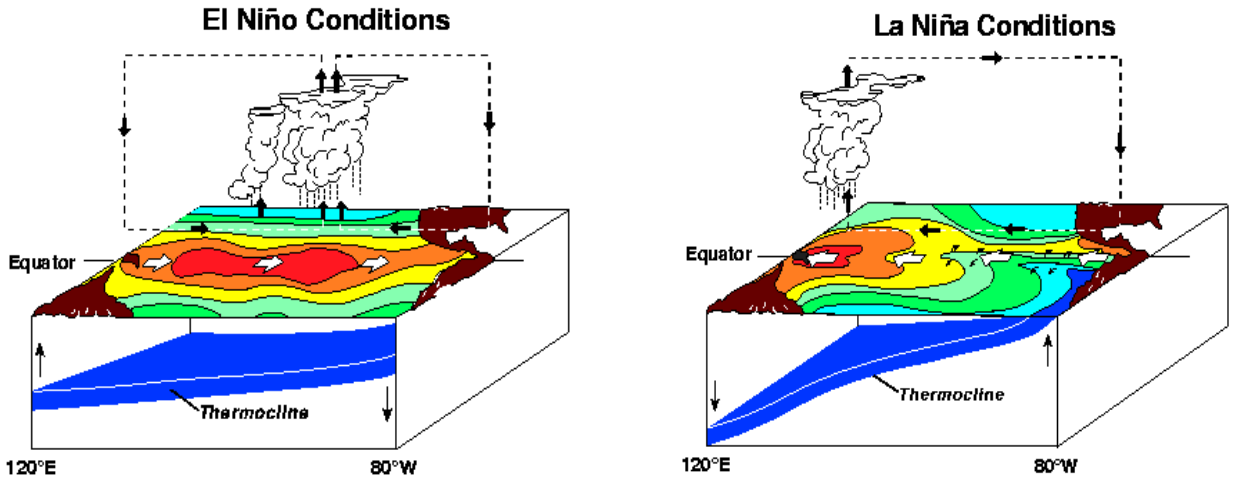

Figure 2. Walker Circulation during (1) El Nino (left) and (2) La Nina (right). (Images Courtesy of NOAA)

This combination is ideal for drought conditions across the region, confirmed by deserts across the western edge of South America. West winds aloft connect the upper level feature of the low and high pressure coupling. During the warm phase of ENSO the atmospheric circulations are weak leading to warm waters spreading eastward. During the cold phase of ENSO the atmospheric circulations are strong and the east-west gradients are magnified.

2.3 ENSO – Precipitation

A link between ENSO and global precipitation has been hypothesized ever since the discovery of the SO by Walker (1923). However, the relationship between ENSO and precipitation was largely ignored until the 1960s. Several studies through the early 1980s (e.g. Horel and Wallace 1981, Rasmusson and Carpenter 1982, Arkin 1982) further developed the conceptual model of ENSO through the exploration of global circulations to explain anomalous precipitation and temperature trends. Precipitation patterns in relation to ENSO were first placed into a geographic context in the mid 1980's.

Ropelewski and Halpert (1986) identified several regions of the United States with a significant ENSO signal through the use of harmonic vectors. Harmonic vectors use rank ordered monthly precipitation totals averaged over some number of ENSO events, which are aggregated together to create vectors with magnitude and direction. The direction refers to the time of greatest precipitation and the magnitude accounts for the amplitude of the ENSO signal. That analysis focused on the rank order of monthly total precipitation.

Of the regions identified, the ENSO signal in the southeast United States was shown to be the strongest. The central Rockies and the Ohio River Valley also experienced a significant precipitation effect according to Ropelewski and Halpert (1986). Ropelewski et al (1987, 1989) extended this study to the global scale. One severe limitation of these studies is the dependence upon available rain gauges. Since rain gauges are only available over land, two thirds of the Earth is immediately void of ENSO analysis. Of the remaining land mass, the availability of reliable rain gauges is strongly biased towards areas of dense, wealthy populations. However, these were the first studies to perform a comprehensive analysis of precipitation patterns globally in relation to ENSO. Ropelewski's research validated ENSO's far reaching influence.

Following the establishment of a global ENSO – precipitation relationship, several studies focused on improving and better understanding this relationship. For example, Gershunov and Barnett (1998) examined ENSO forced precipitation with a focus on the right tail (extreme precipitation) of the probability density function over the United States. Similarly, Cayan et al. (1999) examine the precipitation distribution relative to ENSO in the western United States.

Once the geography of ENSO forced precipitation was mapped out, more detailed questions remained related to the precipitation distributions. For instance, how does ENSO impact daily precipitation events? To answer this question and others, various aspects of the precipitation distributions are examined in a series of research papers.

Ropelewski and Halpert (1995) focused on the annual distribution of rainfall. The 10^{th}, 30^{th}, 50^{th} (median), 70^{th}, and 90^{th} percentiles were examined, and mean changes were noted during ENSO. Findings for the Gulf of Mexico and Northern Mexico suggest increased precipitation during the positive ENSO phase and decreased precipitation during the cold phase. Observed relationships were restricted to land due to the location of rain gauges.

Curtis et al. (2007) examined extreme precipitation defined larger than one standard deviation of the probability density function. Daily and monthly extremes were examined using TRMM (Huffman et al. 2007) satellite derived datasets. As indicated earlier, satellite data can be nearly global in coverage. Curtis et al. (2007) identify differences in precipitation trends over land, ocean, and both. Their results over the Gulf of Mexico were consistent with Ropelewski and Halpert (1995), but included the open waters.

Ropelewski and Bell (2008) focused on ENSO forced precipitation using median values of monthly ranked precipitation, suggesting that the entire precipitation distribution needs to be

studied. The study of changes in mean, variance, and standard deviation provide important information for precipitation distributions. Improving the resolution of GCMs requires more detailed information about the behavior of precipitation distributions (Ropelewski and Bell 2008).

2.4 Global Circulations

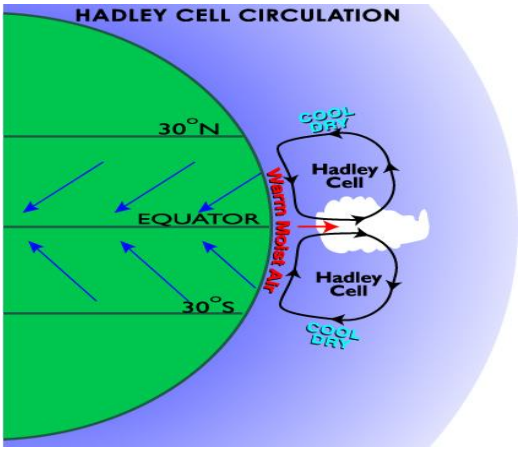

Figure 3. Hadley Cell Circulation. (Image courtesy of www.newmediastudio.org)

The Hadley Cell (Figure 3) is a nearly symmetric circulation centered near the equator. It is similar to the Walker circulation with respect to the high/low pressure coupling. A significant difference lies in the orientation and the scale of the Hadley Cell. The Hadley Cell is a meridional circulation that crosses the equator. It extends from the equator to the subtropics around the earth. The Hadley cell consists of rising air near the equator in the form of the Inter-Tropical Convergence Zone (ITCZ) and sinking air in the subtropics which result in the formation of subtropical high pressure. The circulation migrates seasonally.

The subtropical jet extends around the world in the subtropics at the poleward boundary of the Hadley cell (Held and Hou 1980). The subtropical jet is driven by angular momentum

transport from the deep tropics. The intensity and mean latitudinal position of the subtropical jet is proportional to the strength of the Hadley Cell (Lee and Kim 2003).

The mid-latitude westerlies, also known as the polar front, are baroclinic, eddy-driven zonal winds within the mid-latitudes. In the northern hemisphere the westerlies vary in latitude intra- and inter-seasonally. The largest variation occurs annually with the mean flow receding north and dissipating during the summer while strengthening and expanding southward during the winter. Potential vorticity advection and local baroclinicity are responsible for the progression and intensity of the polar front (Lee and Kim 2003, L'Heureux et al. 2006).

The mid-latitude westerlies are nearly symmetric about the equator suggesting that energy from the tropics transported by the Hadley Cell, and the subtropical jet explain much of the variation present in the mid-latitudes (e.g. Seager et al. 2003). Hoerling and Kumar (2003) demonstrate the symmetry about the equator using the 1998-2002 drought that impacted nearly every continent. They described the symmetry by examining the banding of subtropical highs exhibiting nearly a mirror image across the equator. This suggests a significant interaction between the Hadley Cell and the mid-latitude westerlies (e.g. Seager 2003, Hoerling and Kumar 2003).

Son and Lee (2005) find that the meridional width and gradient of the extratropical baroclinic zone impact the state of the jet stream. A strong temperature gradient generated by strong tropical heating and high latitude cooling produces a strong single jet. A more extensive meridional extra-tropical baroclinic zone that develops from weak tropical heating and strong high latitude cooling is favorable for a double jet state. The work of Son and Lee (2005) has important implications for understanding possible circulation trends during global warming.

Although not specified in Son and Lee (2005), it is not a stretch to employ some of these general findings towards possible ENSO induced changes in circulation.

2.4.1 North America

The mean climatology of the polar jet stream across North America is described by the Pacific-North American (PNA) Oscillation. The PNA neutral phase or mean climatology places a broad weak ridge across the eastern Pacific Ocean, into the western United States and across the United States Rockies into the high plains. A broad weak trough is typically prevails across the eastern half of the United States. A general trend for this pattern is increased precipitation and cooler temperatures in the vicinity of the trough and warmer drier conditions in the vicinity of the upper level ridge. An active subtropical jet stream typically extends from the tropical Pacific into the United States and/or Mexico. Interaction of the two jet streams increases the likelihood extratropical cyclone development and strengthening.

During the warm season, the polar jet stream recedes northward and weakens while the subtropical jet dissipates. As a result the polar and subtropical jets have a minimal impact in apparent weather across the United States into Mexico and the Gulf of Mexico. Diurnal convection over land, tropical cyclones, and occasional front's become the main drivers for precipitation across North America during the warm season.

2.5 ENSO – Global Circulation

The 1998-2002 global drought was forced by anomalously cold SSTs. It was, in fact a prolonged La Nina that is considered by Hoerling and Kumar (2003) to be the main driver for the global drought.

A significant feedback between the mid-latitude westerlies and the Hadley Cell during ENSO is the topic of several research papers (e.g. Lee and Kim 2003, Son and Lee 2005, Allan and Soden 2008). The general consensus is that warmer SSTs strengthen the Hadley Cell. An increased transport of moisture and angular momentum from the subtropical jet ensues as the Hadley Cell contracts equatorward (Lu et al. 2008, Gastineau et al. 2009). Baroclinicity and phasing of the two jets are the two mechanisms that enable a stronger polar front, equatorward of its mean position (Lee and Kim 2003). This energized polar front is likely to produce more precipitation as discussed in the following sub-section.

2.5.1 U.S. Southeast

Horel and Wallace (1980) find below normal atmospheric heights in the Southeast during El Nino. During El Nino, east coast cyclogenesis is favored, while during La Nina storm development and movement tends to occur further west over the Ohio River Valley (Eichler and Higgins 2006). Curtis (2006, 234) finds a similar trend, showing a concentration of extra-tropical cyclones near the east coast during El Nino events. Curtis (2006) finds that El Nino years have twice as many extra-tropical cyclones as either La Nina or neutral events over an entire winter season. This observation supports the theory that El Nino and its associated warming of SSTs strongly influences the mid-latitude westerlies. Curtis (2006) also finds that there are four times as many intense storms (lower than 1000 hPa in pressure) during El Nino years. In combination with the increased frequency, this provides further evidence of increased precipitation and increased extreme precipitation across the southeastern region during El Nino.

3. Data and Methodology

3.1 ENSO Index

ENSO is typically defined by averaged SST anomalies in the equatorial Pacific (Figure 4). The National Oceanic and Atmospheric Administration's (NOAA) Oceanic Nino Index (ONI) is used to reveal El Nino and La Nino events. ONI is defined as a three month floating mean of Nino 3.4 centered over the month for calculation. The Nino 3.4 region (Figure 4) extends from 120°W-170°W and 5°S- 5°N. An average value 0.5 over the three month period is defined as a positive (El Nino) and -0.5 as negative (La Nina) phase of ENSO, respectively. The months fitting this threshold for the ONI index are called ENSO months. Other studies such as Ropelewski et al. (1987, 1989) have used a five month average of SSTs and the variation of different Nino regions to define ENSO over longer time periods.

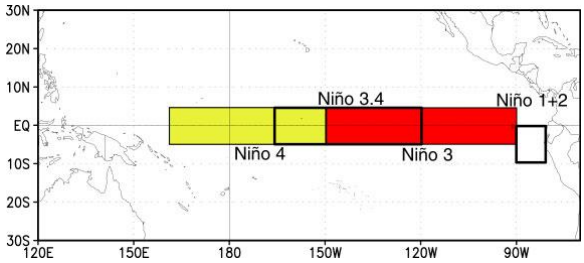

Figure 4. Nino Regions. Courtesy of NOAA.

Months that do not have three or more El Nino or La Nina events in the 12 year study period are discarded to control for sample size. February through July do not meet the requirements and are discarded. Neutral months are likewise discarded. The selected months (Table 1) are displayed below.

Month	El Nino	La Nina
August	97, 02, 04, 09	98, 99, 07
September	97, 02, 04, 06	98, 99, 07
October	97, 02, 04, 06	98, 99, 00, 07
November	97, 02, 03, 04 ,06	98, 99, 00, 07
December	97, 02, 04, 06	98, 99, 00, 05, 07, 08
January	98, 03, 05, 07	99, 00, 01, 06, 08, 09

Table 1. ENSO months.

3.2 Satellite Derived Datasets.

3.2.1 Geostationary Operational Environmental Satellite

The Geostationary Operational Environmental Satellite (GOES) is a geosynchronous orbiting satellite approximately 35,000 meters above the Earth. Its fixed position relative to the Earth's surface enables a nearly continuous full disc scan. The GOES consists of an imager and a sounder. The GOES imager is a five channel (one visible, four infrared) imaging radiometer designed to sense radiant and solar reflected energy from sampled areas of the Earth. The GOES sounder consists of nineteen channels (long to short wave infrared 1-18, and visible 19) designed to approximate vertical profiles of temperature and moisture. Additionally the GOES sounder estimates total precipitable water (TPW) and stability indices.

3.2.2 The Global Precipitation Climatology Project

The World Climate Research Program (WCRP) established the Global Precipitation Climatology Project (GPCP) with the goal of producing a new global precipitation product using available satellite datasets (WCRP 1986). The one degree daily (1DD) dataset is one product of the GPCP.

The 1DD dataset of the GPCP is a global dataset at a resolution of 1°x1° lat/lon grid. One degree daily is composed of the Threshold-Matched Precipitation Index (TMPI) with gaps filled by polar orbiting satellite sounding data. The TMPI product utilizes infrared radiometer data, collected by geostationary satellites with the best coverage between 40 degrees north and 40 degrees south. The GOES Precipitation Index (GPI: Arkin and Meisner 1987) is modified to approximate rainfall rates from satellite estimated cloud top temperatures in TMPI. The modification corrects for inconsistency between cloud top temperatures, precipitation estimates using the GPI, and observed/expected precipitation distributions. The indirect estimation of precipitation using infrared geo-stationary satellite data is not ideal. Measurement errors are unavoidable and are largest at fine scales. The Television and Infrared Observation Satellite (TIROS) Operational Vertical Sounder (TOVS) provides the pathfinder Path A dataset (Susskind et al. 1997). This main polar orbiting satellite data is merged with TMPI to produce the GPCP 1DD dataset (Huffman et al. 2001).

One drawback of the GPCP 1DD data is the relatively short period of available data when compared to its 2.5 degree resolution monthly counterpart. The 1DD dataset is only available from October 1996 until the present. As mentioned above, a distinct advantage of the GPCP 1DD dataset is the global extent and its relatively high resolution, both spatially and temporally. However it should be noted that the spatial averaging within the 1°x1° boxes, a symptom of gridded satellite data, might reduce the ENSO signal when compared to those derived from rain gauges (Ropelewski and Bell 2008).

3.3 Statistical Distributions

3.3.1 Cumulative Distribution Function

The cumulative distribution function (CDF example – Figure 5) is the running summation of a variable x, summed across all x from x-min to x-max until f(x) equals the total sum of all x. On the y-axis this total sum is represented by 1.0 or 100% (i.e. it's a relative distribution or density). In the example the F(x2) distribution (dashed line) is skewed to higher precipitation rates with ~80% of the distribution greater than x=1. This is far greater than F(x1) (solid line), where only 30% of the distribution is greater than x=1 (Figure 5).

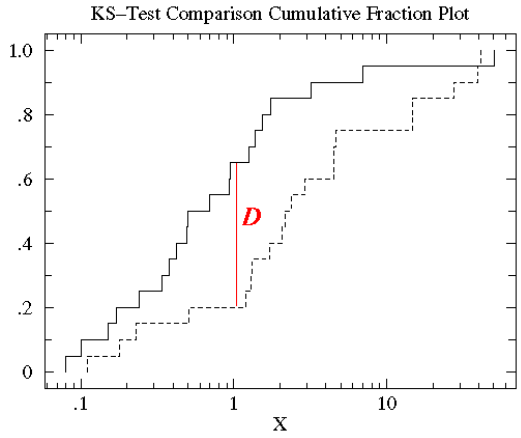

Figure 5. Cumulative Distribution Function - Calculation of D statistic.

3.3.2 Kolmogorov-Smirnov Test

The Kolmogorov-Smirnov (KS) test, examines the largest vertical differences between the cumulative distribution functions (CDF) of two variables. The difference of the two CDF functions is the D statistic (Figure 5). The D statistic is described by Equation 1, where D is the D statistic and S(x) represents each CDF function, N_1 and N_2.

Equation 1. The D Statistic.

$$D = \max_{(-\infty<x<\infty)} \left| S_{N1}(x) - S_{N2}(x) \right|$$

Thus, in Figure 5, D would equal approximately 0.5. The KS test compares two CDFs to determine if the two curves are significantly different. A D-statistic below a dynamic threshold, obtained from a lookup table for any month, at a given grid box, is used to determine the percent chance that the distributions are from the same population. The D-statistic lookup table requires information on the type of distribution (Gamma), the level of significance (5%), and the sample size (large n). The Gamma distribution provides the best fit for precipitation distributions.

3.3.3 Probability Distribution Function

The probability distribution function (PDF) graphs bin data (x-axis) against the frequency of occurrence of each bin occurring in a dataset (Figure 6). The area under the function is standardized to equal one and centered on the mean. Once this step is performed, any x-interval area under the curve represents the probability of observing that range of data. This is a normally standardized PDF (Figure 6). The PDFs used in this study are empirical.

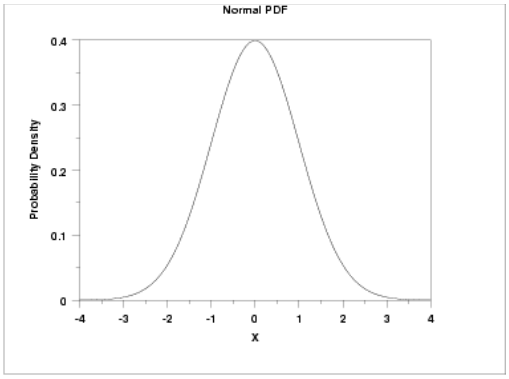

Figure 6. Probability distribution function.

3.4 Global Precipitation Plots

The global coverage of the GPCP 1DD dataset makes it a valuable input to create global precipitation plots (Figure 7). Similar to Curtis et al. (2006) a KS test is used to compare the two

monthly precipitation distributions, La Nina versus El Nino composites, calculated as La Nina minus El Nino, at each grid box, for each month, globally. Positive values (red) indicate the El Nino CDF is significantly different and has a larger proportion of heavy precipitation events than La Nina. Similarly, negative values (blue) indicate the La Nina CDF is significantly different and has a larger proportion of heavy precipitation events than El Nino. Additionally, contours of average precipitation differences (positive – negative phase of ENSO) are plotted at 1.0 mm/day increments to provide additional information on changes in average precipitation during ENSO. It should be noted that as expected there is a strong spatial correlation for both positive and negative D statistic values.

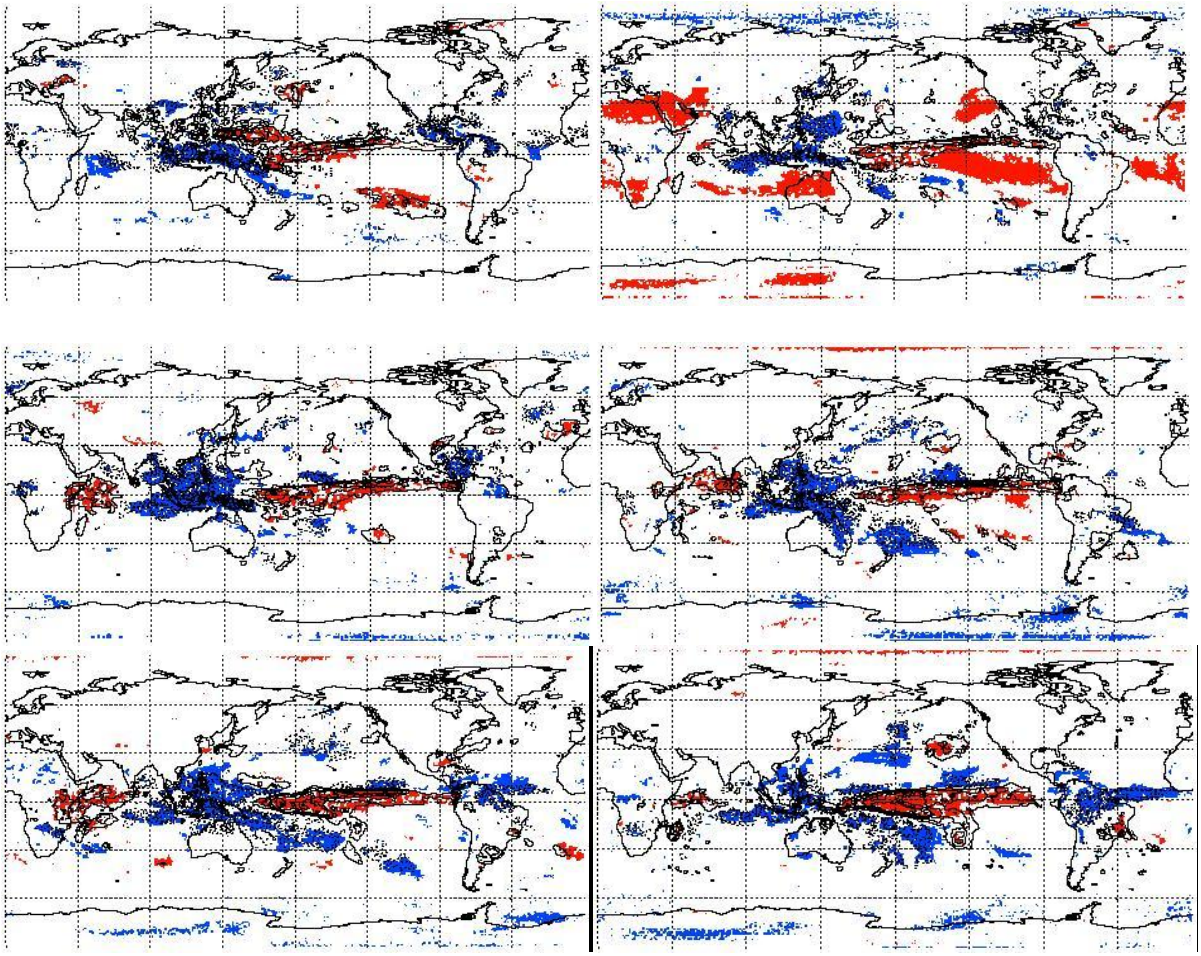

Figure 7. ENSO Monthly Precipitation KS Derived Signal. August – January from left to right, top to bottom. Red (blue) indicate that the La Nina CDF is larger (smaller) at D than the El Nino CDF. Solid (dashed) contours indicates that the mean rainfall is larger (smaller) for El Nino as compared to La Nina.

3.5 Region

Following the production of global precipitation plots, a study region is selected, based on several conditions:

-An ENSO signal is present.

-The region is at latitudes favorable for interactions with the subtropical and polar jet.

-Data availability.

-Support of literature.

Two regions are identified that meet these criteria, southern South America and the Gulf of Mexico region (Figure 8). Both regions possessed an ENSO signal during several of the months used in this study. They also are located at latitudes favorable for interactions with the subtropical and polar jets. Southern South America and the Gulf of Mexico are within 35 degrees north/south which is desirable for the most reliable TMPI rainfall estimates. Ropelewski and Halpert (1996) identify the Gulf of Mexico and Southern South America as regions impacted by ENSO using rain gauge data. Curtis et al. (2006) show an ENSO signal using GPCP and TRMM satellite derived precipitation data for the same regions.

The Gulf of Mexico is selected over South America for a few key reasons. Most notably, Ropelewski and Bell (2008) performed a similar study analyzing the ENSO signal in South America using rain gauge data. As a result, the Gulf of Mexico region (Figure 8) is selected to avoid redundancy. Additional considerations are related to the geographical relevance to the United States. Conveniently, this region is important to climate in the United States. Data availability and accessibility are improved for this region. Local knowledge of climate and synoptic weather patterns is another advantage in selecting the Gulf of Mexico.

Finally, earlier studies (Curtis 2006, Eichler and Higgins 2006) noted that extratropical storms are more abundant and stronger in the Gulf of Mexico during El Nino as compared to La Nina, yet little is understood about the controlling mechanisms, in particular the placement and strength of the polar jet and subtropical jet (see literature review). Thus, the study area selected extends from 20° to 35° N latitude and 75° to 100° W longitude.

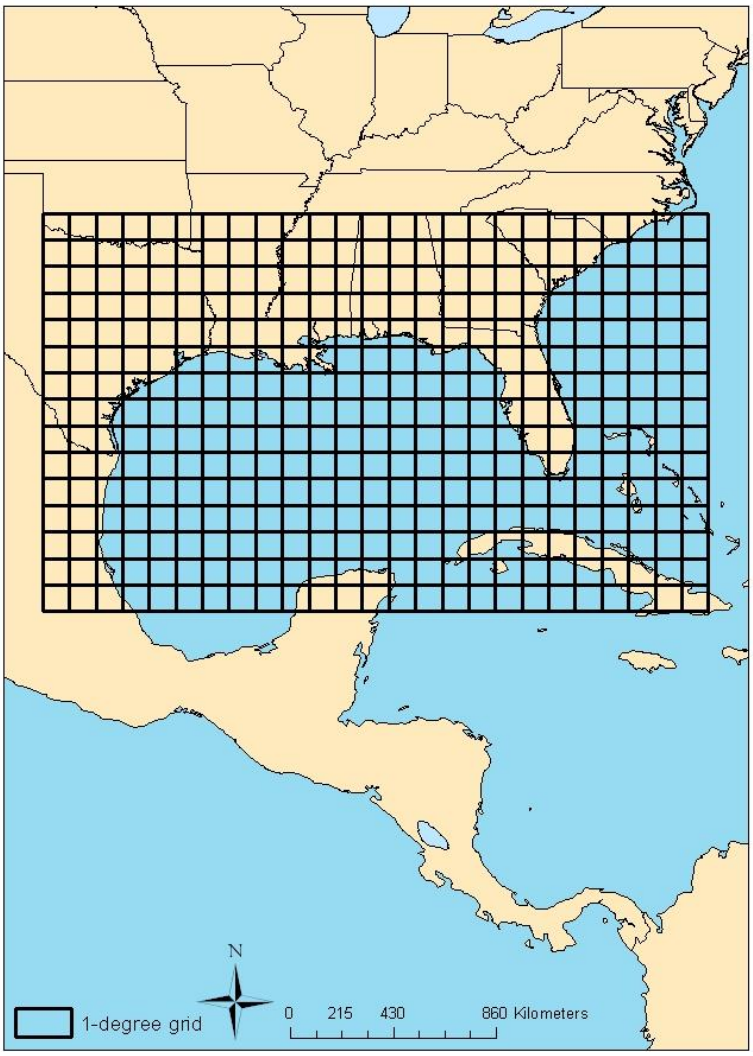

Figure 8. Gulf of Mexico Study Region. (20 – 35 ° N, 75 – 100 ° W), 1° Grid Superimposed.

3.6 Precipitation Distributions and Analysis

Interactive Data Language (IDL) software is used to examine the impact of ENSO on precipitation distributions. Intensity versus duration analysis is used to examine precipitation distributions**.** For clarity, bin size is defined as the period of time or window in which precipitation is accumulated as one event. The study region is made up of 375, 1°x1° grid boxes.

3.6.1 Intensity Versus Duration

The intensity/ duration method varies the time period of the bins of precipitation in order to extract precipitation anomalies occurring on different temporal and indirectly, spatial scales. This adds another dimension to the spatial analysis of precipitation distributions by analyzing the impact of different scales on precipitation distributions in the study region. Analysis of longer time scales beyond the temporal resolution of the 1DD dataset offers a more dynamic understanding of precipitation occurring at larger time and spatial scales. Bins used in this study are 24, 48, and 72 hours.

3.6.2 Bin Data Analysis

Precipitation events within the 24 hour bin (Equation 2) are examined using a similar methodology as the global precipitation plots discussed earlier to highlight differences in the precipitation distribution between El Nino and La Nina over the Gulf of Mexico. The native 1DD dataset 24 hour bin is chosen to represent synoptic scale precipitation. The 48 and 72 hour (Equations 3, 4) bin sizes (running total of 2 and 3 days of 1DD, respectively) are calculated in a similar manner. Although, due to the larger bin size, a moving window of the 48 and 72 hour bins is performed in order to increase the sample size and exhaust possible combinations of precipitation in each bin. The 48 and 72 hour bins are selected to represent synoptic scale precipitation events.

Equation 2: 24 Hour Precipitation Bin.

$D24_{ij} = EL24_{ij} - LA24_{ij}$

Where:
$EL24_{ij}$ = cumulative 24 hour rainfall values within cell i and month j
$LA24_{ij}$ = cumulative 24 hour rainfall values within cell i and month j
i = 1, 2, 3, … , 375 (in a 15*25 grid)
j = August, … , January

If $D24_{ij}$ >0, then El Nino has greater frequency of heavy events (wet El Nino)
<0, then La Nina has greater frequency of heavy events (wet La Nina)

Equation 3: 48 Hour Precipitation Bin.

$D48_{ij} = EL48_{ij} - LA48_{ij}$
Where:
$EL48_{ij}$ = cumulative 48 hour rainfall values within cell i and month j
$LA48_{ij}$ = cumulative 48 hour rainfall values within cell i and month j
i = 1, 2, 3, … , 375 (in a 15*25 grid)
j = August, … , January

If $D48_{ij}$ >0, then El Nino has greater frequency of heavy events (wet El Nino)
<0, then La Nina has greater frequency of heavy events (wet La Nina)

Equation 4: 72 Hour Precipitation Bin.

$D72_{ij} = EL72_{ij} - LA72_{ij}$

Where:
$EL72_{ij}$ = cumulative 72 hour rainfall values within cell i and month j
$LA72_{ij}$ = cumulative 72 hour rainfall values within cell i and month j
i = 1, 2, 3, … , 375 (in a 15*25 grid)
j = August, … , January

If $D72_{ij}$ >0, then El Nino has greater frequency of heavy events (wet El Nino)
<0, then La Nina has greater frequency of heavy events (wet La Nina)

3.6.3 Spatial Analysis

To supplement analysis of independent grid boxes, a hotspot analysis is performed to provide information on the spatial autocorrelation between grid boxes, beyond visual inspection. Accounting for the correlation or dependence between grid boxes will provide an improved understanding of the spatial distribution of significant precipitation. It may also offer a structure of values (large scale signal) to compare to ENSO and the synoptic scale forcing that impacts precipitation across the region. The method used is a hotspot analysis in the Geoda (Anselin 2006) statistical package using Univariate Local Indicators of Spatial Association (LISA) to analyze spatial autocorrelation of D values within the study region (Anselin, 2003). Hotspot analysis consists of positive and negative spatial autocorrelation. Positive spatial autocorrelation is a grouping of similar values. Conversely, negative positive spatial autocorrelation is a grouping of alternating or opposite values.

3.6.4 Exploratory Hot Spot Analysis

A combination of ArcMap and Geoda are used to produce and visualize a spatial analysis of the D values, monthly mean precipitation, and precipitation rates that occur at the D statistic for the KS test. Data is imported as a raster grid into ArcGIS from a text file. Each grid box is 1°x1°. Grid boxes were converted to vector polygons containing attribute values for rainfall in the form of D values. Then the converted data was used to perform a local spatial autocorrelation analysis established by the Local Moran LISA statistics (Equation 5) within the GeoDa statistical package.

Equation 5. Univariate LISA Statistic.

$$L_i = f(y_i, y_{ji})$$

For variable y_i observed at location i, where L_i is the LISA statistic

f describes a function such that y_{ji} are observed values in a neighborhood of j and i. A weighting scheme described later is used to define the neighborhood (Anselin, 1995).

After examining several weighting schemes in the Univariate LISA analysis, the Arc Distance Weight was selected. The Arc Distance Weight develops the spatial weights from the distance between the points on the grid. The Arc Distance Weight was used (rather than Euclidian) because the grid used is unprojected. For this study, two threshold values were analyzed; the values 64.72 and 100 miles. 64.72 miles is the default distance setting for GeoDa, which ensures that all cells have at least one neighbor included. The threshold value of 100 miles increases the cut-off distance (Anselin, 2003).

A Cluster Map (illustrated as a Chloropleth map), Significance Map, and Moran's I graph were produced to better understand the spatial autocorrelation of the cells. A Cluster Map shows four types of spatial autocorrelation: *high-high* and *low-low* which translates to clustering of similar values (positive spatial autocorrelation); *high-low* and *low-high* which shows spatial outliers (negative spatial autocorrelation). A Significance map shows significant Moran's I values with different shades of green. The Significance map is based on 999 randomized permutations, which provide a reference distribution for both the Significance map and the Moran's I graph. The Moran's I graph plots values of a variable against its neighbors (or weighted) values. A linear fit of these points provides the slope, which is the Moran's I value. The Moran's I graph has the same classifications as the Cluster Map. The *high-high* and *low-low* values represent positive spatial autocorrelation, and the *high-low* and *low-high* values represent negative spatial autocorrelation. A positive Moran's I value indicates positive spatial autocorrelation, while a negative value indicates negative spatial autocorrelation. Values near

zero suggest spatial independence or a random spatial distribution, signifying no significant relationship.

After the Univariate LISA statistics were calculated, the results were deposited into ArcMap and maps representing the Cluster and Significance maps were created.

3.6.5 Spatial Weight

This spatial analysis using Arc Distance Weight is executed 18 times in total, for the months of August through January at the 24, 48 and 72 hour bins (Equation 6) for D values and the rate of precipitation at D. The analysis is performed six times for mean precipitation.

Equation 6. Number of Hotspot Analysis Maps.

AUG SEP OCT NOV DEC JAN	**(6)**	*****	24 hr 48 hr 72 hr	**(3)**	**=**	**18 (MAPS)**

3.6.6 Grid Box Selection

Following this in depth analysis of independent and hotspot analysis patterns of the precipitation distributions related back to ENSO, several grid boxes are selected that meet a few criteria. Selected grid boxes must be independently and spatially significant at the five percent level for all three bin sizes (24, 48, and 72 hour). Independent D value maps are produced using the KS test, and hotspot analysis significance is determined using the univariate Local Indicator for Spatial Autocorrelation (LISA) hot spot analysis (as described earlier). Grid boxes with the largest KS derived D located at high precipitation rates are preferred during the selection process.

3.6.7 Precipitation Rates

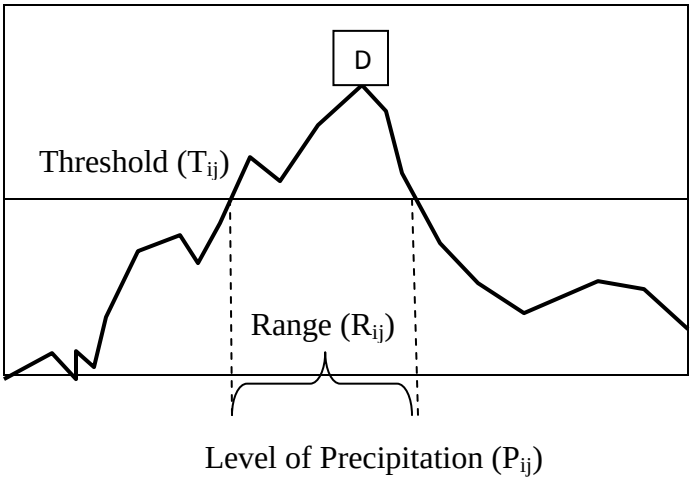

Figure 9. Absolute Value of the Difference of Two CDF Precipitation Distributions. El Nino and La Nina.

For each selected grid box (displayed later), precipitation rates of interest are selected for each bin size. The absolute value of the CDF ($Diff'24_{ij}$) is plotted and the range of precipitation rates are selected in the vicinity of the D statistic (Figure 9).

For example, a threshold value, T, of $|Diff'24_{ij}|$ is selected depending upon month and cell (usually between 0.2 and 0.5). Precipitation range, R, can then be used to identify events that make up a greater proportion of the distribution during El Nino/La Nina and may be responding to different drivers. As an illustration, suppose when it rains during an El Nino, 80% of the time it occurs at rates greater than 1 to 9 mm/day, while during a La Nina only 50% of the time it occurs beyond that range. This shift in the distribution means that the same rain rates are likely being caused by different preferential synoptic forcings during El Nino and La Nina. For purposes of discussion, imagine three distinctive outcomes in R values (Figure 10): low level precipitation differences between the two drivers (Type A), mid-level differences (Type B), and high level differences (Type C).

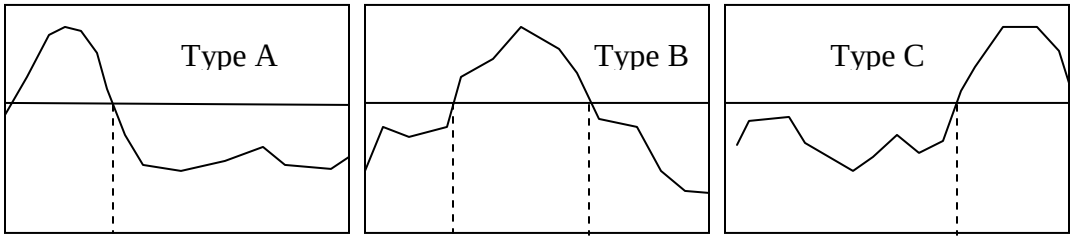

Figure 10. CDF. Low-Level(A), Mid-Level(B), and High-Level(C) Precipitation Ranges (Left to Right).

There are 18 possible outcomes for each cell (i) and month (j):

Diff'24_{ij} > 0, and Type A B or C; Diff'48_{ij} > 0 and Type A B or C; Diff'72_{ij} > 0 and Type A B or C
Diff'24_{ij} < 0, and Type A B or C; Diff'48_{ij} < 0 and Type A B or C; Diff'72_{ij} < 0 and Type A B or C

3.7 Synoptic Analysis

From the above analysis, the dates corresponding to the precipitation range (low-level, mid-level, and high-level) are selected for synoptic analysis. For selected dates, mean 24 hour 250 hPa wind velocities are acquired from the NCEP Reanalysis dataset (Kalnay et al. 1996) online. The Integrated Data Viewer (IDV) program is used to open and visualize streamlines and wind speed for synoptic analysis (Figure 11).

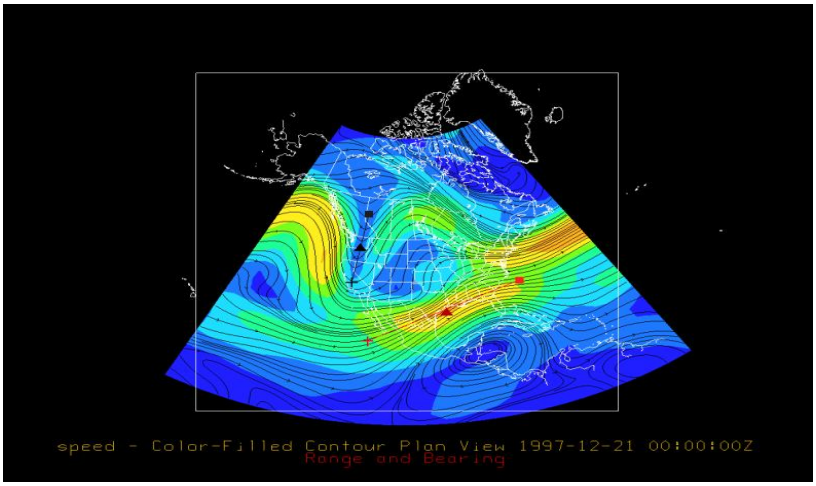

Figure 11. Jet stream analysis. Wind speed and streamlines.

The polar and subtropical jet features are treated differently due to difference in structural and physical processes that drive the two jets. The polar jet is analyzed at the nearest significant long wave trough or the trough that is most likely to influence the study region. Trough tilt provides tendencies of advection and trough movement. Typically a positive tilting trough is faster with weaker advection relative to a negatively tilted trough which is slower and has stronger temperature and moisture advection (Figure 12). Due to increased advection and divergence aloft, negatively tilted troughs are more favorable for developing stronger, slower moving extra-tropical cyclones which often result in more precipitation.

In this study the trough is measured from the center of the base of the trough toward cold air. The angle (in degrees) of this measurement and location at the base of the trough are recorded. The subtropical jet location and strength is measured at the maximum jet streak near the study area. The tilt is measured using the range and bearing tool across the length of the subtropical jet at this location. A manual query is performed to find maximum wind speeds (m/s) associated with either jet.

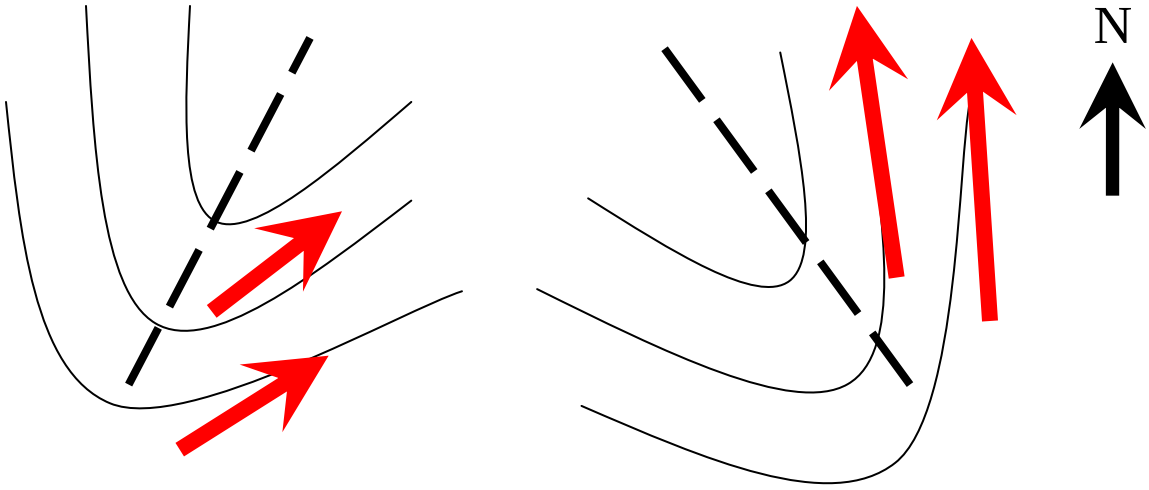

Figure 12. Trough Tilt. Positive (Left) and Negative (Right) Tilting Troughs (Dashed Lines). Black Curves are Isobars. Red Arrows Represent Temperature (Warm) and Moisture Advection.

3.7.1 Data Entry and Analysis

Jet stream tilt, strength, and location are entered in Microsoft Excel for each selected grid box and at each bin for El Nino and La Nina precipitation events. Once the data is entered, simple statistics are calculated on the data such as mean, median, max/ min, and standard deviation to search for patterns or deviations for the measures of the two jet streams. A T-Test is performed to further analyze between populations (El Nino versus La Nina) using a two tailed T-Test. The t-test describes the probability that two distributions are from the same population. A small value (value < 0.1) suggests that the jet stream circulations are responsible for similar precipitation events that occur at selected grid boxes. The grid boxes are chosen to represent a larger area with similar precipitation distributions as defined by the univariate LISA hotspot analysis.

4. Results

4.1 D Value Analysis

Independent grid box analysis of D values for each month at each bin is performed to display location and value of significant grid boxes. For this analysis, only grid boxes that have significantly different precipitation distributions between El Nino and La Nina at the five percent level are selected. Below are the maps of independent D values for each month, August through January (Figures 13-18). Even though D is defined as the absolute value of the maximum difference in CDF, since La Nina is consistently subtracted from El Nino, the sign is added for clarity. Thus, positive D values means that the La Nina histogram is weighted to having more

extremes and the negative D value means that the El Nino histogram is weighted to having more extremes.

4.1.1 August

The month of August (Figure 13) shows a relatively low number of significant grid boxes. At the 24 hour bin large and positive significant D values (more extreme precipitation in La Nina) are scattered in the southwest and south central areas of the study region. A few significant large and negative significant D values (more extreme precipitation in El Nino) occur north of the Gulf of Mexico. The same general trend can be said for the 48 and 72 hour bins. The spatial coverage of significant grid boxes expands considerably from the 24 to 48 and from the 48 to 72 hour bins.

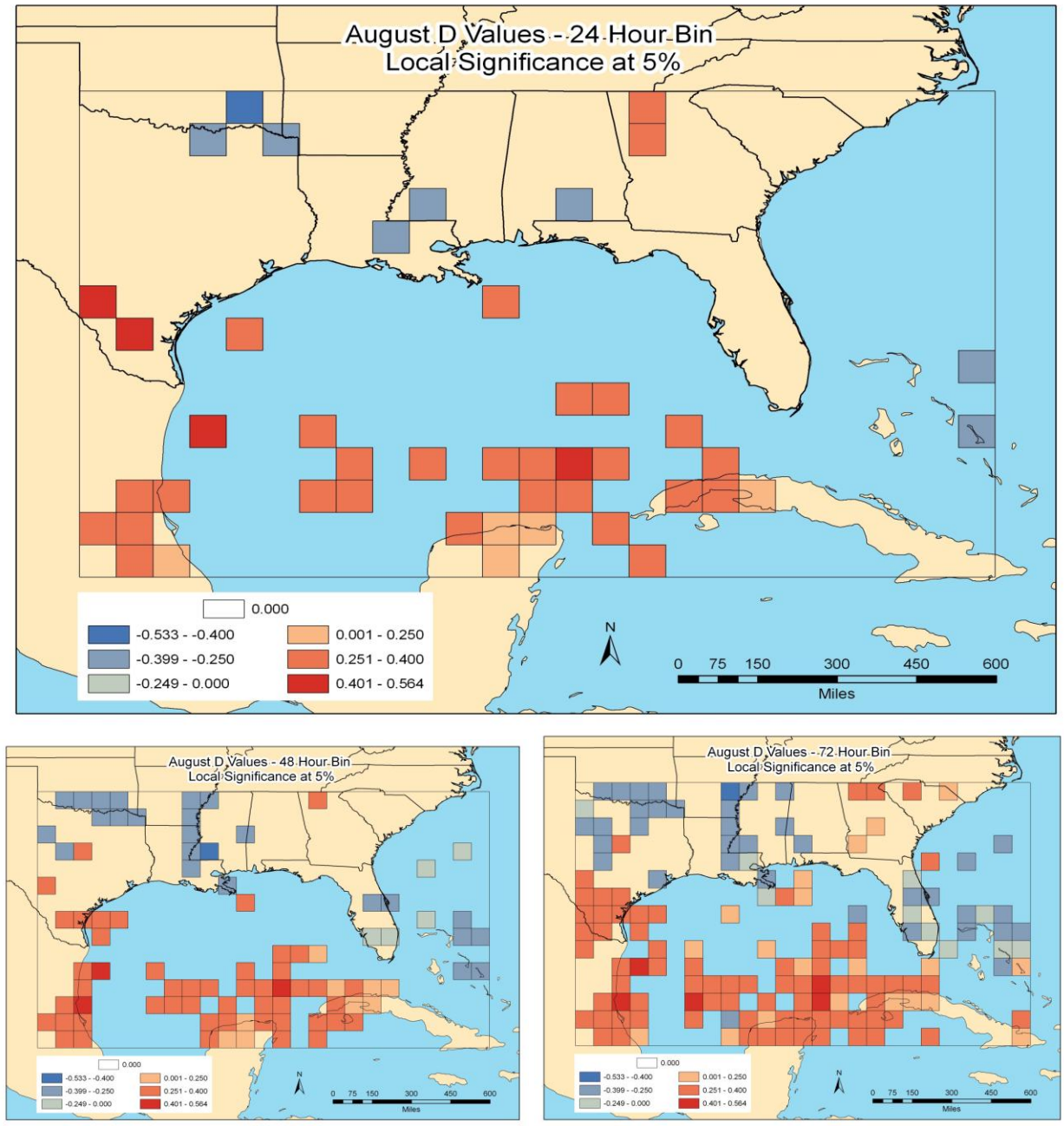

Figure 13. August D Values (Independent). 24, 48, and 72 hour bins (left to right). Red are positive D values (La Nina with more extremes) and blue are negative D values (El Nino with more extremes). The scale is the same for all maps.

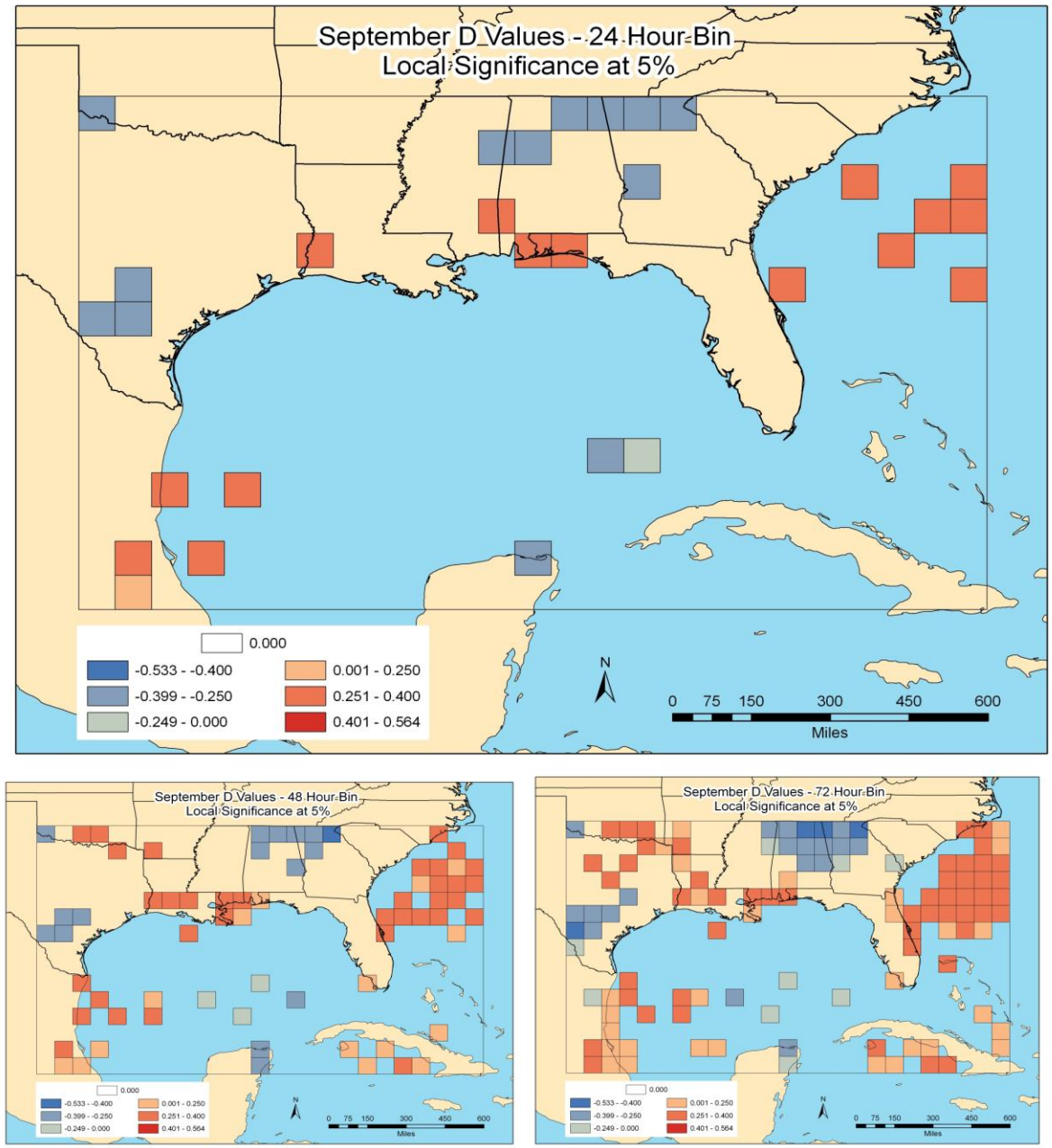

Figure 14. September D Values (Independent). 24, 48, and 72 hour bins (left to right). Red are positive D values (La Nina with more extremes) and blue are negative D values (El Nino with more extremes). The scale is the same for all maps.

4.1.2 September

September (Figure 14) also displays few significant grid boxes within the 24 hour bin. The only clear trends at this bin duration are a group of high values (more La Nina extreme precipitation) off the southeast coast of the United States and in the southwest corner of the study region with an area of negative values (more extreme precipitation in El Nino) in northern Alabama and Georgia. At the longer durations the aforementioned areas continue to expand, most notably off the southeast coast. Also a new area of positive values (more La Nina extreme precipitation) emerges in the northwest corner of the study region to Louisiana and along the Gulf coast into the western Panhandle of Florida. Another smaller area of high values (more extreme precipitation in La Nina) appears in the southeast corner of the study region. A small region of negative values is observed in southern Texas, especially at the 72 hour bin length. In addition to expanding areas of significant grid boxes, there is an increase in the number of grid boxes with large ($> |0.25|$) values of D.

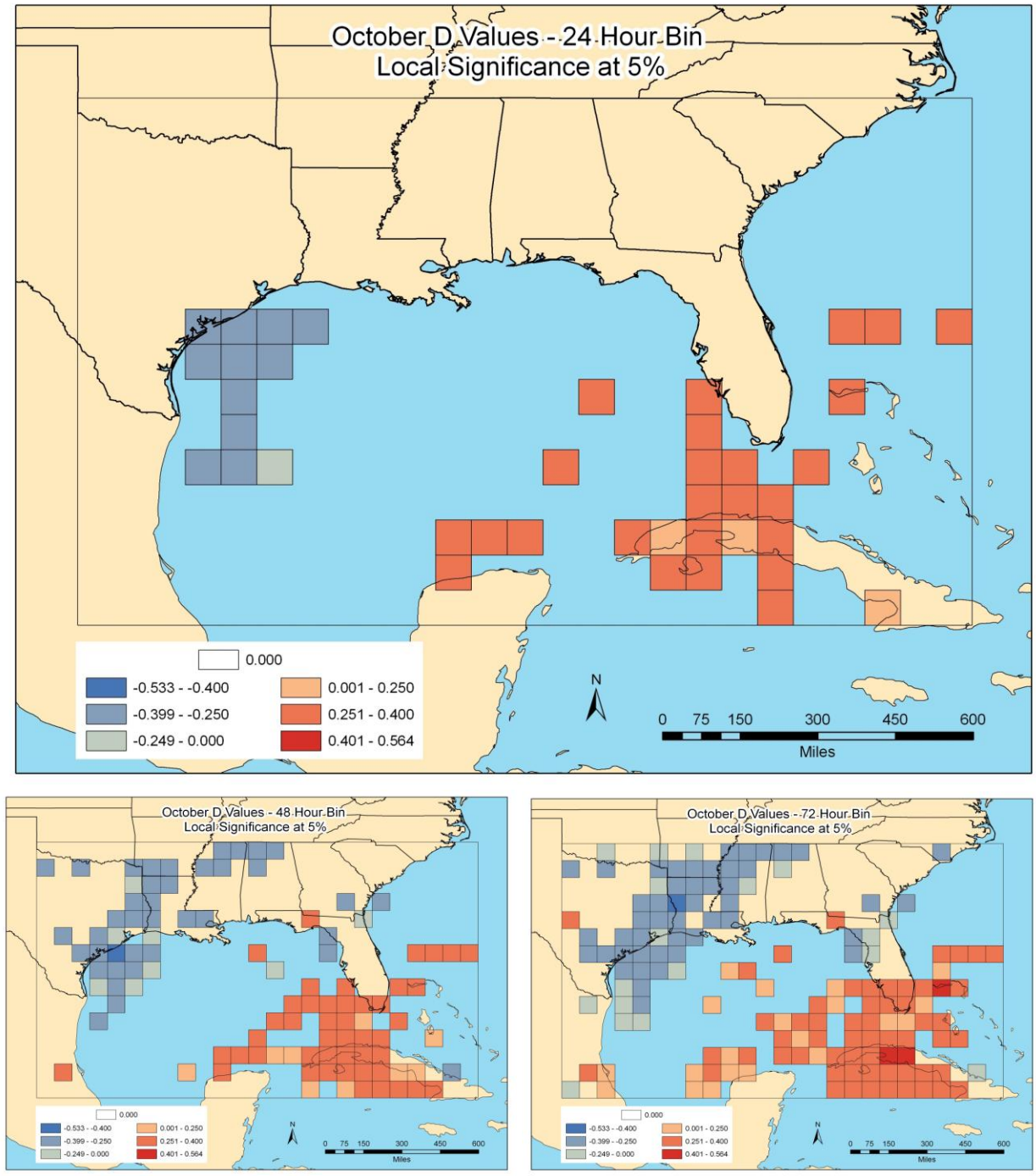

Figure 15. October D Values (Independent). 24, 48, and 72 hour bins (left to right). Red are positive D values (La Nina with more extremes) and blue are negative D values (El Nino with more extremes). The scale is the same for all maps.

4.1.3 October

The month of October (Figure 15) has a relative minimum in the number of grid boxes significant at the five percent level. Two concentrations of D values do emerge to form a dipole of D values across the Gulf of Mexico. In the southeast Gulf of Mexico high D values (more La Nina precipitation extremes) are close together suggesting substantial spatial organization. Similarly, negative D values (more El Nino extreme precipitation) in the northwest Gulf of Mexico are in close proximity. Important patterns to note moving to 48 and 72 hour bins are an expansion of the significant D values in and around the established dipole of D values and an expansion northward of the negative (more extreme precipitation during El Nino) values in particular from the northwest Gulf of Mexico into Texas, east to Alabama. Also note the appearance of negative values in northern Florida in the 48 and 72 hour analysis. Additionally, there is an increase in the absolute value of D at large bin lengths.

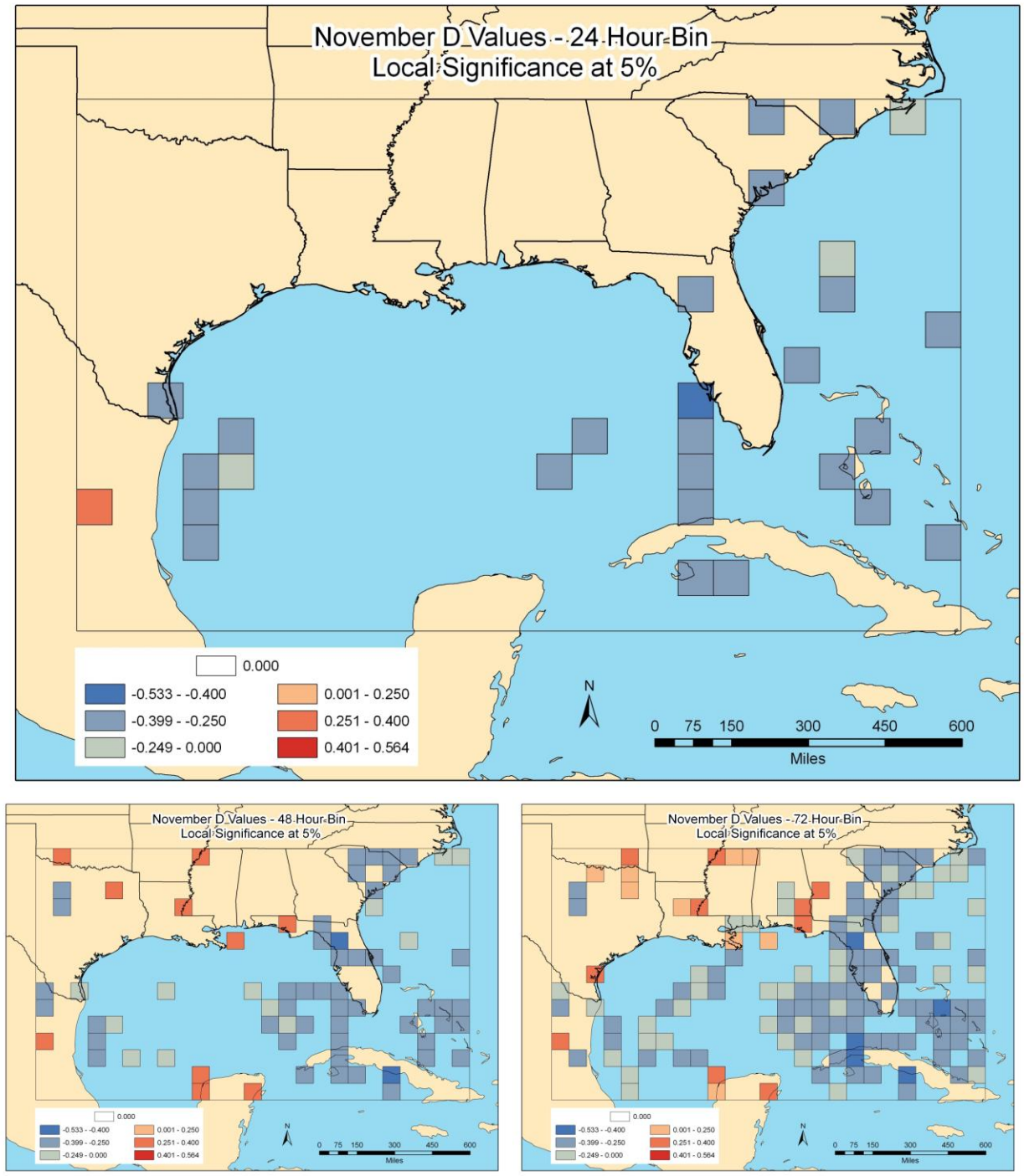

Figure 16. November D Values (Independent). 24, 48, and 72 hour bins (left to right). Red are positive D values (La Nina with more extremes) and blue are negative D values (El Nino with more extremes). The scale is the same for all maps.

4.1.4 November

November (Figure 16) has a relatively low number of significant grid boxes. Of the few significant grid boxes at the 24 hour bin length, only one is a positive D value (more extreme precipitation in La Nina). Most of the negative values are scattered from Cuba north to the Carolina's. The 48 and 72 hour bin length follow a similar trend with negative D values (more extreme precipitation in El Nino) concentrated, but expanding in the eastern half of the study region. Interestingly, at longer bin lengths there is a noticeable absence of significant D values off the southeast coast as compared to the southeast United States and Bahamas. This means that there is little change in precipitation distributions off the southeast coast during ENSO. In addition to expanding areas of significant grid boxes, there is an increase in the number of grid boxes with large (> |0.25|) values of D.

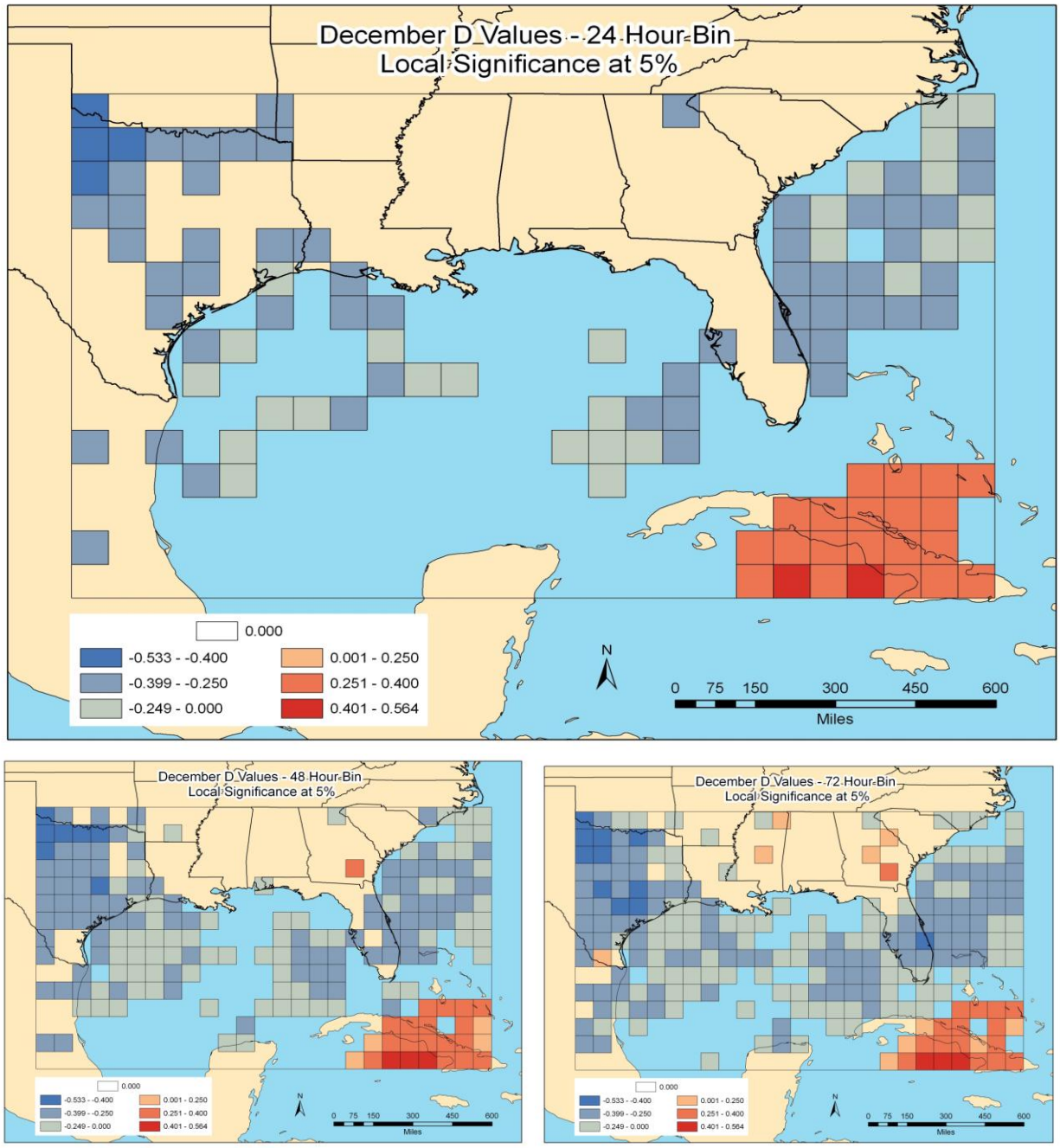

Figure 17. December D Values (Independent). 24, 48, and 72 hour bins (left to right). Red are positive D values (La Nina with more extremes) and blue are negative D values (El Nino with more extremes). The scale is the same for all maps.

4.1.5 December

December (Figure 17) conveys three main regions of significant D values. Positive values (more La Nina precipitation extremes) persist over the southeast portion of the study region, while negative values (more El Nino precipitation extremes) occur predominately from Texas into the northwest Gulf of Mexico and in a separate area from the eastern Gulf and in particular, off the southeast coastline. The same general trend is present into the 48 and 72 hour bins lengths. However, negative values expand in the 72 hour bin, allowing for D values to converge over the central Gulf of Mexico to result in a long swath of significantly negative D values (more extreme precipitation in El Nino) from Texas and northern Mexico east to the Atlantic Ocean. Additionally, large D (> |0.25|) values also increase in coverage. On the other hand, positive values in the southeast portion of the region remain largely unchanged at the 48 and 72 hour bins.

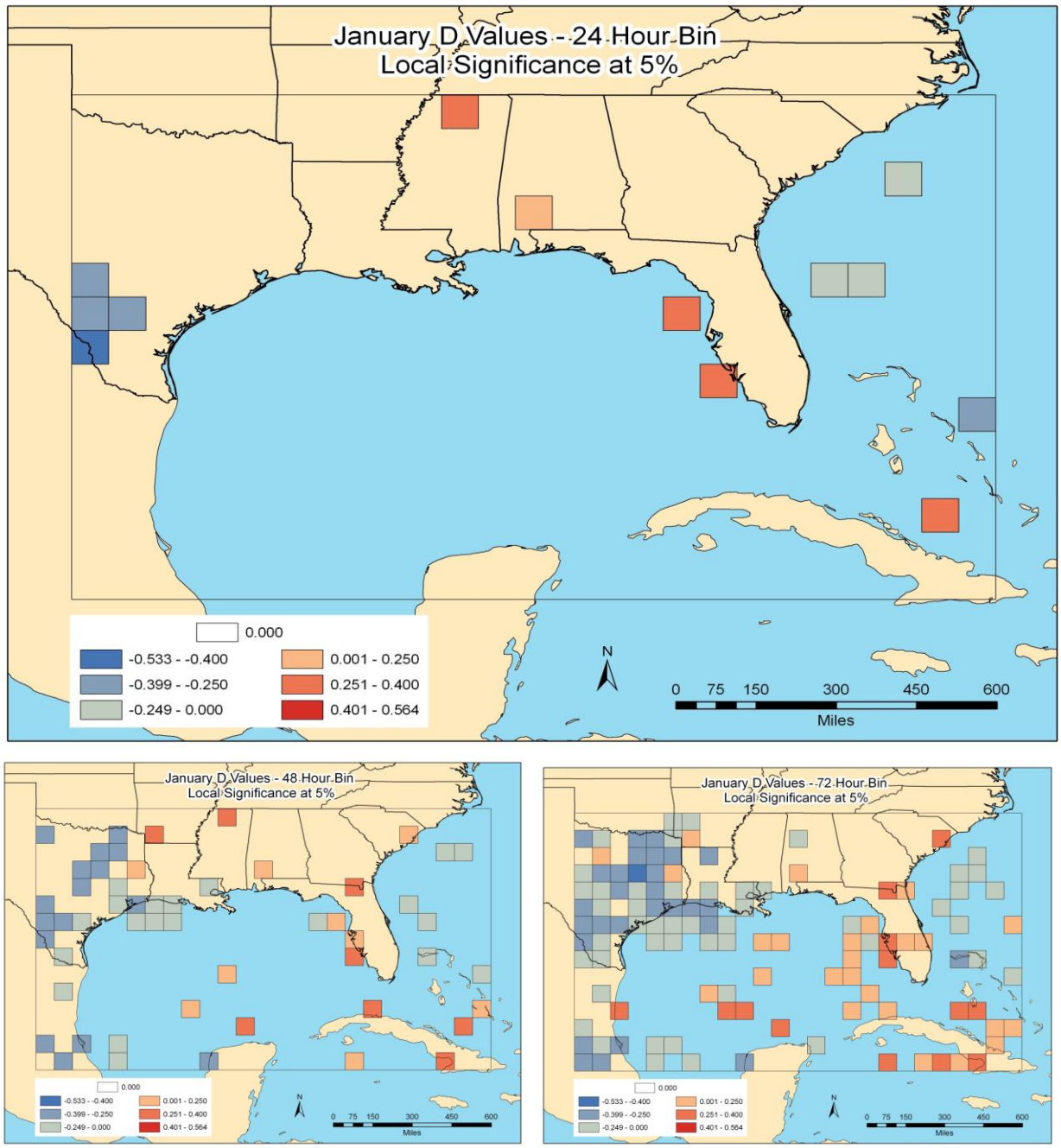

Figure 18. January D Values (Independent). 24, 48, and 72 hour bins (left to right). Red are positive D values (La Nina with more extremes) and blue are negative D values (El Nino with more extremes). The scale is the same for all maps.

4.1.6 January

The month of January (Figure 18) has the smallest number of significant boxes at all bins. A discernable large scale pattern cannot be determined at the 24 hour bin. At 48 hours, and in particular the 72 hour bin, show some spatial cohesion between grid boxes. Most notably, Texas is covered with negative D values (more La Nina extreme precipitation). All other patterns are weak and difficult to describe at best.

4.1.7 Independent Grid Box Summary

D value independent significance at 5 % displays a consistent pattern at larger bin lengths from 24 to 48 and 72 hours. The number of significant grid boxes at the 5 % level increases with increasing bin duration. A general trend shows the additional significant grid boxes are located in or near areas of concentrated significant grid boxes at 24 hours. Additionally, the number of significant boxes with low D values (-0.25 to 0.25) remain the same (August, September) or increase (October - January) at higher bins suggesting more widespread synoptic scale precipitation during October through January. A visual inspection suggests an organization spatially of locally significant grid boxes, which is supported by the spatial analysis of D values discussed at length in the next section.

August through December have a moderate to large number of significant grid boxes, especially at large bins. However, October, and in particular, December display the greatest consistency between bin lengths, improved spatial organization and a large number of significant grid boxes in general. All months except January, show a noticeable increase in the number of significant grid boxes with large D values (> |0.25|). Significant grid boxes with increasing D values over large scales suggest that there is a relationship with larger synoptic systems producing extremes as the time bin increases from 24 to 72 hours because larger storms cover a

larger area, often move slower and produce precipitation over longer periods of time. This also suggests a greater difference between ENSO precipitation distributions at the synoptic scale.

4.1.7.a D Value Trend

Looking at mean D values as a whole (Figure 19), there is a decreasing trend region-wide. In August and September mean D values are positive suggesting more La Nina extreme precipitation. In November and December a negative D value means that El Nino produces more extremes in general. Maximum positive values occur in August and September at a D value of around 0.05, with the minimum value at -0.15 in December. October and January have relatively neutral D values. Furthermore, for each month the average has a higher absolute value as the bin size increases from 24 to 72 hours. From August through January there is a decreasing trend in the standard deviation of D values (Figure 20), implying that there is less variation in D values and hence less variation in precipitation distributions during ENSO moving into the cold season. This is likely due to the expanding area of El Nino favored extreme precipitation (negative D values) moving into December. The standard deviation is also larger as the bin size increases.

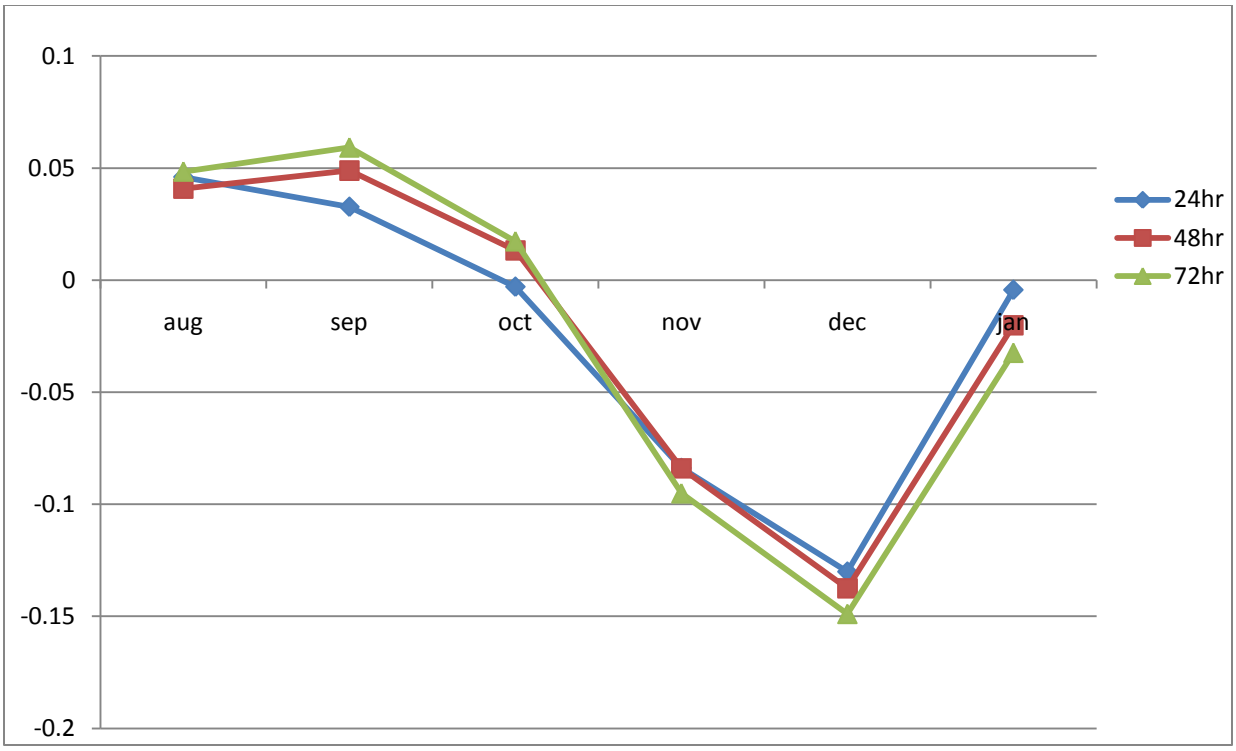

Figure 19. Monthly Mean D Values. 24, 48, and 72 Hour Bins.

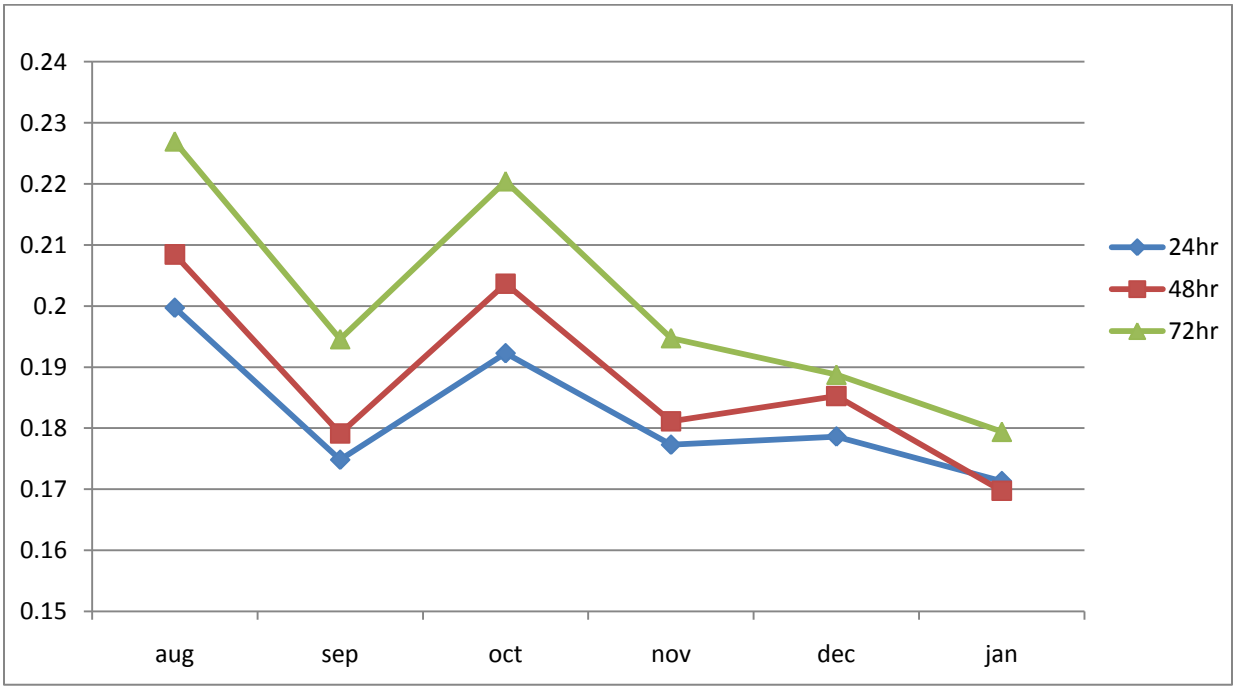

Figure 20. Monthly D Value Standard Deviations. 24, 48, and 72 Hour Bins.

4.2 Moran's I Values

As previously discussed in the methods section, the Moran's I is a linear fit between actual variable values and spatially weighted values. Values range from -1 to 1. Values correspond to negative (-1 to 0) and positive (0 to 1) autocorrelation in the study region. The further from 0, the stronger the positive or negative spatial autocorrelation with a value of 0 indicating no spatial autocorrelation using the assigned weighting scheme. The Moran's I values for each month at each bin and accompanying statistics (Table 2) demonstrate that the mean precipitation differences (La Nina minus El Nino months) show the strongest spatial autocorrelation. This is not surprising considering the mean state should be spatially smoother than any individual day (i.e. D value).

Month	Mean Diff.	D Values 24hr	48hr	72hr
AUG	0.775	0.580	0.615	0.610
SEP	0.788	0.549	0.577	0.662
OCT	0.872	0.688	**0.699**	**0.760**
NOV	0.778	0.474	0.500	0.496
DEC	**0.894**	**0.732**	0.682	0.730
JAN	0.772	0.459	0.554	0.509
Stats:				
Mean:	0.813	0.580	0.605	0.628
Min:	0.772	0.459	0.500	0.496
Max:	0.894	0.732	0.699	0.760
Range:	0.121	0.273	0.199	0.263

Table 2. Moran's I Values and Statistics. Largest values are bolded.

One consistency throughout all measures of spatial analysis is the largest absolute values of D occur in October and December. December has its largest values in the mean and 24 hour bins, while October has the largest values in the 48 hour and 72 hour bins. Interestingly, the

month in between, November has the lowest value in all D value spatial analyses and nearly the lowest value for the mean difference spatial analysis. This suggests that November could represent a transition month between two different synoptic forcings in fall (October) and winter (December) that lead to similar patterns of precipitation distribution. January has the next lowest Moran's I, followed by September, then August at the 24 hour bin. At longer bin lengths an interesting trend emerges. The months of August, November and January max out at the 48 hour bin. September and October increase by a fair margin at each bin, suggesting large spatial/ temporal scale patterns have a significant effect on the spatial organization of D values for those months. December is an outlier, in that the 24 and 72 hour bins represent approximately the same high Moran's I value, while the 48 hour bin marks a minimum. The mean statistic demonstrates that the Moran's I values increase with bin size. The 24 and 72 hour bins display the greatest range of Moran's I values, both 0.07 greater than the 48 hour bin range. This may suggest a greater monthly change in spatial patterns of precipitation at these scales during ENSO.

4.3 Hotspot Spatial Analysis

A hotspot spatial analysis provides evidence of the connectivity between grid boxes, while independent grid box analysis provided important grid box significance. A spatial analysis provides information on larger spatial patterns that could only be inferred using an independent grid box analysis of D values. A hotspot analysis of mean precipitation is produced to support the D value analysis. Mean precipitation plots are calculated at each grid box with the mean of La Nina minus El Nino. This is reversed to the typical El Nino minus La Nina difference, since a positive D value is nearly always associated with La Nina having more precipitation than El

Nino (see Fig. 7). The August through January mean precipitation difference and d value hotspot spatial analysis maps are displayed in the following (Figures 21-26).

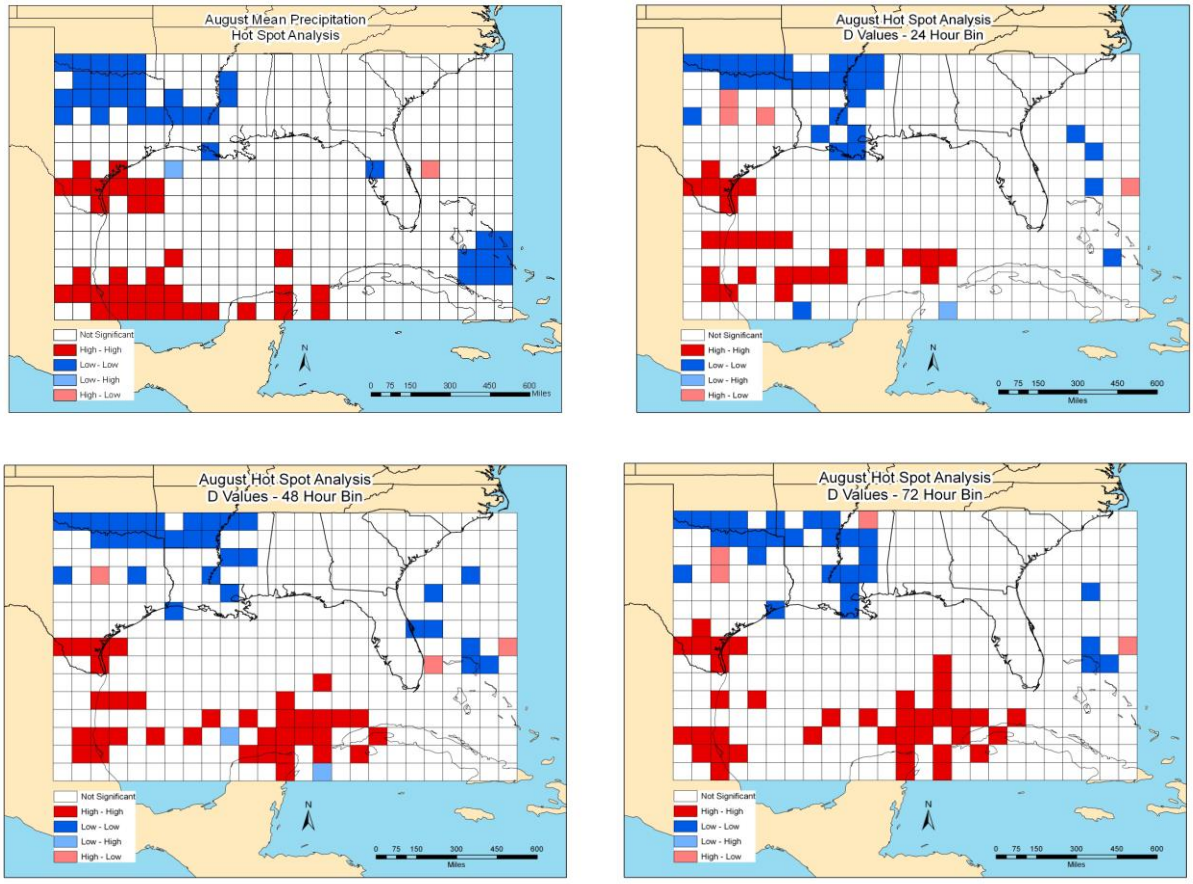

Figure 21 (left to right). August Hotspot Analysis of (1) Mean Precipitation; D Values at (2) 24 Hour, (3) 48 Hour, and (4) 72 Hour Bins.

4.3.1 August

4.3.1.a Mean Precipitation

The August mean precipitation map (Figure 21.1) reveals positive correlation in the form of low – low values (more El Nino extreme precipitation) in the northwest and southeast corners of the study region. Positive autocorrelation is also present in the form of high – high values (more La Nina extreme precipitation) in the south and southwest portion of the study region.

Additionally there is a small area of high – high values in southern Texas into the Gulf of Mexico.

4.3.1.b 24 Hour Bin

The August hot spot analysis of D values for the 24 hour bin (Figure 21.2) reveals a broad area of scattered high – high values (more La Nina extreme precipitation) across the southwest Gulf of Mexico. Low – low values (more El Nino extreme precipitation) are prevalent in northern Texas along the red river into portions of Louisiana and northern Mississippi. There are four scattered low – low values to the east of Florida. Note the small grouping of high – low values in the Dallas, TX area.

4.3.1.c 48 Hour Bin

The August hot spot analysis of D values for the 48 hour bin (Figure 21.3) shows similar patterns to the 24 hour bin. Noticeable differences include an expanding area of the high – high positive autocorrelation (more La Nina extreme precipitation) in the southeastern Gulf of Mexico and an expanding area of low – low values (more El Nino extreme precipitation) east of Florida.

4.3.1.d 72 Hour Bin

The 72 hour bin (Figure 21.4) displays somewhat similar patterns to the 24 and 48 hour bins. However, noticeable changes include a division of high – high values (more La Nina extreme precipitation) in the southwestern portion of the study region and a decrease in the spatial extent of low – low values (more El Nino extreme precipitation) east of Florida. This is intriguing, considering the general trend is for an increase in the spatial extent of positive autocorrelation at larger bin sizes.

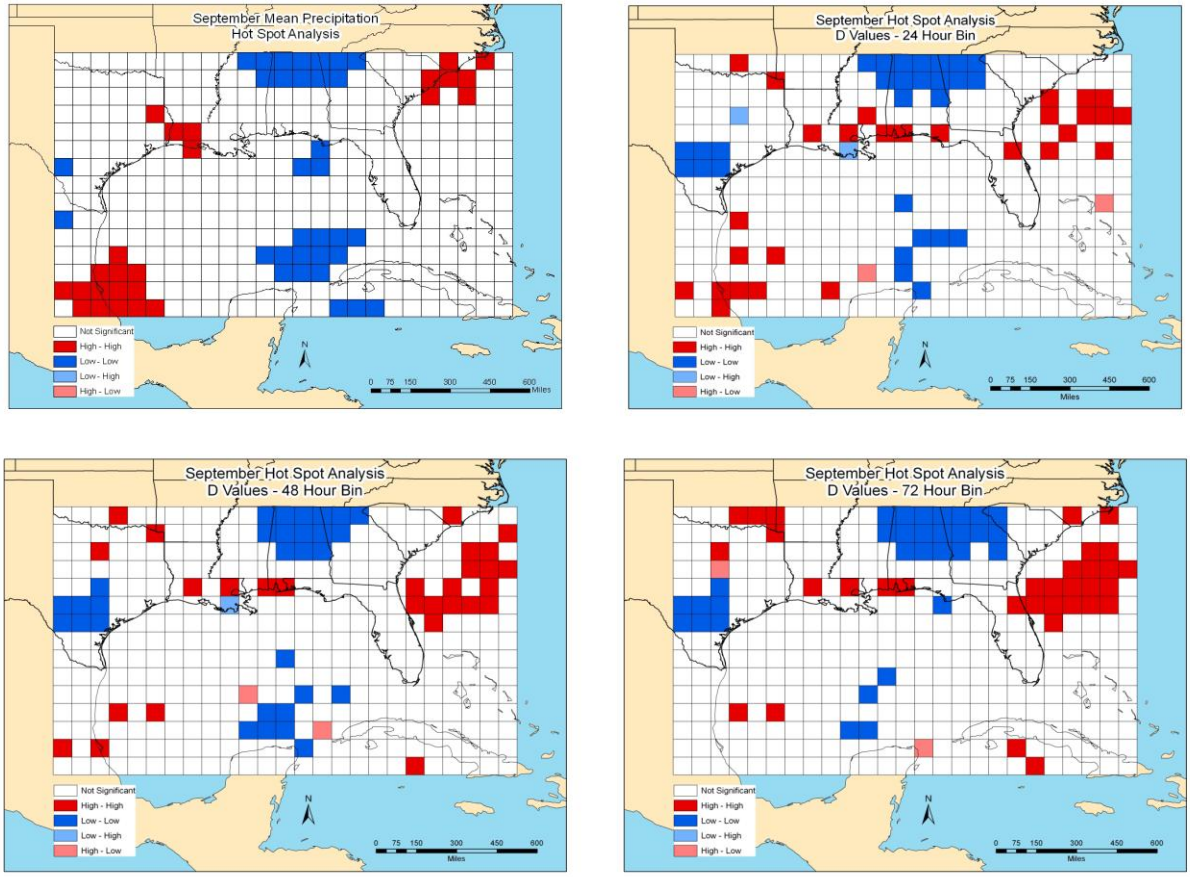

Figure 22 (left to right). September Hotspot Analysis of (1) Mean Precipitation; D Values at (2) 24 Hour, (3) 48 Hour, and (4) 72 Hour Bins.

4.3.2 September

4.3.2.a Mean Precipitation

The September mean precipitation hot spot analysis (Figure 22.1) shows areas of low – low positive spatial autocorrelation (more El Nino extreme precipitation) in the north and south central portion of the study region. High – high positive spatial autocorrelation (more La Nina extreme precipitation) is prevalent in the southwest and northeast corners of the study region.

4.3.2.b 24 Hour Bin

The September hot spot analysis of D values for the 24 hour bin (Figure 22.2) reveals low – low values of positive spatial autocorrelation (more El Nino extreme precipitation) in the northern and southern portion of the study region, along with south-central Texas. High – high values (more La Nina extreme precipitation) are more spread out with the highest concentrations focused in the southwest and northeastern section of the study region. Also, there is a concentration of high – high values along the Gulf coast from Louisiana to the panhandle of Florida.

4.3.2.c 48 Hour Bin

The 48 hour bin (Figure 22.3) is similar to the 24 hour bin. The most noticeable differences revolve around an expanding area of high – high positive spatial autocorrelation values (more La Nina extreme precipitation) off the southeast coastline and a decrease in spatial extent of high – high values in the southwest corner of the study region.

4.3.2.d 72 Hour Bin

There are similar patterns between the 48 and 72 hour (Figure 22.4) bins. However, there tends to be more areas of positive spatial autocorrelation in the northern half of the study region. The high – high positive spatial autocorrelation (more La Nina extreme precipitation) off the southeast coast continues to expand at the 72 hour bin. The low – low positive spatial autocorrelation (more El Nino extreme precipitation) likewise expands across northern Alabama and Georgia. The significant boxes in the southern region largely disappear with no large scale positive spatial autocorrelation.

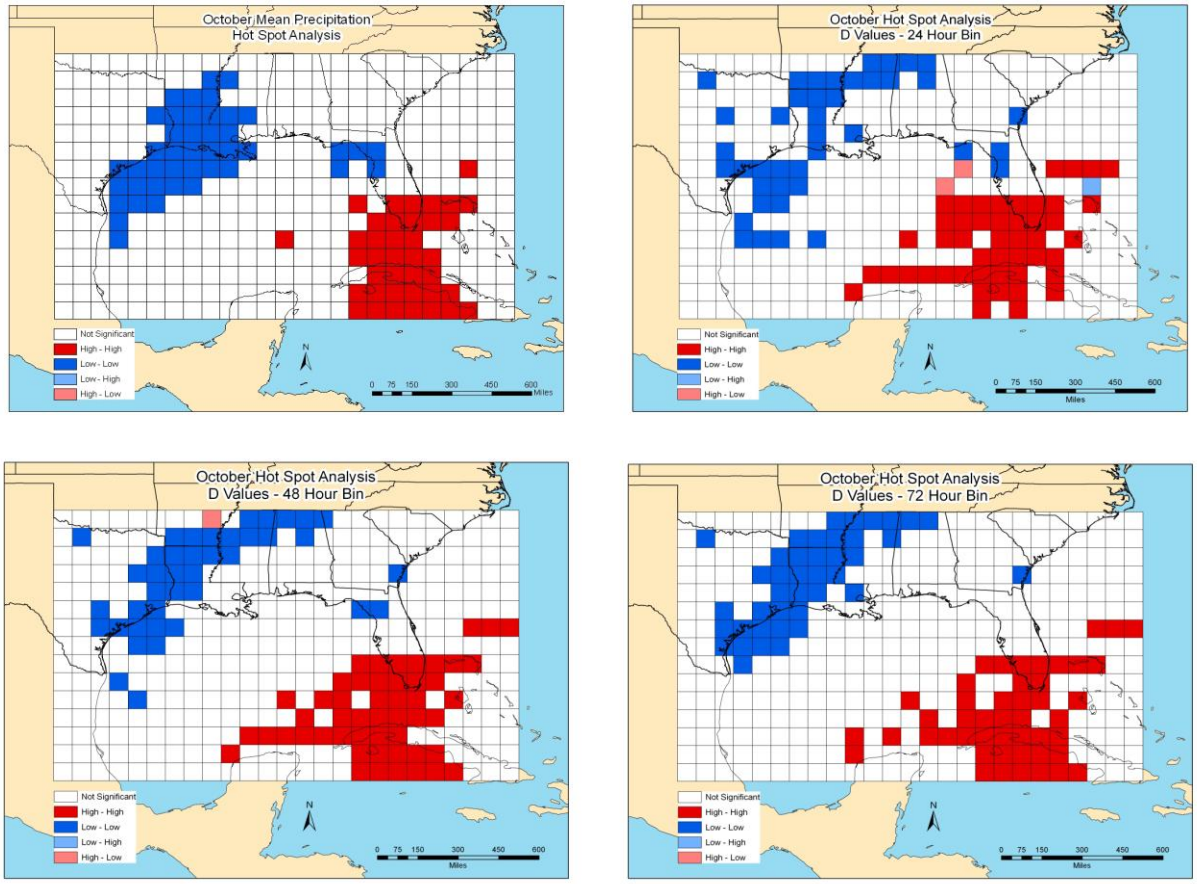

Figure 23 (left to right). October Hotspot Analysis of (1) Mean Precipitation; D Values for (2) 24 Hour, (3) 48 Hour, and (4) 72 Hour Bins.

4.3.3 October

4.3.3.a Mean Precipitation

The October hot spot analysis of mean precipitation (Figure 23.1) exhibits positive spatial autocorrelation across two large organized areas. High – high positive spatial autocorrelation values (more La Nina extreme precipitation) are prevalent from southern Florida into the Caribbean Sea. Low – low positive spatial autocorrelation values (more El Nino extreme precipitation) are present in the northwest Gulf of Mexico north and east into Louisiana. Across the panhandle hook of Florida there is another small area of low – low values.

4.3.3.b 24 Hour Bin

The 24 hour spatial analysis (Figure 23.2) shows a large area of high – high positive spatial autocorrelation (more La Nina extreme precipitation) across the southeastern portion of the Gulf of Mexico. The northwest Gulf of Mexico into Texas and east to Alabama displays a similarly sized area of low – low positive spatial autocorrelation (more El Nino extreme precipitation).

4.3.3.c 48 Hour Bin

The 48 hour bin (Figure 23.3) shows a remarkably similar size and extent of positive spatial autocorrelation values (more La Nina extreme precipitation). The only discernable pattern change is a polarizing effect, separating the opposing values of positive spatial autocorrelation.

4.3.3.d 72 Hour Bin

The 48 and 72 hour (Figure 23.4) bins of October are essentially the same. No significant pattern change emerges.

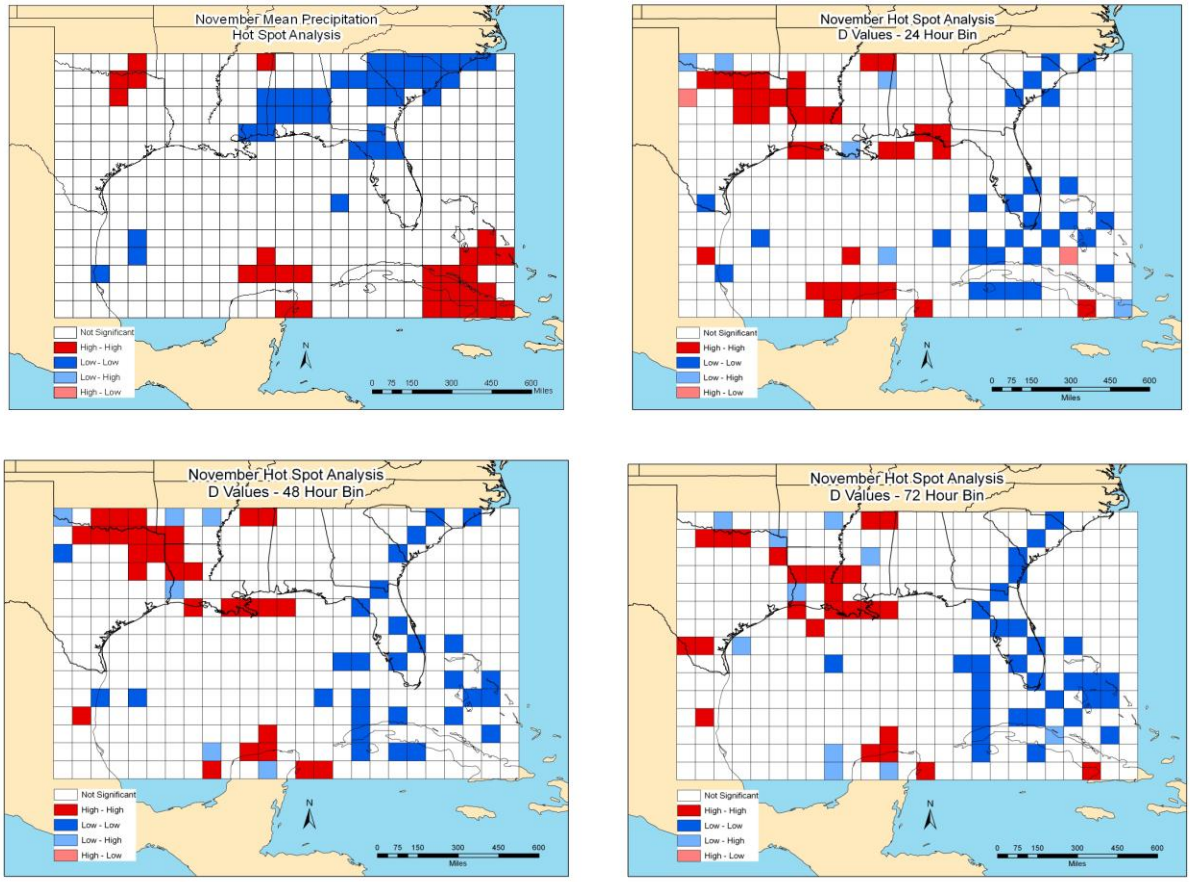

Figure 24 (left to right). November Hotspot Analysis of (1) Mean Precipitation; D Values for (2) 24 Hour, (3) 48 Hour, and (4) 72 Hour Bins.

4.3.4 November

4.3.4.a Mean Precipitation

The November mean precipitation hot spot analysis (Figure 24.1) exhibits two main areas of positive autocorrelation; the southeastern United States (low – low: more El Nino extreme precipitation) and the southeast corner (high – high: more La Nina extreme precipitation) of the study region. Additionally, there is a small area of high – high positive spatial autocorrelation north of the Yucatan Peninsula.

4.3.4.b 24 Hour Bin

November exhibits sporadic organization of positive spatial autocorrelation. At the 24 hour bin (Figure 24.2) high – high positive spatial autocorrelation values (more La Nina extreme precipitation) are scattered from Louisiana towards the panhandle of Texas. Another small area resides near the Yucatan Peninsula. Low – low values (more El Nino extreme precipitation) are scattered in a checker like pattern across the southeastern study region along with the Carolinas.

4.3.4.c 48 Hour Bin

The 24 and 48 hour (Figure 24.3) bins are similar in structure.

4.3.4.d 72 Hour Bin

The 72 hour bin (Figure 24.4) is similar likewise, though there is an increase in high – high (more La Nina extreme precipitation) coverage in Louisiana and a decrease in coverage over Texas/Oklahoma.

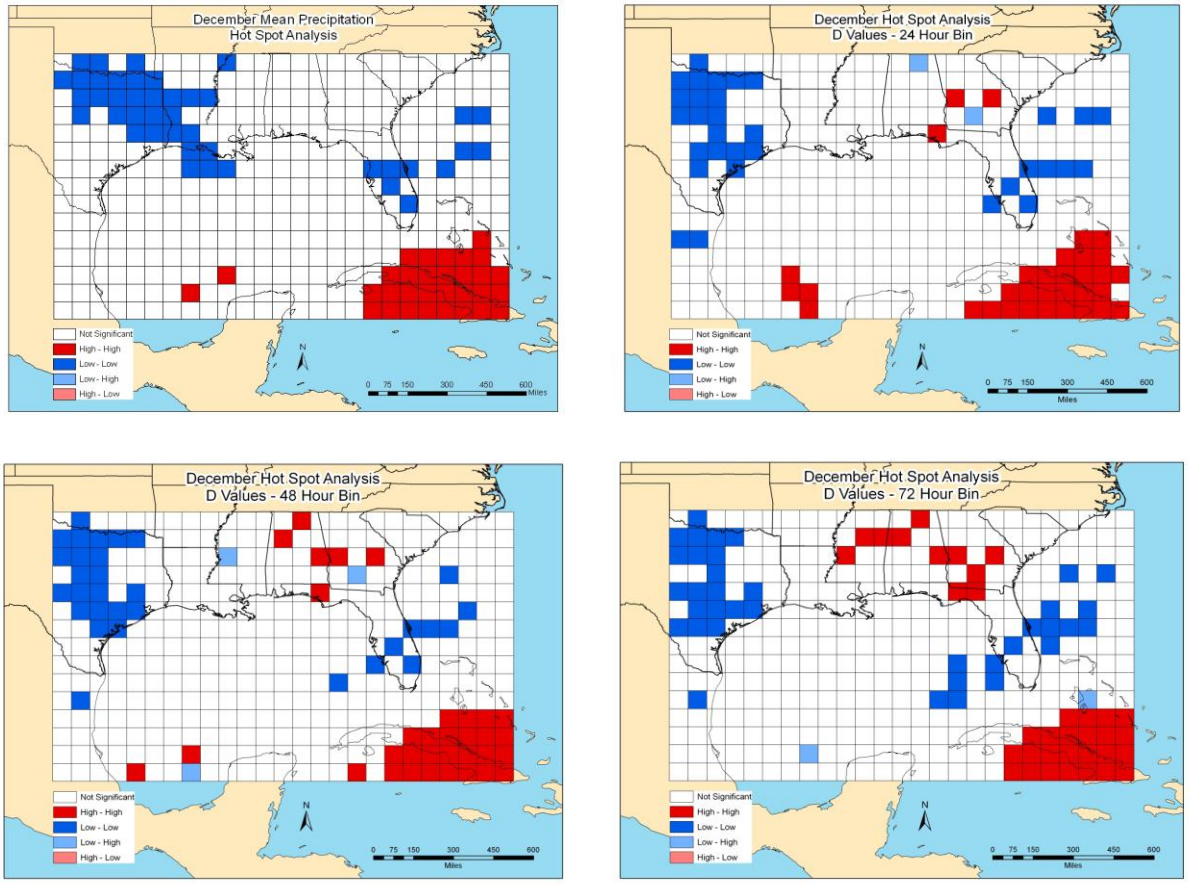

Figure 25 (left to right). December Hotspot Analysis of (1) Mean Precipitation; D Values for (2) 24 Hour, (3) 48 Hour, and (4) 72 Hour Bins.

4.3.5 December

4.3.5.a Mean Precipitation

The mean precipitation hot spot analysis (Figure 25.1) for December displays two large organized areas of positive spatial autocorrelation. High – high positive spatial autocorrelation values (more La Nina extreme precipitation) are concentrated across the southeast corner of the study region. Low – low values (more El Nino extreme precipitation) are focused from Texas to Louisiana. This pattern resembles the October map. A second smaller area of low – low values are in central Florida and off the southeast coast.

4.3.5.b 24 Hour Bin

The 24 hour hot spot analysis (Figure 25.2) also shows two similar areas of organized positive spatial autocorrelation. The southeast corner of the study region has an organized area of high – high positive (more La Nina extreme precipitation) spatial autocorrelation values. Grouping of low – low values (more El Nino extreme precipitation) occurs over Texas as well as a smaller scattered grouping across south Florida into the Atlantic Ocean.

4.3.5.c 48 Hour Bin

The 48 hour bin hot spot analysis (Figure 25.3) displays a similar pattern to the 24 hour analysis. One noticeable difference is an increase in coverage of high – high values (more La Nina extreme precipitation) over land in Alabama and Georgia.

4.3.5.d 72 Hour Bin

The 72 hour bin (Figure 25.4) is also similar to the 24 hour bin. The general area of values is the same. However, the smaller regions from Mississippi to Georgia (high – high: more La Nina extreme precipitation) and the low – low area (more El Nino extreme precipitation) around Florida have expanded in coverage across those regions.

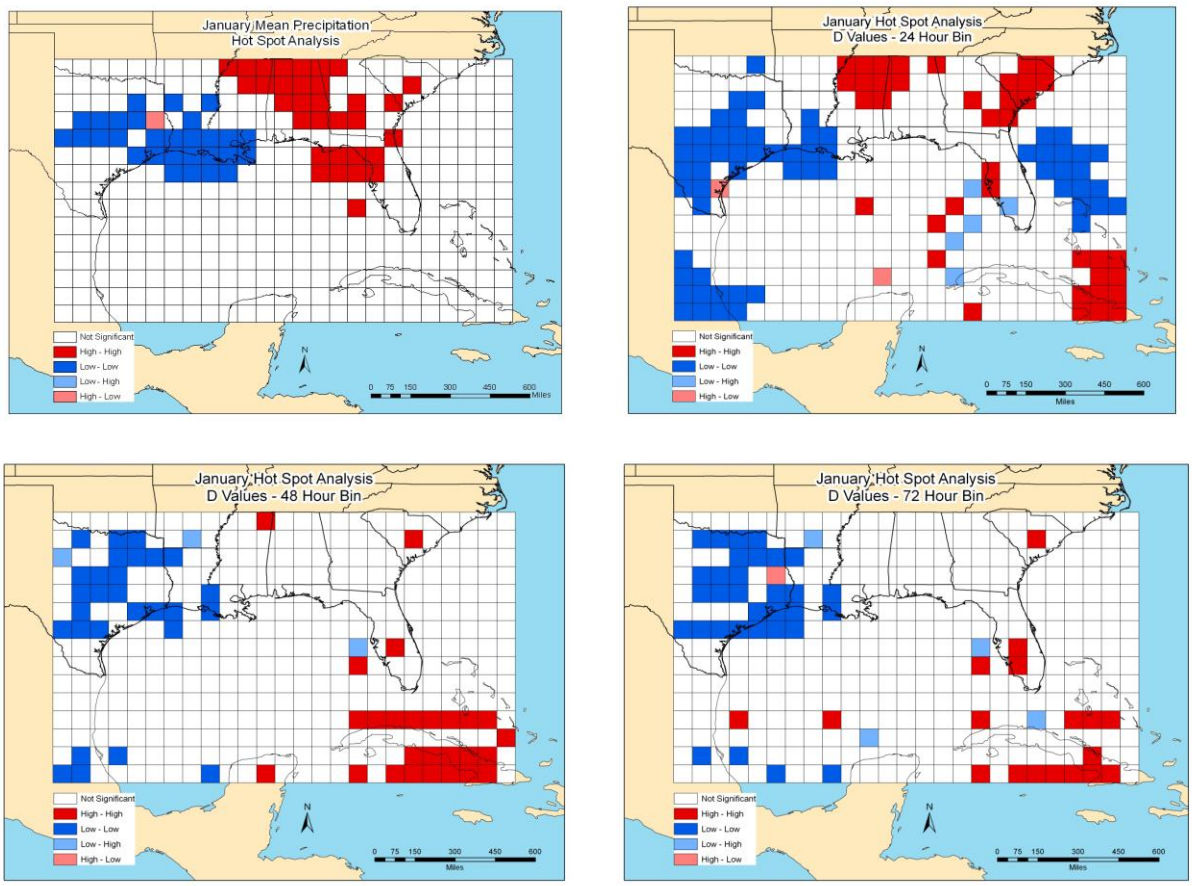

Figure 26 (left to right). January Hotspot Analysis of (1) Mean Precipitation; D Values for (2) 24 Hour, (3) 48 Hour, and (4) 72 Hour Bins.

4.3.6 January

4.3.6.a Mean Precipitation

In January mean precipitation hot spot analysis (Figure 26.1) areas of positive spatial autocorrelation are relegated to the northern half of the study region, mainly over land. High – high values of positive spatial autocorrelation (more La Nina extreme precipitation) dominate from northern Mississippi southeast to northern Florida. Low-Low values (more El Nino extreme precipitation) are centered on the Louisiana coast.

4.3.6.b 24 Hour Bin

The 24 hour bin January hot spot analysis (Figure 26.2) shows a greater coverage of spatial autocorrelation. Areas of organized high – high values of positive spatial autocorrelation (more La Nina extreme precipitation) are present in northern Mississippi, South Carolina and the southeastern corner of the study region. Areas of organized low – low values of positive spatial autocorrelation (more El Nino extreme precipitation) are present in southeast Texas into Louisiana, off the east coast of Florida and the southwest corner of the study region.

4.3.6.c 48 Hour Bin

The 48 hour bin (Figure 26.3) is drastically different than the 24 hour bin. The only similarities are an area of low – low positive spatial values (more El Nino extreme precipitation) in Texas. All other significant organized areas of positive spatial autocorrelation from the 24 hour analysis disappear, and high-high positive spatial values (more La Nina extreme precipitation) emerge in the southeast corner of the study area.

4.3.6.d 72 Hour Bin

The January the 72 hour (Figure 26.4) bin is similar to the 48 hour bin. However the 72 hour bin shows a decrease in coverage in high – high values (more La Nina extreme precipitation) in the southeast portion of the study region while the low – low positive spatial autocorrelation values (more El Nino extreme precipitation) in Texas become more numerous.

4.3.7 Summary Hotspot Analysis of D values

Large areas of positive spatial autocorrelation occur at each month. One exception is a linear pattern of positive spatial autocorrelation grid boxes along the Gulf Coast in September. October and December display the most coherent spatial patterns with eerily similar location,

extent and values of positive spatial autocorrelation, with large areas of El Nino driven extreme precipitation across the northwestern Gulf of Mexico and La Nina driven extreme precipitation across the southeastern part of the study region. January also follows a similar pattern, although weaker. November displays a considerably weaker spatial pattern. The stronger patterns and general similarities between October and December confirm the Moran's I statistic. A shift towards more spatial dependence between grid boxes and larger a difference between ENSO precipitation distributions likely follows a change in synoptic forcing across the Gulf of Mexico region.

4.4 Independent Grid Box and Hotspot Analysis Summary

The independent grid box and hotspot spatial analysis displayed similar results. However, the spatial analysis is preferred for identifying large spatial patterns. The hotspot analysis was able to identify larger areas of positive spatial autocorrelation at shorter bin lengths (ex. October). The spatial analysis is also significant at the one percent level, while the independent grid box analysis is only significant at the five percent level, adding to the confidence in the hotspot analysis. Finally, the Moran's I statistic adds more information to the quality of the overall spatial fit. In summary, the independent grid box analysis suggests spatial autocorrelation, and the hotspot analysis confirms it, while the Moran's I values communicate the strength of the spatial patterns for the Gulf of Mexico as a whole.

4.5 Precipitation Rate at D

The previous hot spot analysis is now performed for the precipitation rate at D. This is important because when selecting grid boxes based on precipitation ranges (i.e. low-level, mid-level, and high-level), they should represent their neighborhood, giving more confidence to the synoptic forcing analysis.

4.5.1 Moran's I Values

Similar to the Moran's I values for the hotspot analysis of D values, Moran's I values for the rate of precipitation at D (Table 3) are most significant in general at higher bins. Exceptions include December and January where the highest Moran's I values occur at the 48 hour bin. Also similar, October and December exhibit the largest Moran's I values. None of the Moran's I values reach significance. January exhibits much larger Moran's I values at the 48 hour bin. In fact, January has the maximum Moran's I value. This will be supported with the inspection of the large area of positive spatial autocorrelation over the Gulf States.

Month	**24**	**48**	**72**
AUG	0.017	0.106	0.273
SEP	0.177	0.242	0.246
OCT	0.127	0.165	**0.350**
NOV	0.110	0.208	0.331
DEC	**0.297**	0.357	0.278
JAN	0.275	**0.429**	0.288
Mean:	0.167	0.251	0.294
Min:	0.017	0.106	0.246
Max:	0.297	0.429	0.350
Range:	0.280	0.323	0.104

Table 3. Precipitation Rate at D Moran's I Values. 24, 48, and 72 hour bins. Largest values are bolded.

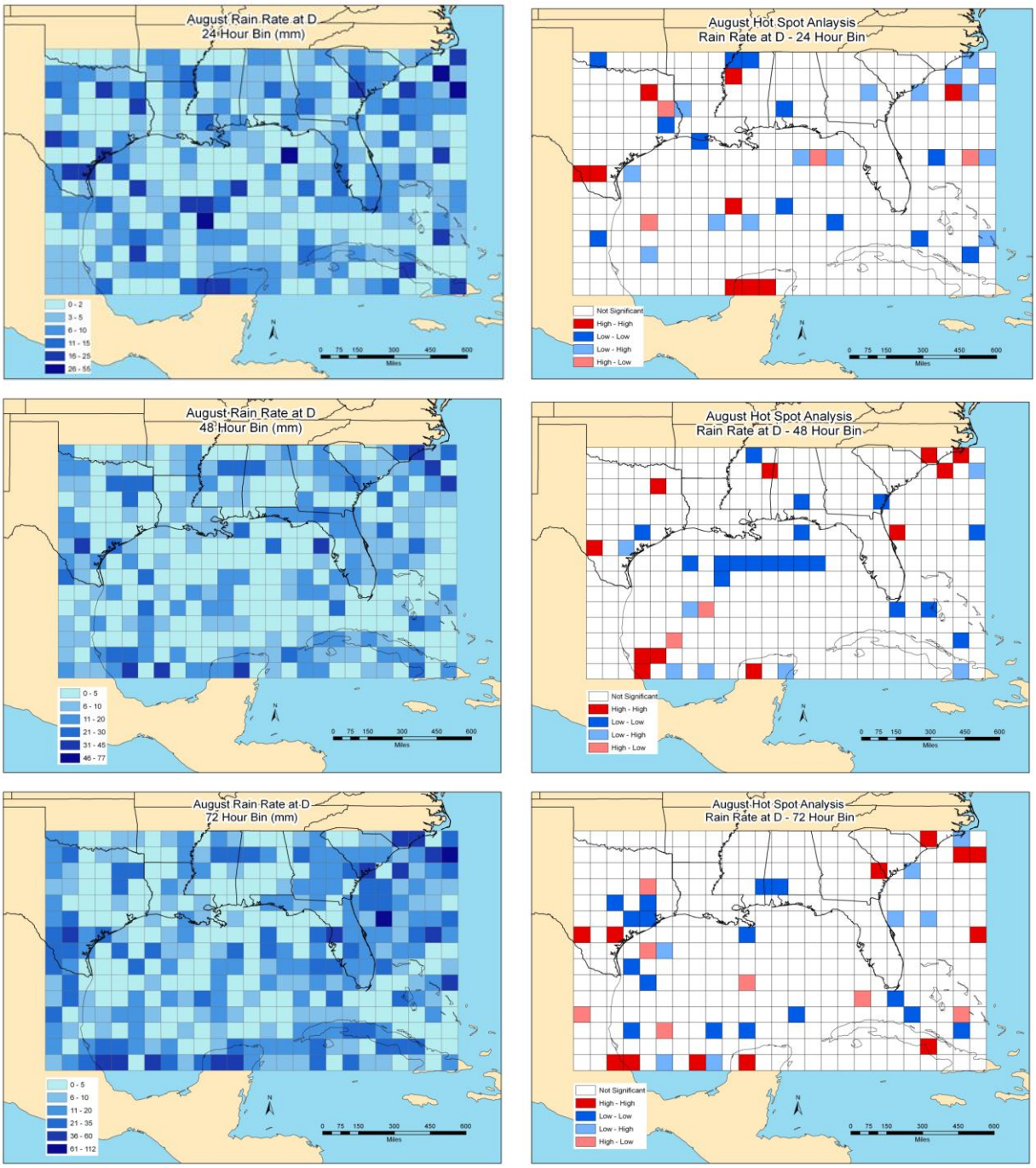

Figure 27. August Precipitation Rate at D (left) and Hotspot Analysis (right). 24, 48 and 72 Hour Bins (top to bottom).

4.5.2 Hotspot Analysis of the Precipitation Rate at D

4.5.2.a August

For August (Figure 27), the rain rate spatial distribution is sporadic, especially at the 24 hour bin length. Organized areas of the high precipitation rates at the D statistic are prevalent off the southeast coast with low precipitation rates at D present through much of the Gulf of Mexico into the southeast area of the study region. The 48 and 72 hour precipitation rates offer new trends. In particular there is a noticeable increase in spatial autocorrelation. Interestingly the 48 hour and particularly the 72 hour bin shows increased spatial coverage of high precipitation rates at D over Florida and off the southeast coast. A general trend of lower precipitation rates occur over the Gulf of Mexico, especially for the 48 hour bin.

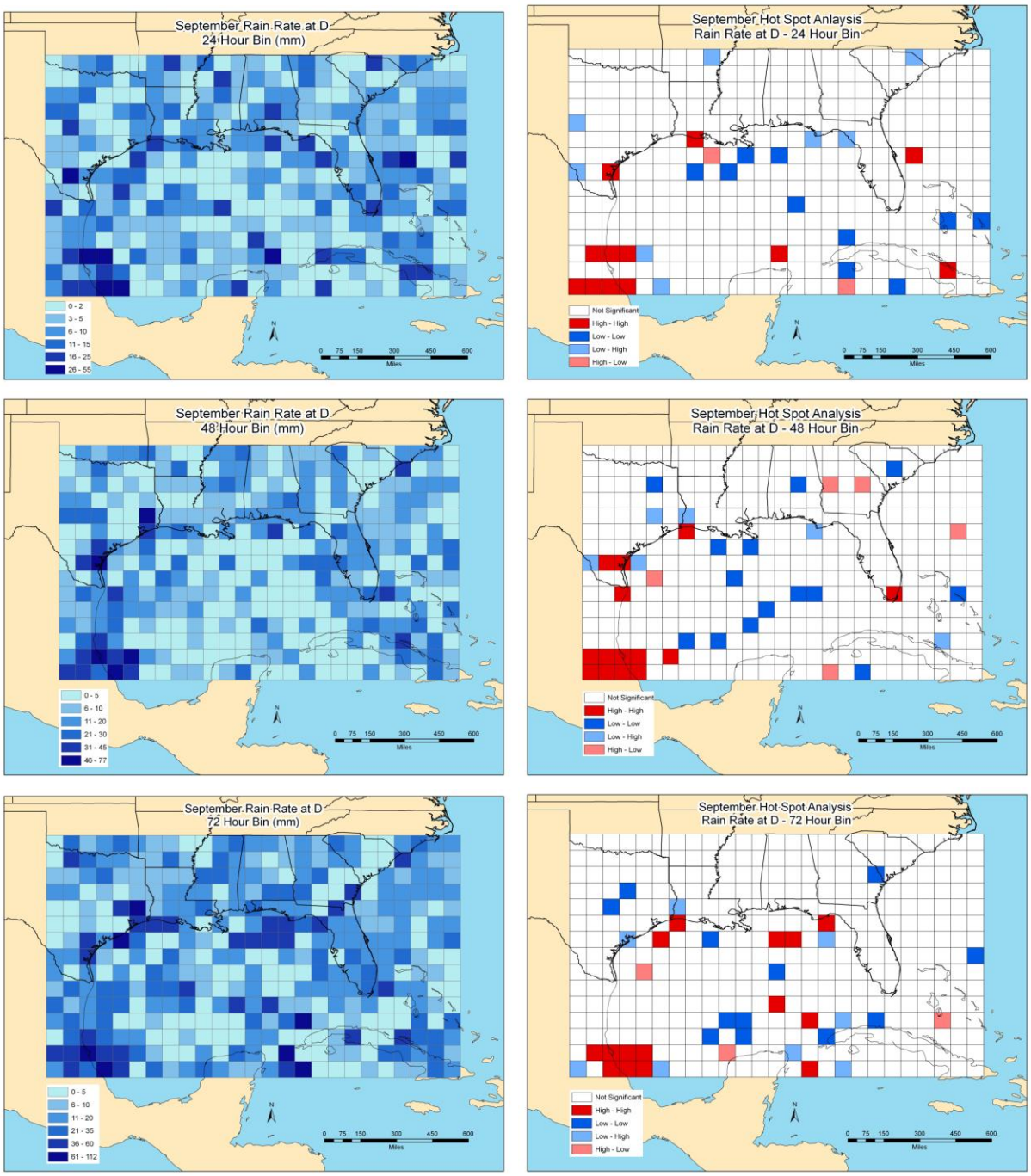

Figure 28. September Precipitation Rate at D (left) and Hotspot Analysis (right). 24, 48 and 72 hour bins (top to bottom).

4.5.2.b September

September (Figure 28) has a slight increase in spatial autocorrelation. Most notably, there is a well organized area of high – high positive spatial autocorrelation values (higher rates of precipitation at D) at the 24, 48, and 72 hour bin sizes over the southwest portion of the study region. A coastline bias towards higher values seems to be a trend, especially at high bin sizes. This suggests there is a tendency for a substantial change in high precipitation rates along the coastline.

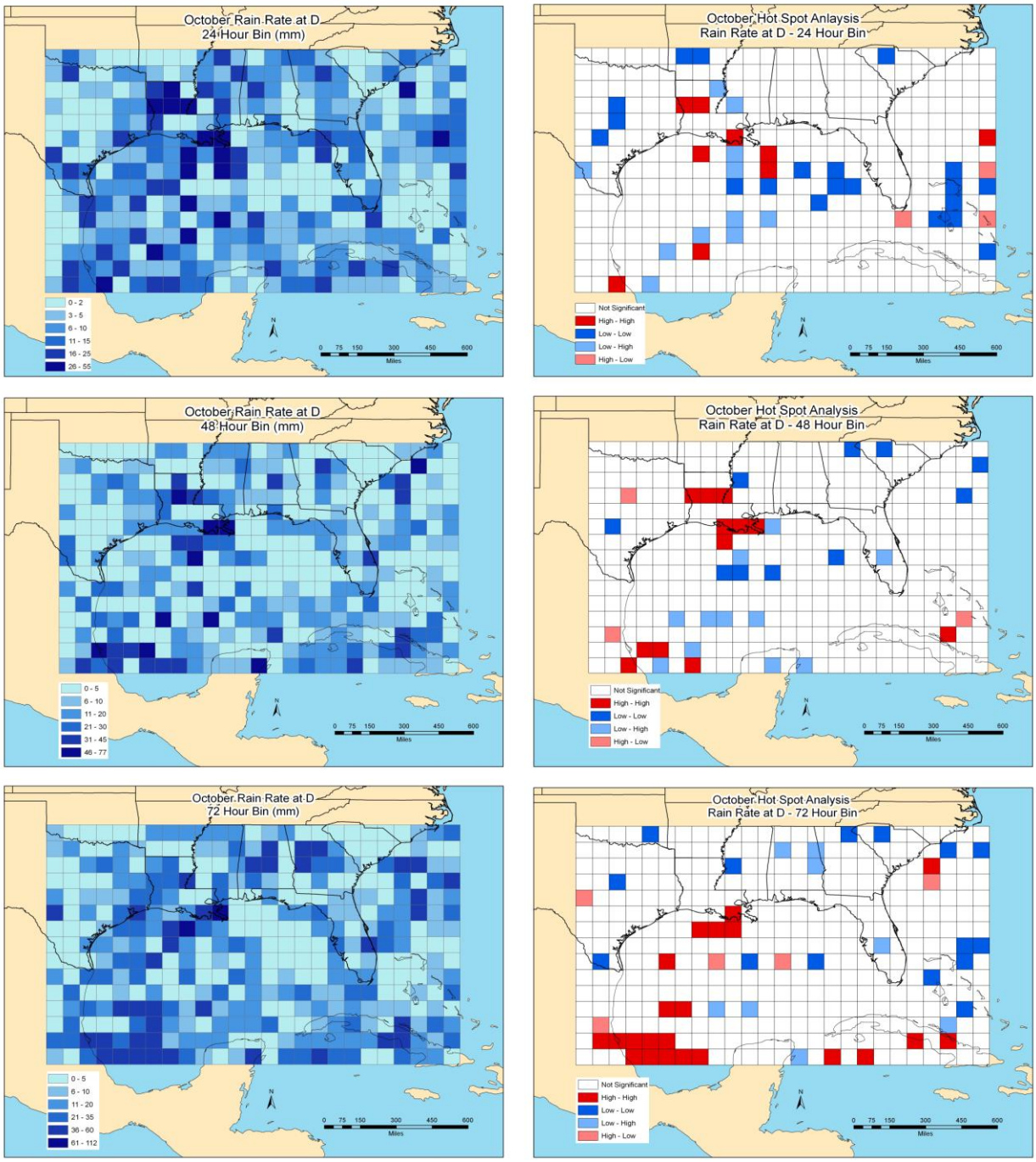

Figures 29. October Precipitation Rate at D (left) and Hotspot Analysis (right). 24, 48 and 72 hour bins (top to bottom).

4.5.2.c October

The month of October (Figure 29) shows an area of scattered high precipitation values from the southwest portion of the study region, through the western gulf into Louisiana. This is supported at all three bins by the scattered high – high positive autocorrelation values in the hot spot analysis for the precipitation rates. A costal linear bias towards high values is noticeable at all bins.

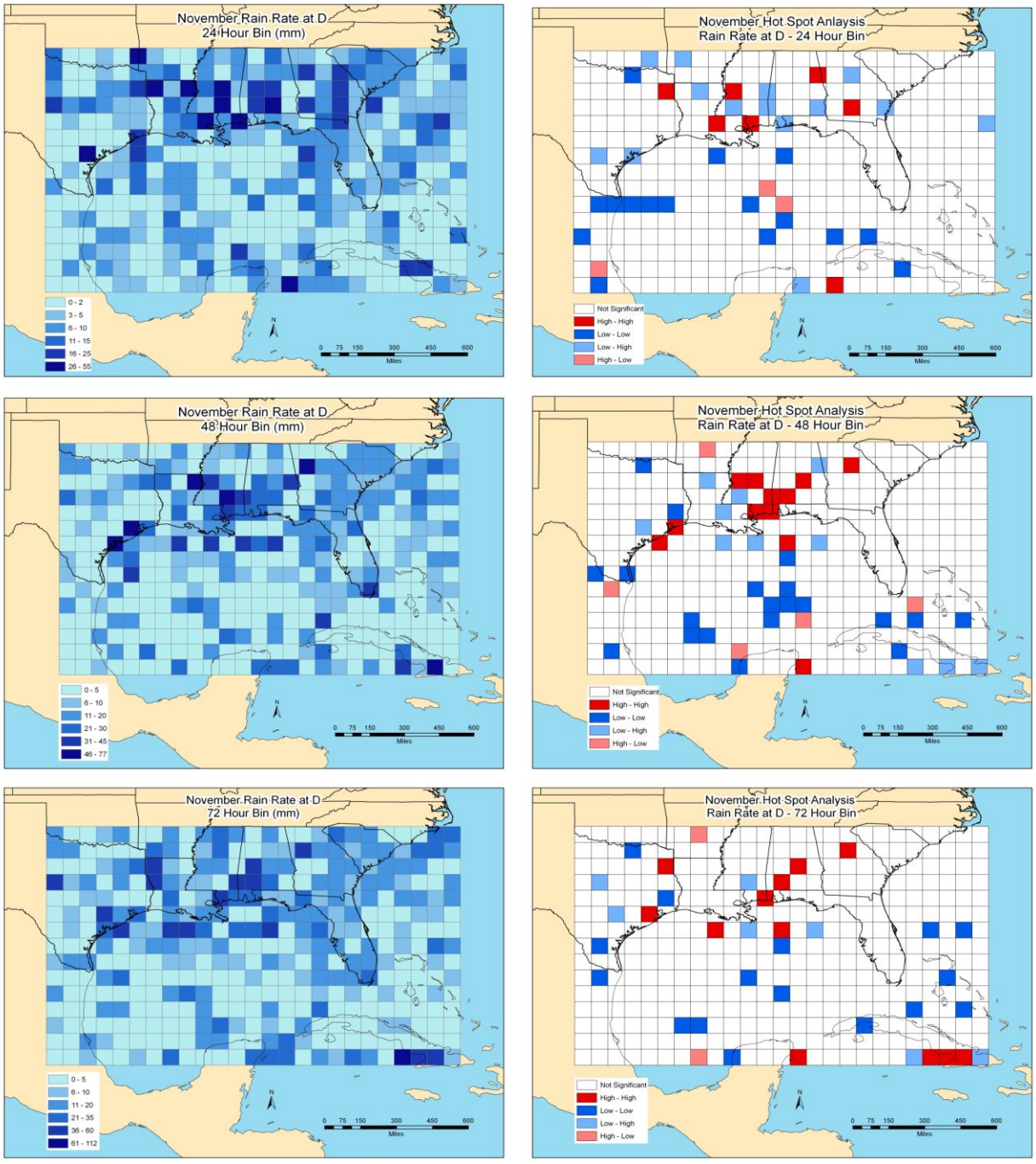

Figure 30. November Precipitation Rate at D (left) and Hotspot Analysis (right). 24, 48 and 72 hour bins (top to bottom).

4.5.2.d November

The month of November (Figure 30) displays a clear northern bias towards high rates of precipitation. The region with the highest rates occurs along the northern Gulf of Mexico and southeast United States coastline, northward into an area from Louisiana into Georgia. High rates of precipitation occur predominately north of 25 degrees north latitude. Also note how most of the high rates of precipitation at D occur over land.

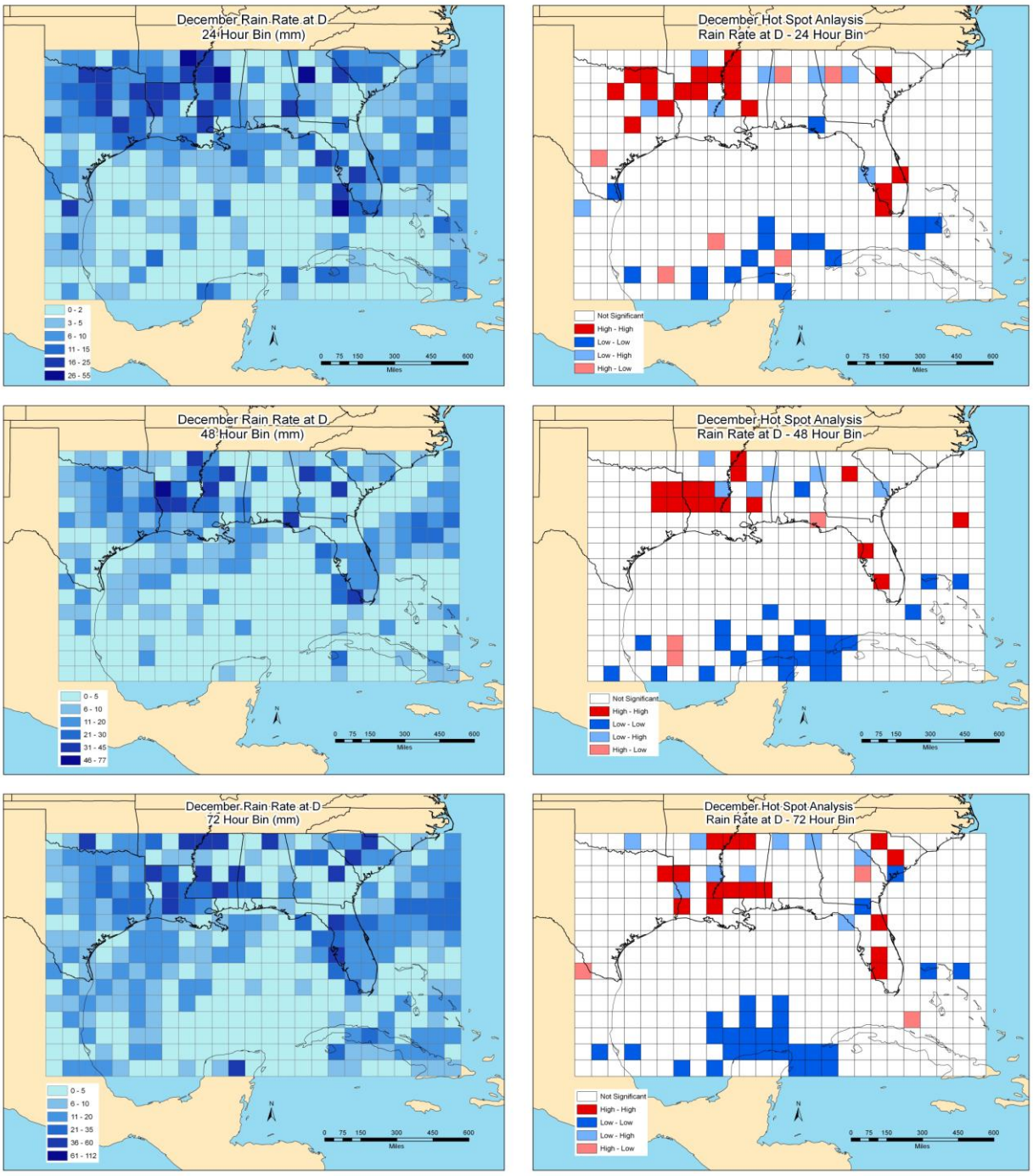

Figure 31. December Precipitation Rate at D (left) and Hotspot Analysis (right). 24, 48 and 72 hour bins (top to bottom).

4.5.2.e December

December (Figure 31) has a cluster of high rates of precipitation at D from east Texas to Mississippi and over southern Florida. Low values persist over most of the Gulf of Mexico and South of Florida. Similar to November, entering the cold season, there is a distinct northern region, over land that experiences a change in precipitation distributions at high end precipitation rates. Moving into December, notice how the greatest precipitation rates at D become focused along the coast and inland in the northwestern Gulf of Mexico.

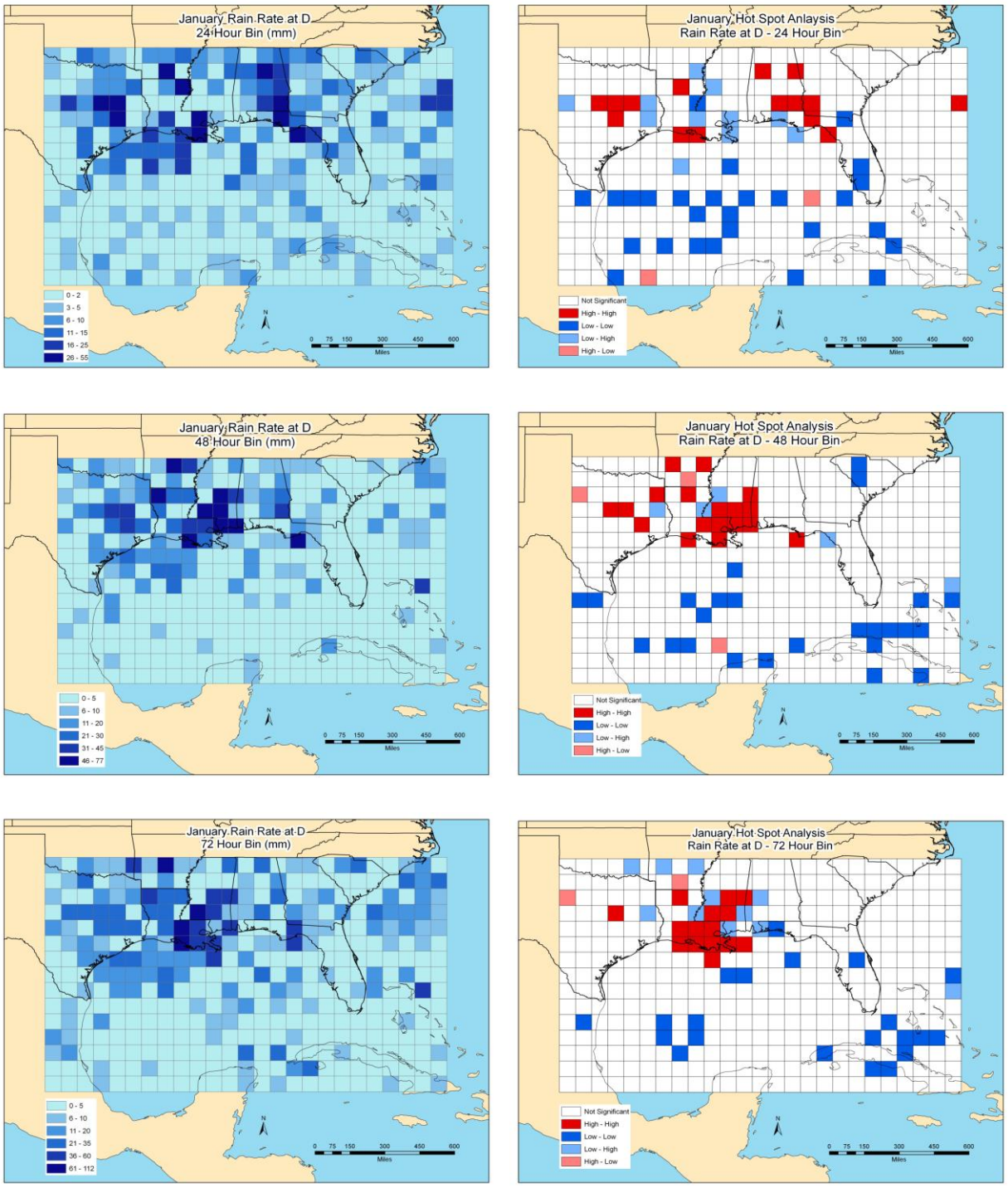

Figure 32. January Precipitation Rate at D (left) and Hotspot Analysis (right). 24, 48 and 72 hour bins (top to bottom).

4.5.2.f January

The 24 bin for January (Figure 32) displays two main clusters of high rates of precipitation at D. One area is focused across southeastern Alabama and another area across eastern Texas into Louisiana. A substantial shift takes place for D values at the 48 and 72 hour bins. The highest rate of precipitation at D becomes focused over southeastern Louisiana at larger bin lengths. In general the high precipitation rates continue to merge westward focused in southern Mississippi and Louisiana

4.5.7 Precipitation Rate at D Summary

A trend emerges over the six month period for clusters of high rates of precipitation at D. From August into September high – high positive spatial autocorrelation values (large precipitation rates at D) expand across the western Bay of Campeche. By October high rates of precipitation at D become more scattered and shift northward into the western Gulf of Mexico and into Louisiana. In November high values are prevalent across the Deep South from Louisiana east to Georgia. December shows a similar trend, though values are displaced north and westward into eastern Texas east to Mississippi. December also has more significant positive spatial autocorrelation as shown by the larger grouping of high – high positive spatial autocorrelation values than any of the previous months. In January the high – high values shift to the south over southern Mississippi and Louisiana and into the adjacent grid boxes off shore. This pattern suggests a possible connection to a northward and strengthening subtropical jet stream with eventual polar jet interaction as the max precipitation rates stall along the southern Gulf of Mexico.

Interestingly, from November through December the largest difference in precipitation rates over land occurs predominately at high precipitation rates, while outside of the north Gulf

of Mexico the largest difference in the precipitation cumulative distribution functions occurs at low precipitation rates. This is an important finding for a couple reasons. From an atmospheric viewpoint it suggests that in November ENSO forced changes in regional and global circulations may affect land differently than the ocean and provide more or less high precipitation rates depending on the phase on ENSO. Since this occurs over land it creates increased precipitation variability for people to adapt to.

4.6 Grid Box Selection

Areas of large scale positive autocorrelation of D values are evident from August – January, most notably in October and December. The strong spatial patterns suggest that there are large scale changes in global circulations resulting in the large spatially dependent area of changing precipitation distributions during ENSO. For this reason, October and December are chosen for a synoptic analysis. Six grid boxes in total are selected to represent five regions of positive spatial autocorrelation.

In October grid boxes 179 and 242 (Figure 33) are selected for synoptic analysis. Both grid boxes are significant at the independent and hotspot spatial analyses**.** Grid box 179 is located off the coast of Texas in an area of negative D values (more extremes in El Nino). Grid box 242 is located to the west of Miami, Florida in an area of positive D values (more extremes in La Nina).

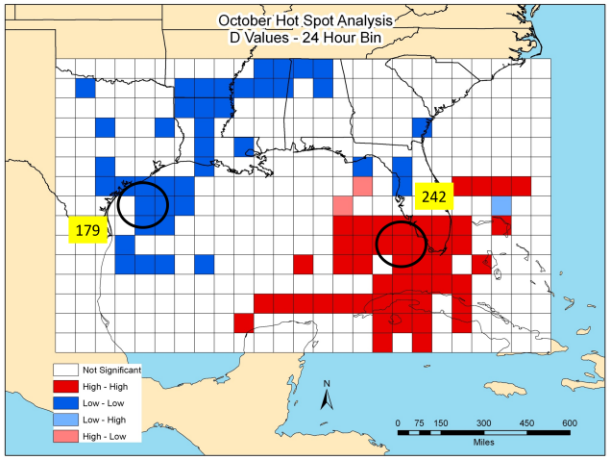

Figure 33. October Grid Boxes for Synoptic Analysis.

Grid box 179 (Figure 33) has considerably different ranges of precipitation rates in the absolute difference plots of the ENSO CDF curves (Figure 34) as depicted by the blue boxes. The 24 (Figure 34.1) and 72 hour bins (Figure 34.3) display two ranges of precipitation rates. The 48 hour bin has only one at the low end of precipitation, suggesting that the largest difference in precipitation distributions during ENSO occurs at light precipitation events.

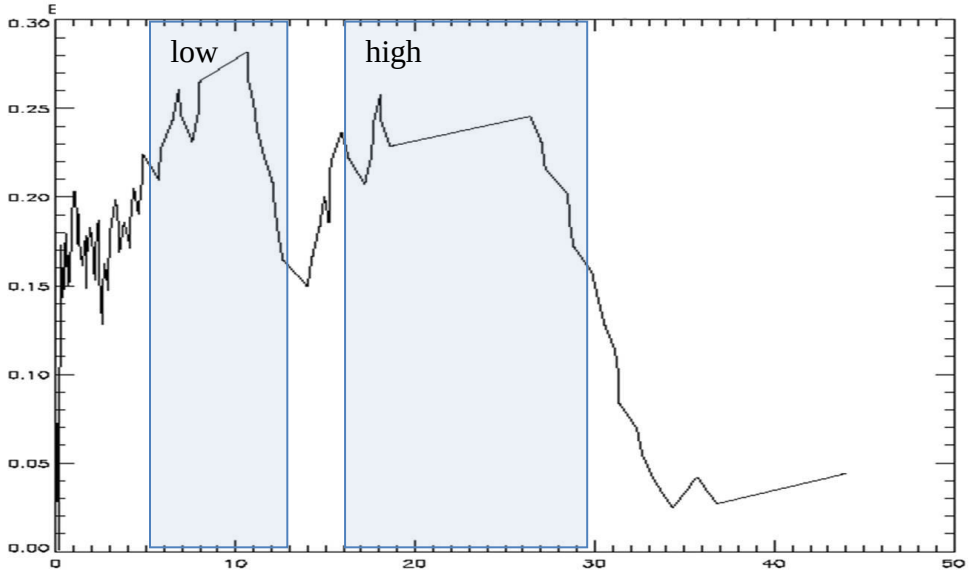

Precipitation (mm)

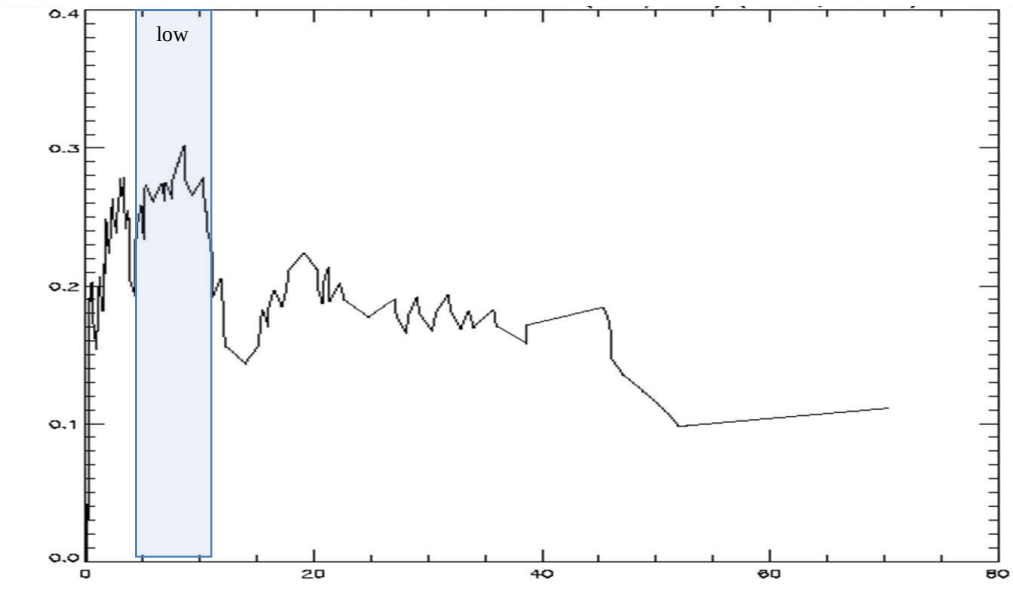

Precipitation (mm)

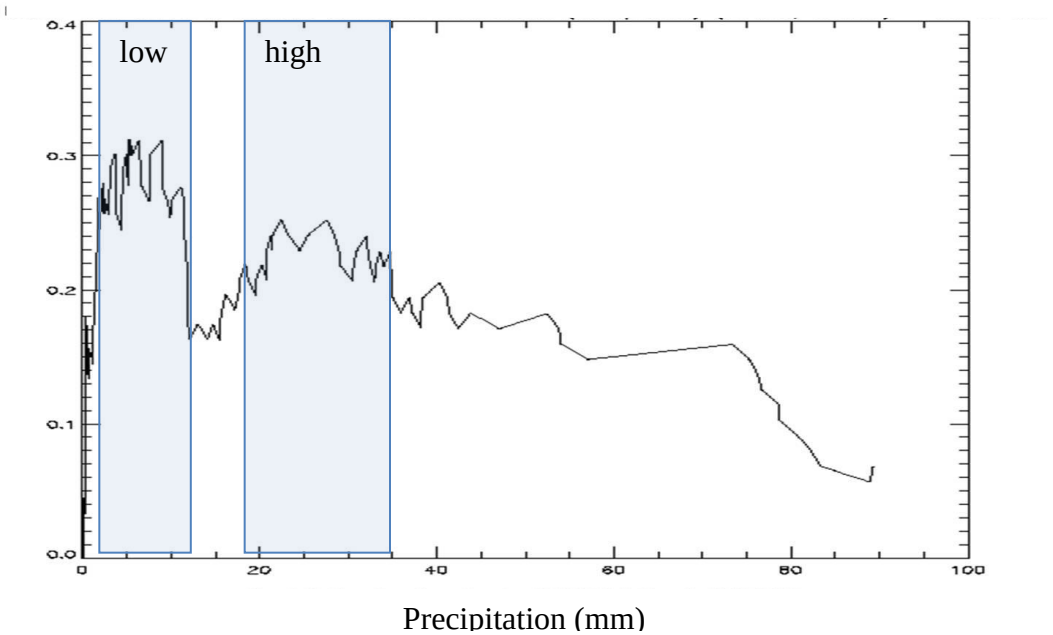

Figure 34. Grid Box 179 Difference CDF of ENSO Precipitation Distributions. Bins (1) 24, (2) 48 and (3) 72 from top to bottom.

Grid box 242 in contrast has relatively similar ranges of precipitation rates at each bin (Figure 35). The precipitation rates selected for this grid box range from about 8 mm per day at the 24/48 hour bins to 35 mm per day at the 72 hour bin.

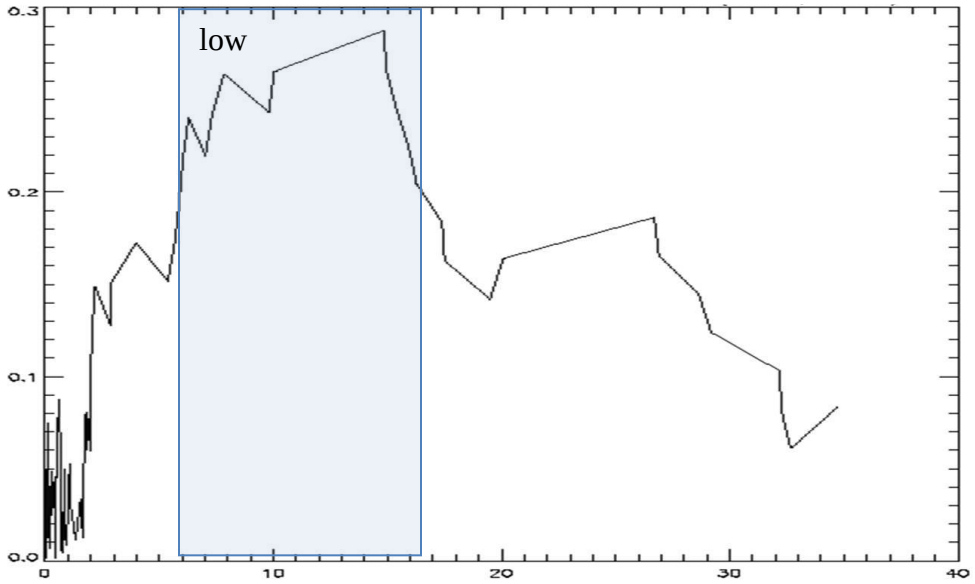

Precipitation (mm)

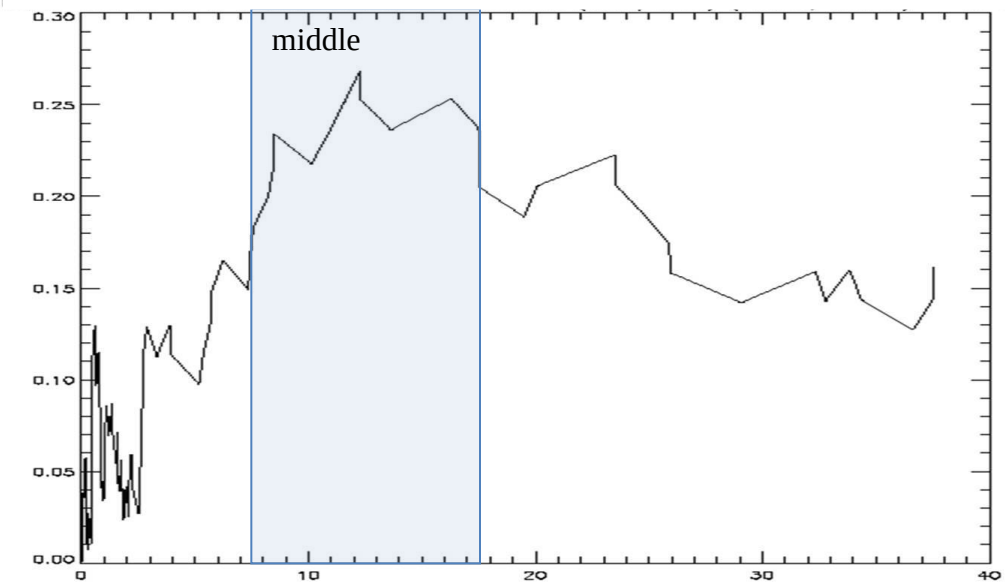

Precipitation (mm)

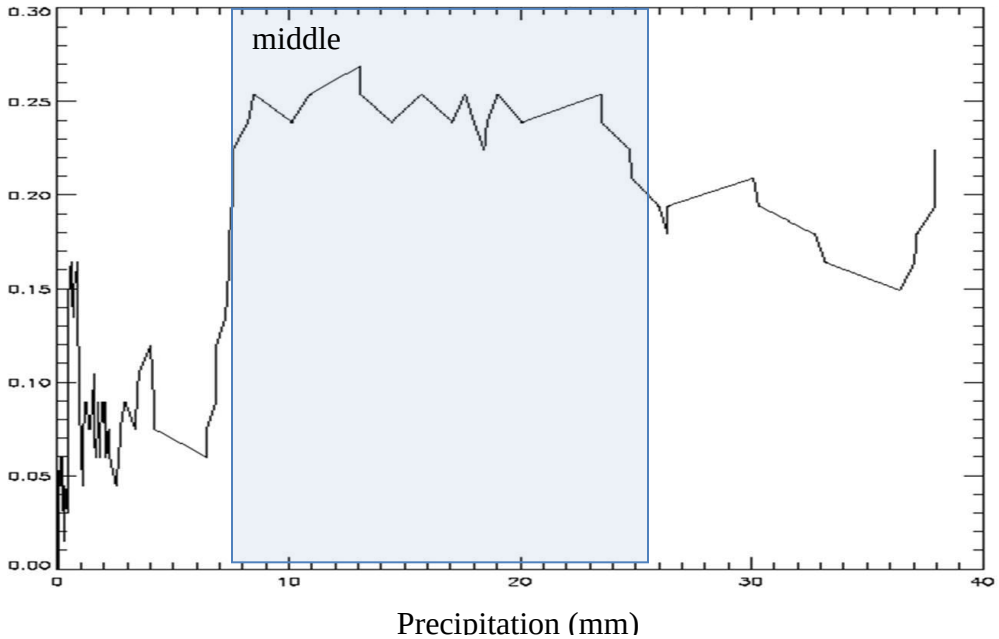

Figure 35. Grid Box 242 Difference CDF of ENSO Precipitation Distributions. Bins 24, 48 and 72 from top to bottom.

In December four grid boxes are selected (Figure 36) to represent three areas of positive spatial autocorrelation. Grid box 25 is located in an area of spatially autocorrelated negative D values (blue, El Nino with more extremes) in northern Texas. Grid box 170 is also located in an area of negative values off the east coast of Florida. Grid boxes 348 and 371 are side by side in the south east portion of the study region at the center of an area of positive values of D (red, La Nina with more extremes). They represent the same large area of positive D values, but have different precipitation distrubtions (see Figure 31). The greatest difference in the CDF of grid 348 occurs at high rain rates, while grid 371's greatest difference occurs at low rain rates. Two

samples in an area of positive D values (more extremes in La Nina) offers a comparison between synoptic conditions at adjacent grid boxes and how different rain rates may contribute.

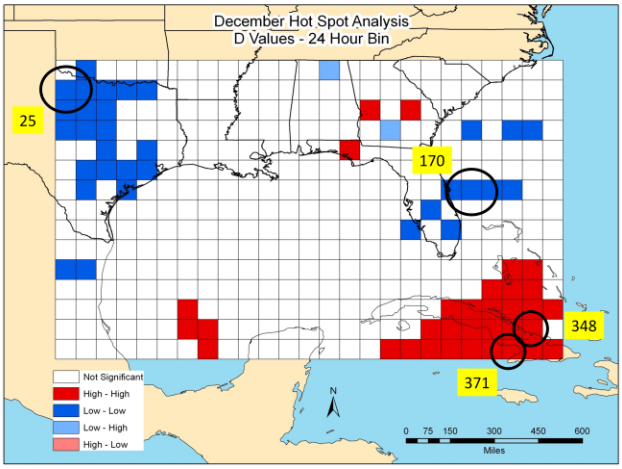

Figure 36. Selected Grid Boxes for December.

The difference between ENSO precipitation distributions for December (Figure 37-40) is similar at each bin length. The selected range of precipitation events runs from 7 to about 12 mm for each bin, despite an overall increase in precipitation events at larger bins. The overall result is the 48 and 72 hour bins capture a relatively lower range of precipitation for synoptic analysis, since at higher bins higher rates of precipitation are more common.

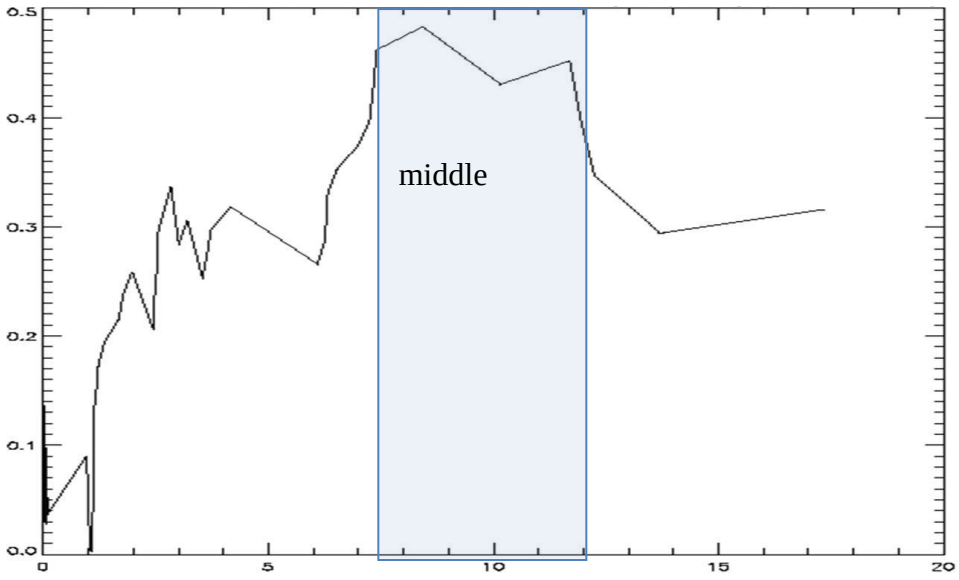

Precipitation (mm)

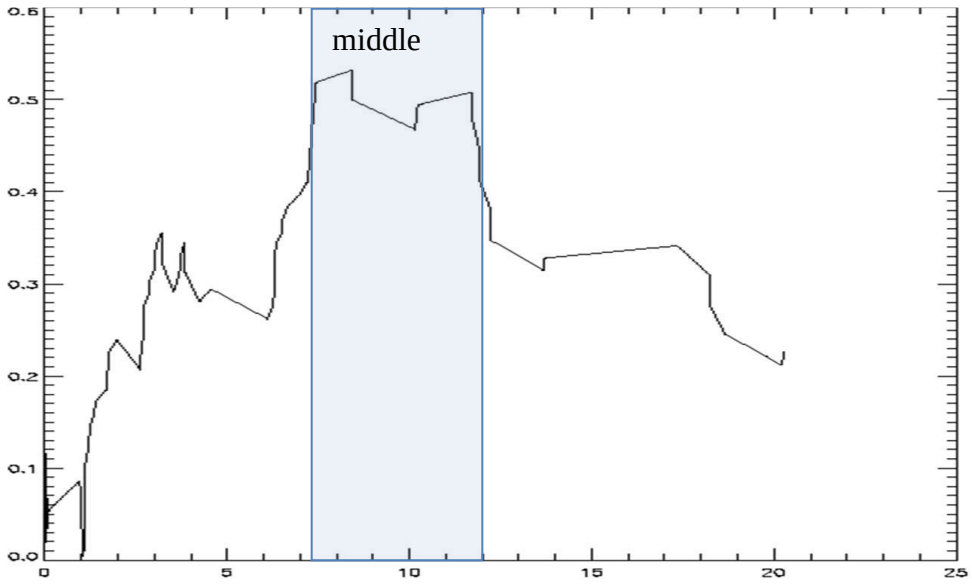

Precipitation (mm)

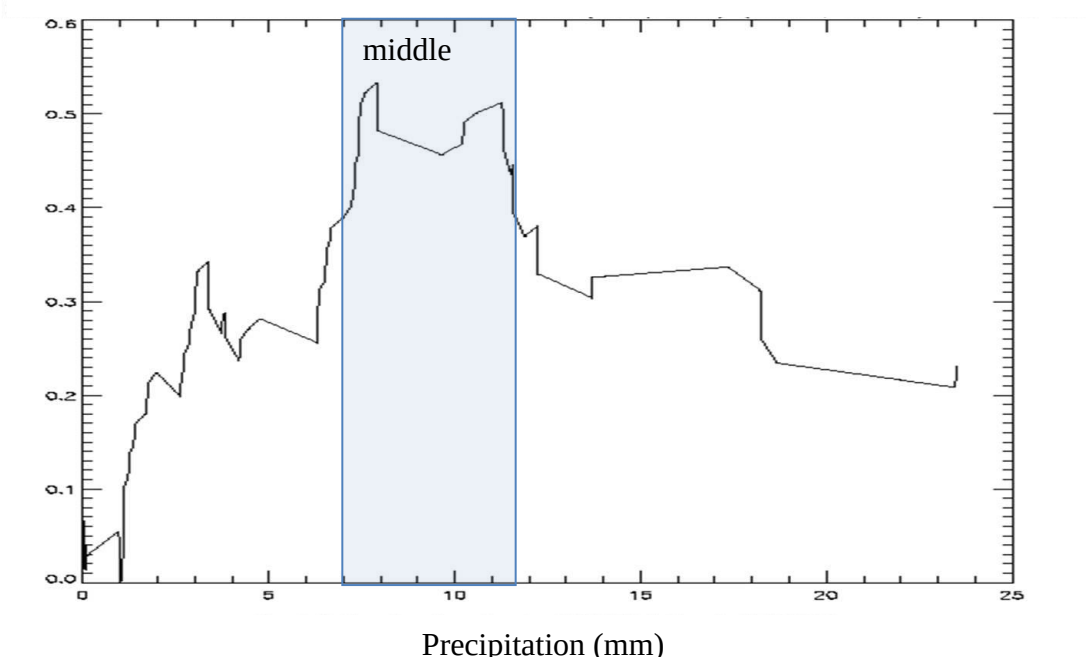

Figure 37. Grid Box 25 Difference CDF of ENSO Precipitation Distributions. Bins 24, 48 and 72 from left to right.

Grid box 25 displays a consistent, but minimal increase in precipitation rates accompaying the largest differences in ENSO CDFs (Figure 37). The increasing precipitation rates at higher bins, owning primarily to the fact that there is a greater amount of time to accumulate precipitation, essentially results in a constant range of precipitation rates.

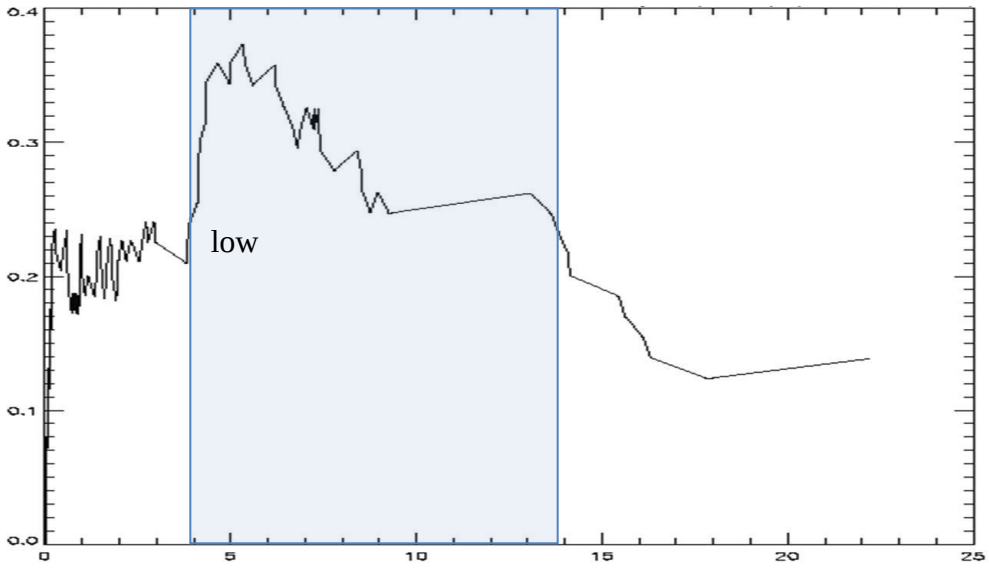

Precipitation (mm)

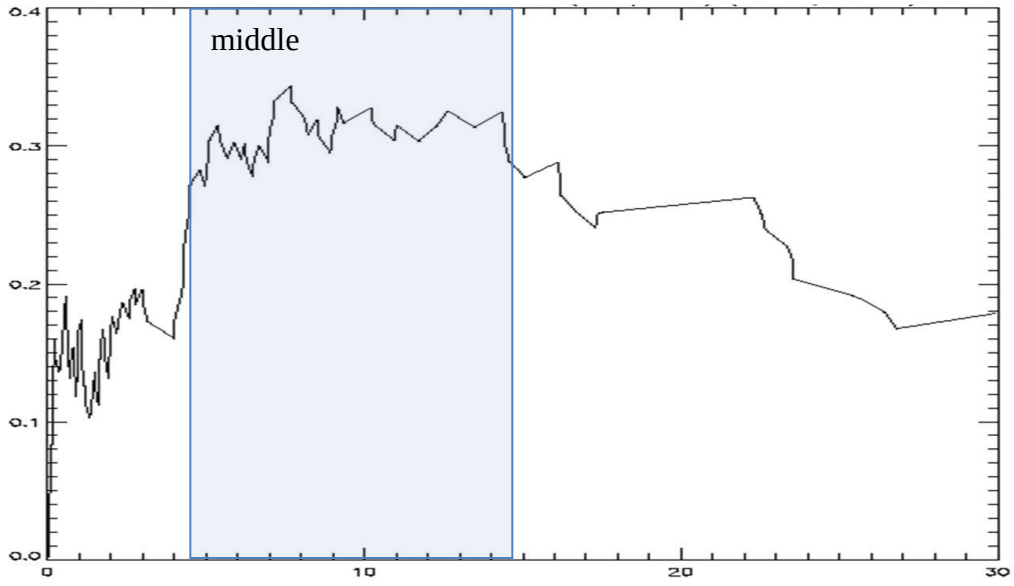

Precipitation (mm)

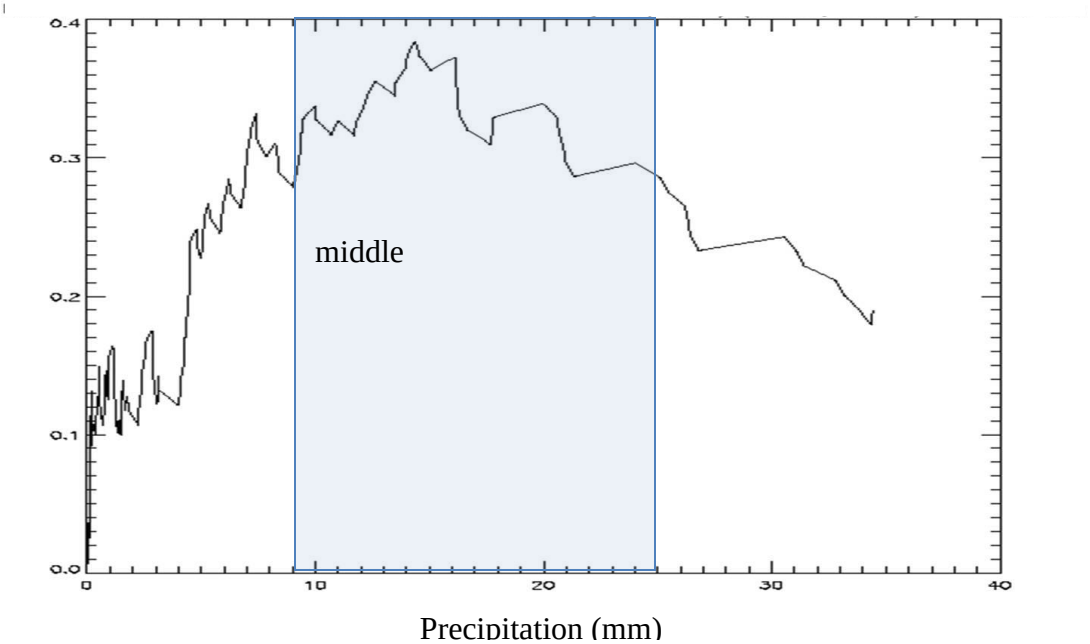

Figure 38. Grid Box 170 Difference CDF of ENSO Precipitation Distributions. Bins 24, 48 and 72 from left to right.

Grid Box 170 (Figure 38) displays a consitently increasing trend for selected precipitation rate values. The 72 hour bin has the largest range of nearly 12 mm/day.

Grid boxes 348 and 371 (Figures 39-40) are located in the same positive spatially autocorrelated area south of Florida. The two grid boxes are diagonally adjacent and each are independently and spatially significant in regards to the El Nino and La Nina precipitation distributions. However, they display different rain rates at D (see Figure 31).

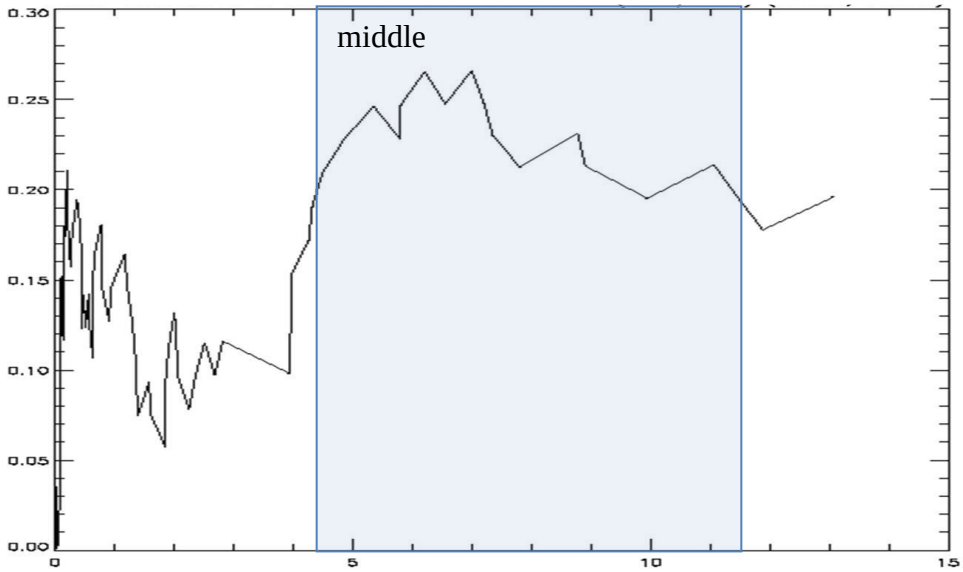

Precipitation (mm)

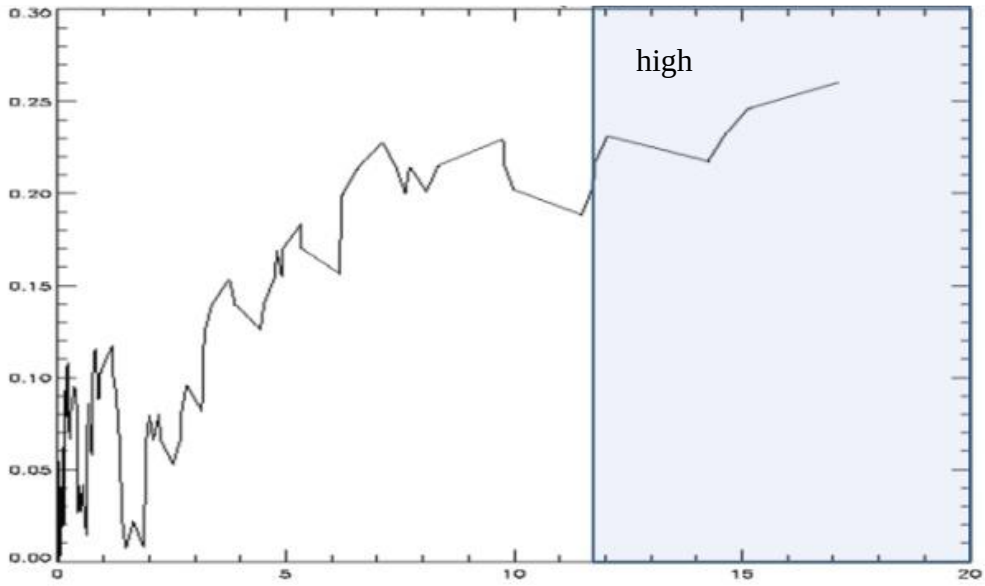

Precipitation (mm)

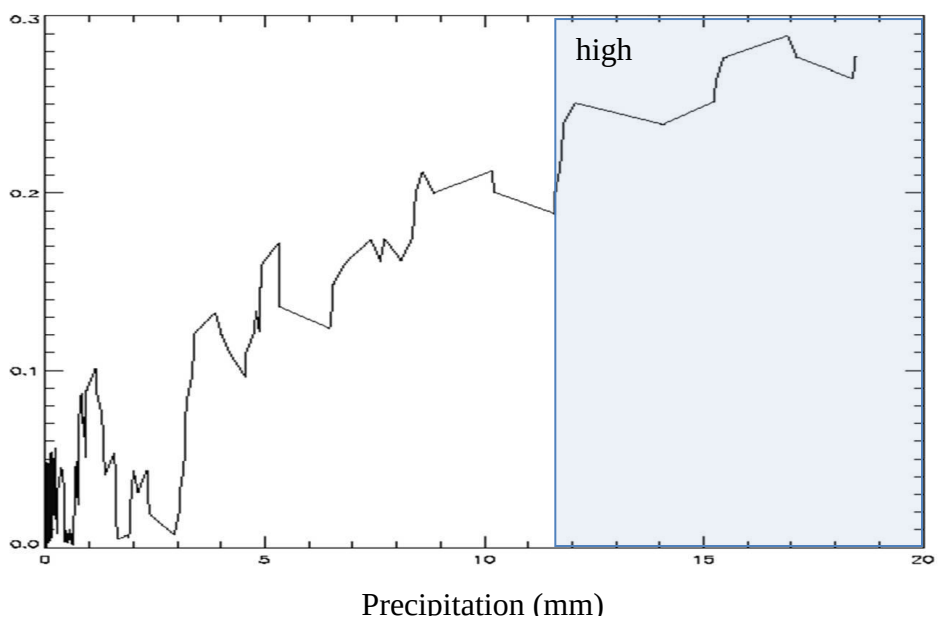

Figure 39. Grid Box 348 Difference CDF of ENSO Precipitation Distributions. Bins 24, 48 and 72 from left to right.

Grid box 348 (Figure 39) has the largest CDF difference with a shift to higher rain rates with increasing bin size. It is one of the most interesting difference CDFs as the greatest change in precipitation distributions corresponds to high rain rates, suggesting that ENSO is an important driver for precipitation in this area. La Nina produces ample precipitation with flooding a good possibility, while a lack of extreme precipitation during El Nino and subsequent drought is likely more of a concern.

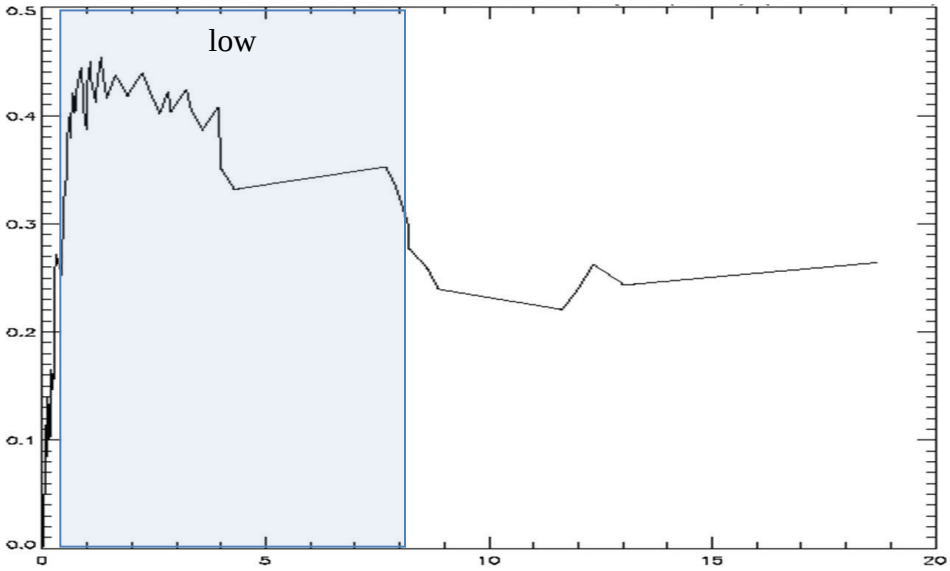

Precipitation (mm)

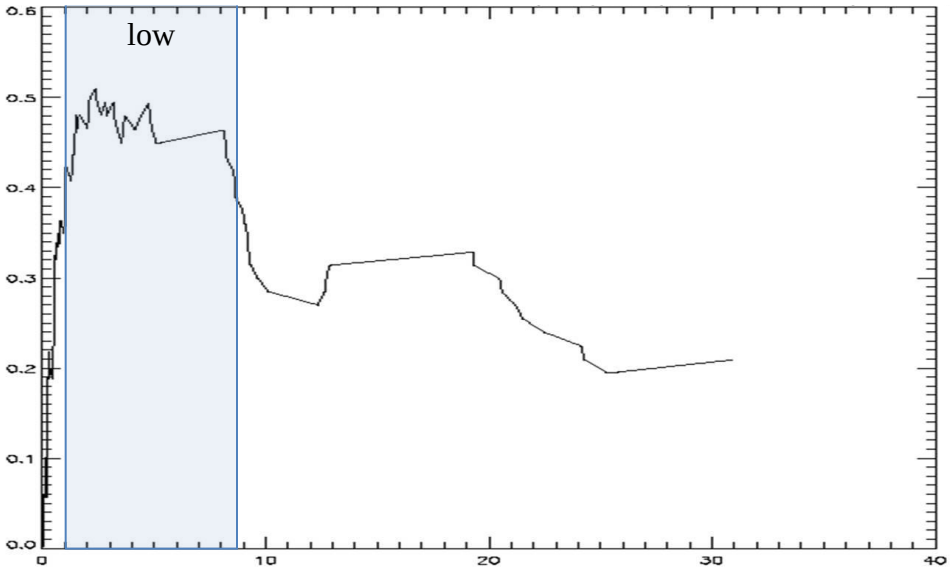

Precipitation (mm)

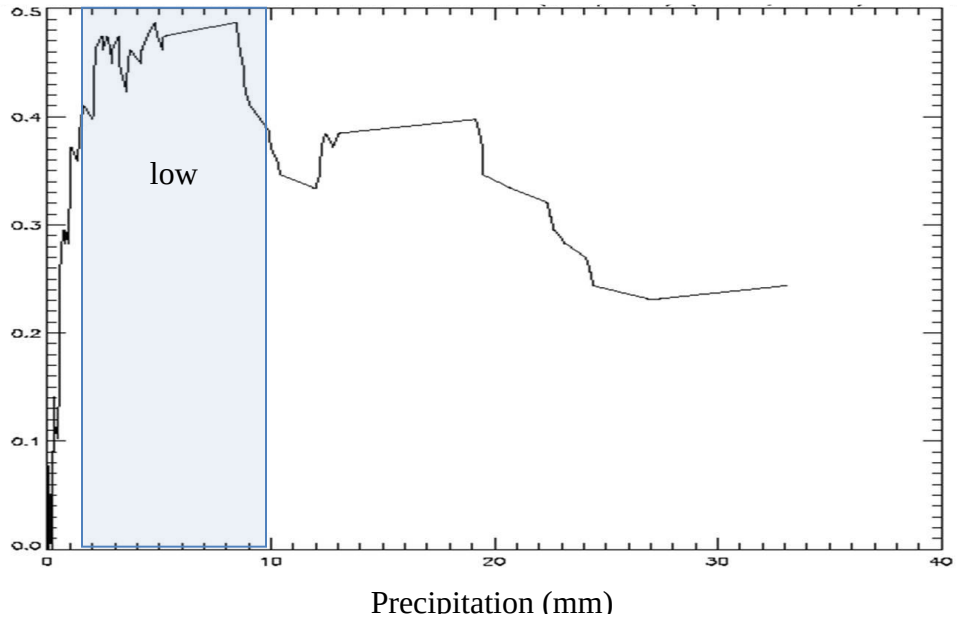

Figure 40. Grid Box 371 Difference CDF of ENSO Precipitation Distributions. Bins 24, 48 and 72 from left to right.

Grid box 371 CDF difference (Figure 40) shows the greatest separation at low precipitation rates with the high end of selected rates upwards of 9 mm/day at the 72 hour bin.

4.6.1 General CDF Observations

Red grid boxes (more La Nina extremes) tend to have the CDF difference maxima at higher values of precipitation and the range tends to expand towards higher precipitation rates with longer bins. This shift towards higher rain rates at red boxes may suggest more successive days of precipitation for La Nina. Unrelated, the highest D values for all grid boxes occurred at 48 or 72 hour bin sizes except for grid box 242 in October.

4.7 Synoptic Analysis

At each selected grid box, a synoptic analysis is performed to quantify the strength, tilt and location of the polar and subtropical jet streams at precipitation events that fall within the areas defined using the CDF difference plots. The following charts (Figures 41-48) describe the mean for strength, tilt and location of the polar and subtropical jet streams. Along the x-axis, grid boxes are coded; for grid box L_179 (D at low precipitation rates) and H_179 (D at high precipitation rates). All other grid boxes start with the number of the grid box, followed by an o = El Nino or a = La Nina.

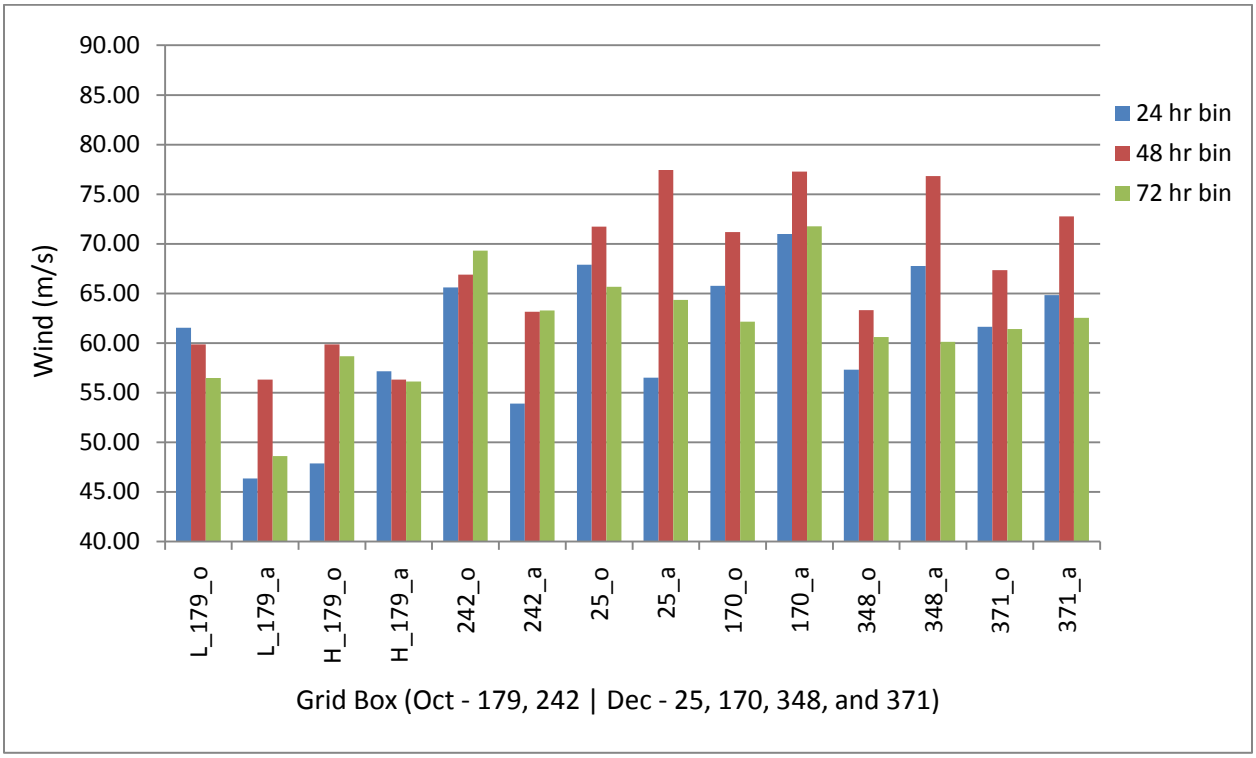

Figure 41. Trough Mean Maximum Wind Speed for 24, 48, and 72 Hour Bins.

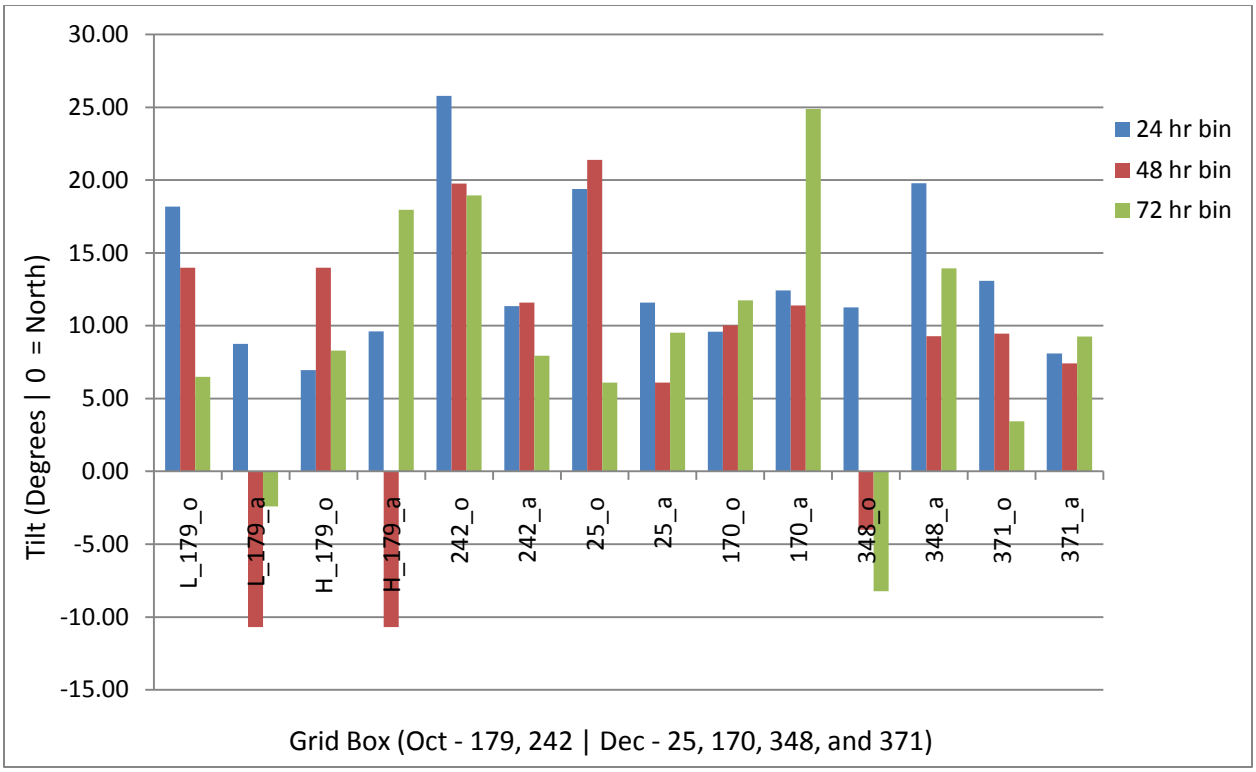

Figure 42. Trough Mean Tilt for 24, 48, and 72 Hour Bins.

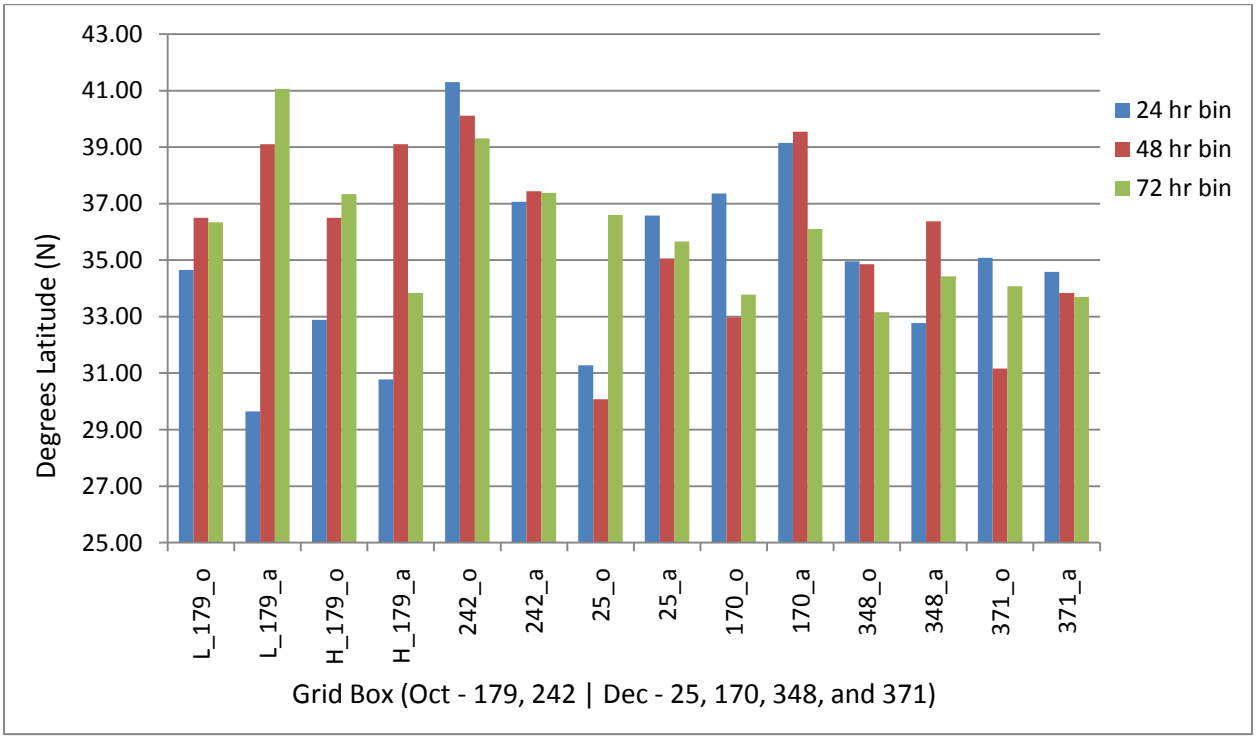

Figure 43. Trough Mean Location (Latitude) for 24, 48, and 72 hour bins.

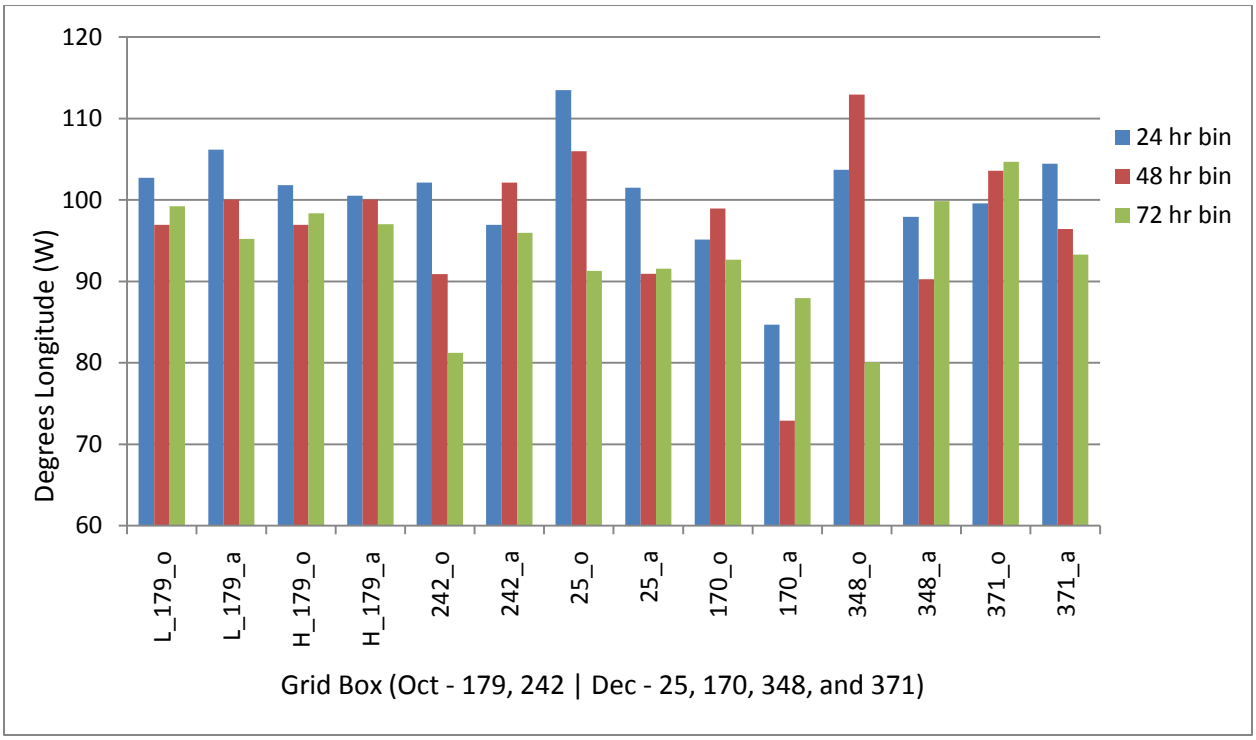

Figure 44. Trough Mean Location (Longitude) for 24, 48, and 72 hour bins.

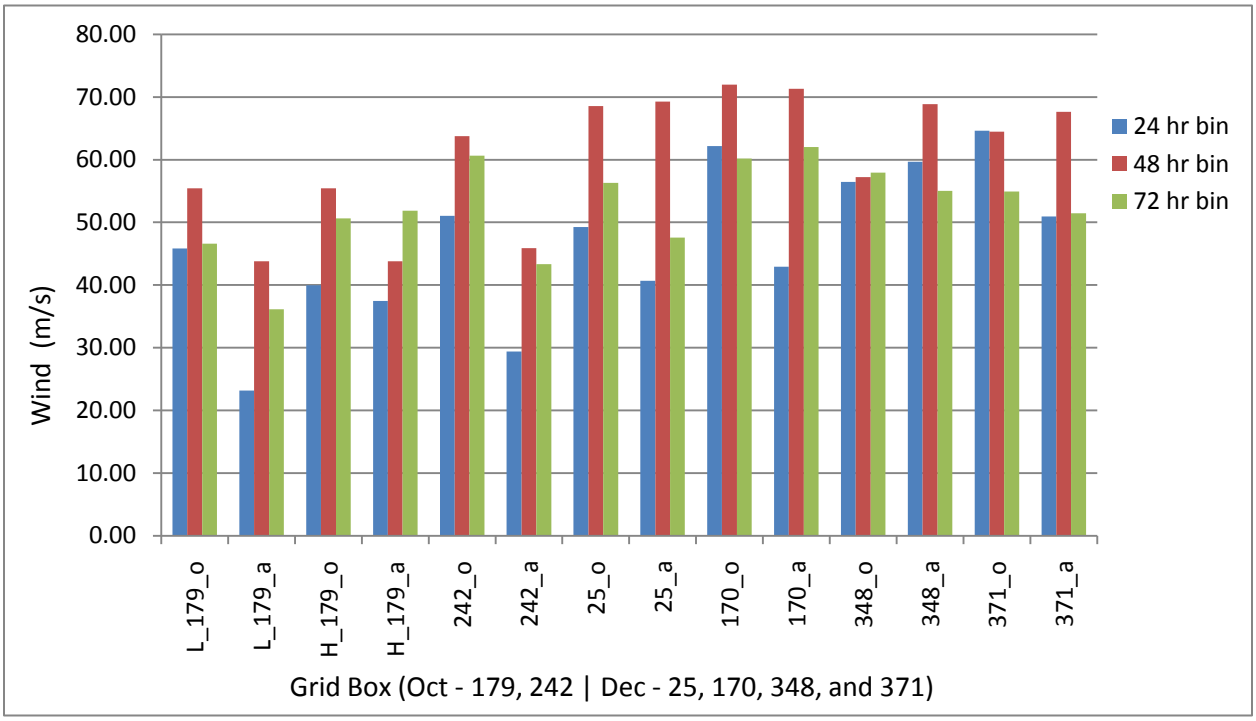

Figure 45. Subtropical Jet Mean Wind Speed for 24, 48, and 72 hour bins.

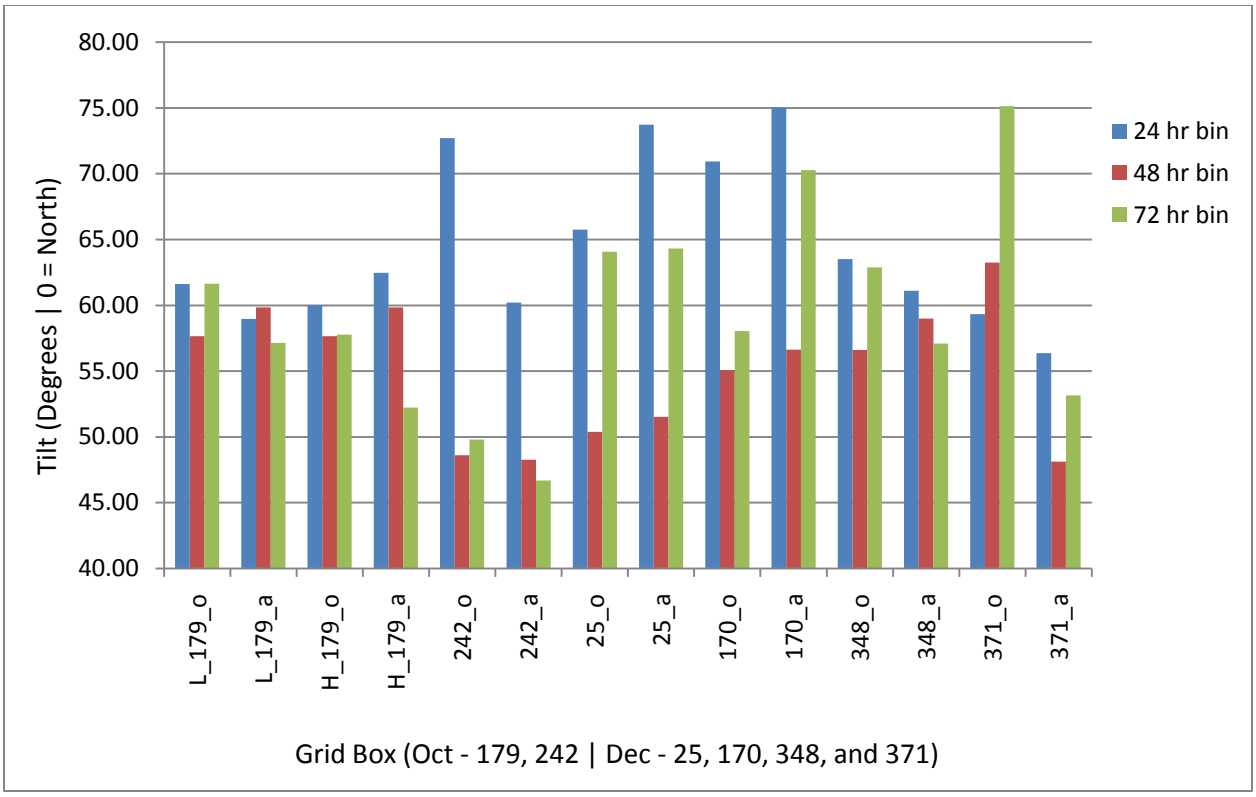

Figure 46. Subtropical Jet Mean Tilt for 24, 48, and 72 hour bins.

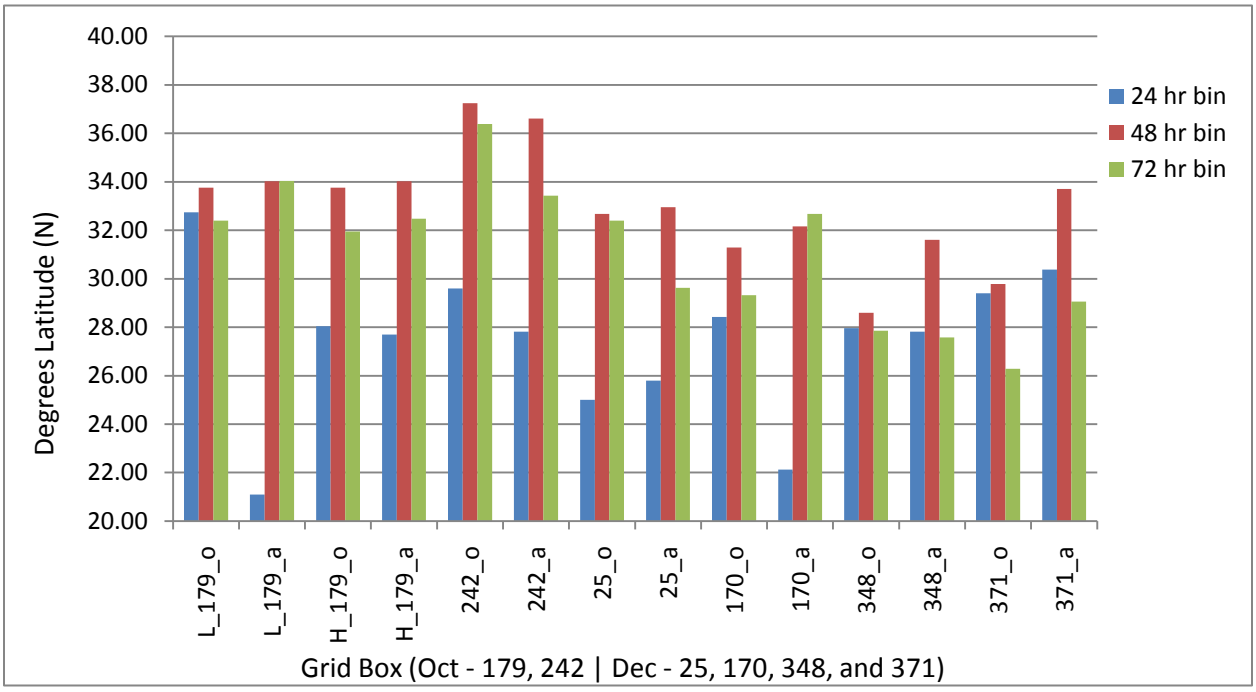

Figure 47. Subtropical Jet Mean Location (latitude) for 24, 48, and 72 hour bins.

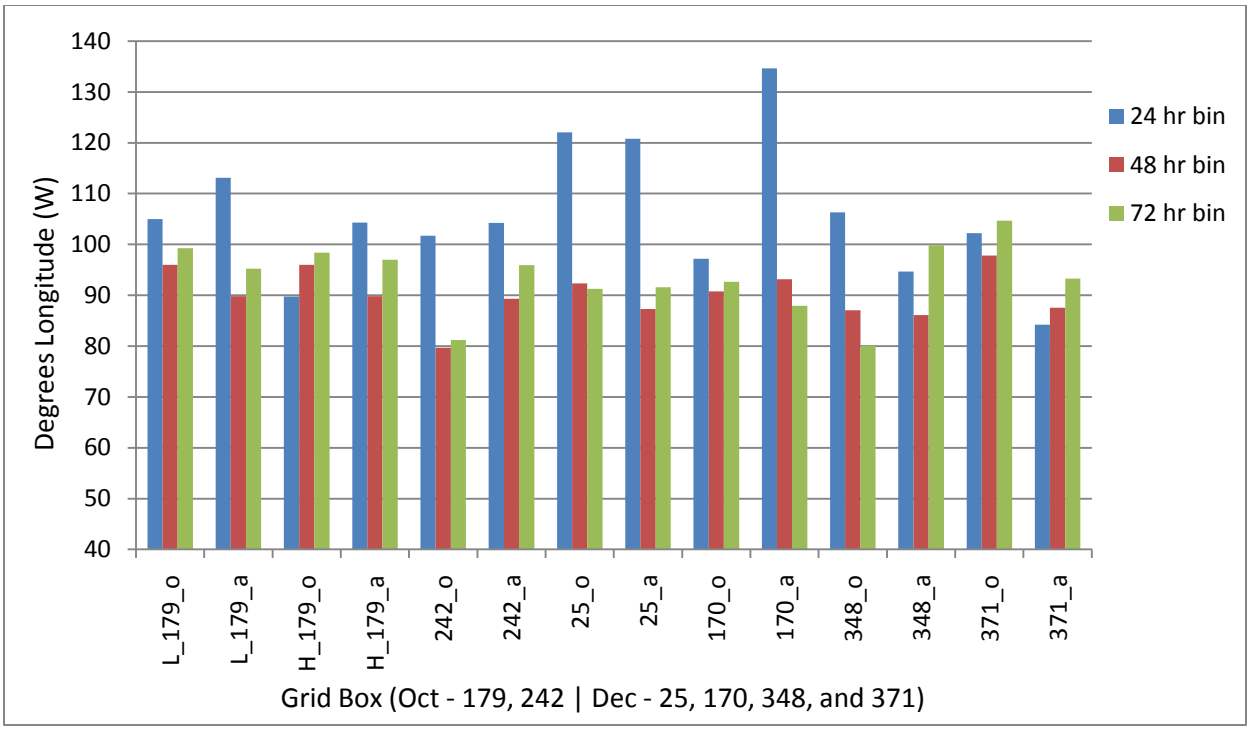

Figure 48. Subtropical Jet Mean Location (longitude) for 24, 48, and 72 hour bins.

4.7.1 The Polar Jet Stream

The polar jet max wind speeds (Figure 41) are generally higher during the month of December as compared to October. This is attributed to the equatorward movement and strengthening of the polar jet stream during the cold season. No apparent trends between ENSO composites are evident across all grid boxes. Grid boxes L_179, 242 and 25 disply noticeable decreases in maximum wind duing La Nina during the 24 hour bin. In fact grid L_179 is significantly different at the one percent level at the 24 hour bin, according to a two tailed T-test (Table 4). On the other hand, grid boxes H_179, 170, 348, and to a lesser extent 371 experience moderate increases in wind speed. Interestingly, for October the 24-hour bin seems to have the largest ENSO differences, but the 24 hour differences become comparable to the 48 and 72 hour differences in December. Also, grid boxes 348 and 371, which are similar spatially but represent

different rain rates, show similar changes in the maximum wind speed for each ENSO phase and bin size.

The polar jet tilt (Figure 42) at the nearest trough indicates a decrease in tilt during La Nina in October, while the tilt is mixed in December. Grid boxes 170 and 348 show a higher tilt for La Nina as compared to El Nino. Grid 179 (October) at the 48 hour bin is not only lower, but significantly different at the two percent level (Table 4).

The polar jet location measured in latitude and longitude (Figure 43, 44) are roughly the same for ENSO composites. The latitude chart displays a large discrepency between 24 and 48/72 hour bins upwards of 12 degrees latitude difference for grid box L_179_a. December is more consistent in this regard. The mean trough position longitudinally is consistently between about 90 to 100 degrees west for the month of October (Figure 44). In December there is considerably more variation in mean trough location from 80 to around 110 degrees west. Most interestingly, there is an eastern bias of the trough axis location during the La Nina months. In fact the 48 hour bin of grid 348 is significantly different at the one percent level (Table 4).

4.7.2 The Subtropical Jet Stream

The subtropical jet maximum wind speeds (Figure 45) exhibit one of the more interesting patterns of this synoptic analysis. For each grid box the wind speed during El Nino is greater than or approximately equal to the winds during La Nina at every bin length, with only a few exceptions. In fact, grid box 170 is significantly different at the ten percent level for the 24 hour bin (Table 5). Most notably, grid box 242 has significantly different subtropical jet maximum winds speeds at the one percent level at each bin length (Table 5).

Subtropical jet stream tilt (Figure 46) is highly variable. Other then grid 179, there is a large range of tilt values at different bins at individual grid boxes. So much so, that it is difficult to discern important patterns. For instance the 242 grid has the lowest values at the 48/72 hour bins, but also has nearly the highest 24 hour bin value in the El Nino composites. However one trend does emerge. The 48 hour bin is the minimum or near the minimum value for every grid box and has a relatively minimal change in values at each grid box.

The subtropical jet stream location displays no definitive trends for latitude (Figure 47), except a southward position of the subtropical jet at the 24 hour bin for grid boxes L_179, 242, and 170. At grid box L_179 for the 24 hour bin, the latitude is significantly different between El Nino and La Nina at the two percent level (Table 5). The longitudinal component of the subtropical jet stream (Figure 48) exhibits a neutral or westward shift during La Nina at all grid boxes except 348 and 371. In fact grid box 170 shows a significant difference between the longitude distributions of the opposing phases of ENSO (Table 5).

4.7.3 Synpotic Summary

Polar Jet Stream

Grid	Bin	Precip. Range	Max wind	tilt	Lat (N)	long (W)
179	L_24	Low	**15.19**	9.42	*5.00*	-3.47
	H_24	High	-9.27	-2.67	2.10	1.30
	48	Low	3.54	**24.69**	-2.60	-3.13
	L_72	Low	7.86	8.90	-4.72	-3.44
	H_72	High	2.53	-9.67	3.50	-0.88
242	24	Low	11.71	14.42	4.23	5.19
	48	Middle	3.74	8.18	2.68	*-11.27*
	72	Middle	6.02	11.01	1.93	*-9.69*
25	24	Middle	11.38	7.80	**-5.31**	11.98
	48	Middle	-5.71	15.30	-4.99	15.09
	72	Middle	1.31	-3.44	0.94	-18.06
170	24	Low	-5.22	-2.84	-1.79	10.43
	48	Middle	-6.08	-1.36	**-6.58**	26.07
	72	Middle	-9.61	-13.13	-2.32	1.75
348	24	Middle	*-10.46*	-8.53	2.19	5.79
	48	High	**-13.52**	-13.31	-1.51	**22.64**
	72	High	**0.47**	**-22.18**	-1.27	6.59
371	24	Low	-3.22	4.98	0.50	-4.85
	48	Low	-5.39	2.04	*-2.67*	7.18
	72	Low	-1.12	-5.82	0.37	-3.25

Table 4. Polar Jet Stream Synoptic Analysis Results. El Nino Minus La Nina. Grid numbers are color coded to reflect their origin: Blue = El Nino extremes | Red = La Nina extremes. Underlined and italized values indicate significance at ten percent level, bolded values indicate significance at the five percent level, and bolded and underlined values identify values significant at the two percent level for a two tailed T-Test.

The polar jet stream synoptic analysis (Table 4) for maximum winds shows a distinct trend between October and December. October displays a general increase in polar jet max winds during Ocotober. In December winds are slightly lower during El Nino. The December grid box 25 is the only exception with a large positive, though insignificant value at the 24 hour

bin. Interestingly at grid 348 all bins are significant and the 24 and 48 hour bins have large negative values, indicating a large increase in winds during La Nina. A general increase in winds from October to December agrees with climatology. The trough tilt shows no consistent trend over all grid boxes. Interestingly, of the two significantly different values, the October grid 179 has a larger tilt by 25 degrees at the 48 hour bin when El Nino has more extreme rain rates. December grid 348 has a large negative value meaning La Nina has a more negative tilt accompanying more extreme rain rates as compared to El Nino. No significant trend was observed for a displacement in latitude between ENSO phases. The longitudinal position showed a strong eastern bias for December La Nina composites. In contrast, October trended westward during La Nina composites. Note the contrast in longitudinal values between grid box 348 and 371. Despite their close proximity, the position of the polar jet during different phases of ENSO seems to vary greatly for the different precipitaiton rates.

In summary, there is a general trend towards a neutral tilt and eastern bias for the polar jet stream trough complexes during La Nina selected precipitation events. Often times a neutral to negative tilting trough results in a more robust wind field associated with the upper level jet stream. However the analysis of maximum winds near the trough does not support this theory.

Grid	Bin	Precip. Range	Max wind	tilt	Lat (N)	long (W)
179	L_24	Low	**22.65**	2.63	**11.64**	-8.16
	H_24	High	2.49	-2.47	0.35	-14.51
	48	Low	*11.65*	-2.19	-0.26	6.19
	L_72	Low	**10.46**	4.50	-1.65	4.03
	H_72	High	-1.20	5.54	-0.53	1.36
242	24	Low	**21.64**	12.50	1.78	-2.56
	48	Middle	**17.87**	0.36	0.63	-9.63
	72	Middle	**17.34**	3.11	2.96	**-14.73**
25	24	Middle	8.58	-7.97	-0.80	1.20
	48	Middle	-0.74	-1.15	-0.28	5.04
	72	Middle	8.73	-0.24	2.78	-0.28
170	24	Low	*19.27*	-4.11	6.30	*-37.49*
	48	Middle	0.66	-1.55	-0.88	-2.37
	72	Middle	-1.85	-12.23	-3.35	4.70
348	24	Middle	-3.21	2.40	0.14	11.63
	48	High	-11.61	-2.40	-3.01	0.98
	72	High	10.93	5.80	0.28	**-19.77**
371	24	Low	*13.71*	2.98	-0.98	*18.02*
	48	Low	-3.15	*15.13*	-3.93	10.26
	72	Low	3.44	**21.99**	-2.77	11.41

Table 5. Subtropical Jet Stream Synoptic Analysis Results. El Nino Minus La Nina. Grid numbers are color coded to reflect their origin: Blue = El Nino extremes | Red = La Nina extremes. Underlined and italized values indicate significance at ten percent level, bolded values indicate significance at the five percent level, and bolded and underlined values identify values significant at the two percent level for a two tailed T-Test.

Possibly the most intriguing result in this study is tied into the subtropical jet stream winds (Table 5). There is a decrease of maximum winds during the negative phase of ENSO at nearly every grid box at each bin length. In October six of the eight values are significant at the ten percent level, all positive increases suggesting El Nino has a strong postive correlation with subtropical jet stream winds. Exceptions to this trend are grids 348 and 371, which are located in the far southeast portion of the study area, the furthest from the mid-latitude westerlies. The tilt

shows an intriguing trend. Grid boxes that occur in areas where El Nino had less extreme rainfall display a decrease in tilt during El Nino, while grid boxes where La Nina had fewer extremes exhibited a decrease in tilt during La Nina. The latitude of the subtropical jet does not display a significant trend. Grid boxes 170 and 179 display a westward trend in the position of the subtropical jet. Grid 371 show an eastward progression to the jet stream during La Nina. In summary, there is a tendency for a slight westward progression and weakening of the subtropical jet during La Nina months. Interestingly the subtropical jet stream tilt is biased towards the phase of ENSO that produced the highest precipitation events at each bin. This suggests that a stronger north/south component to the subtropical jet stream results in higher precipitation events.

		Polar Jet					Subtropical Jet			
Grid	**Bin Size**	**Max wind**	**tilt**	**Latitude**	**Longitude**		**Max wind**	**tilt**	**Latitude**	**Longitude**
179	**L_24**	**0.008**	0.383	*0.092*	0.638		**0.016**	0.769	**0.012**	0.631
	H_24	0.795	0.248	0.254	0.841		0.701	0.864	0.808	0.486
	48	0.365	**0.020**	0.421	0.574		*0.093*	0.836	0.840	0.493
	L_72	0.157	0.419	0.129	0.644		**0.047**	0.695	0.548	0.612
	H_72	0.746	0.452	0.196	0.878		0.573	0.909	0.848	0.870
242	**24**	0.160	0.420	0.400	0.585		**0.009**	0.150	0.658	0.848
	48	0.477	0.484	0.411	*0.061*		**0.007**	0.971	0.820	0.240
	72	0.262	0.310	0.489	*0.078*		**0.007**	0.724	0.350	**0.036**
25	**24**	0.163	0.347	**0.036**	0.237		0.282	0.608	0.846	0.921
	48	0.313	0.778	0.145	0.165		0.922	0.904	0.924	0.675
	72	0.846	0.511	0.830	0.171		0.438	0.987	0.524	0.984
170	**24**	0.407	0.856	0.663	0.575		*0.076*	0.774	0.253	*0.054*
	48	0.178	0.904	**0.006**	0.150		0.908	0.819	0.737	0.750
	72	0.146	0.246	0.453	0.791		0.799	0.124	0.158	0.420
348	**24**	*0.067*	0.285	0.303	0.553		0.745	0.877	0.977	0.528
	48	**0.009**	0.217	0.561	**0.006**		0.155	0.849	0.439	0.924
	72	**0.020**	**0.000**	0.430	0.233		0.633	0.666	0.925	**0.041**
371	**24**	0.634	0.583	0.805	0.487		*0.053*	0.762	0.712	*0.054*
	48	0.373	0.783	*0.084*	0.176		0.671	*0.063*	0.108	0.160
	72	0.795	0.346	0.802	0.514		0.514	**0.000**	0.368	0.197

	Sign.	**Max wind**	**tilt**	**Latitude**	**Longitude**		**Max wind**	**tilt**	**Latitude**	**Longitude**
	10 %	4	2	4	3		8	2	1	4
	5 %	3	2	2	1		5	1	1	2
	2 %	3	2	1	1		4	1	1	0

Table 6. Synoptic Analysis T-Test Results. Underlined and italized values indicate significance at ten percent level, bolded values indicate significance at the five percent level, and bolded and underlined values identify values significant at the two percent level. Below the main table is a count of the number of grid boxes under each level of significance.

4.7.4 Individual Grid Box Significance

In addition to looking at overall difference values obtained from the synoptic analysis. A closer look at a T-Test statistics (Table 6) compares the relative importance between the tropics and extratropics. At first glance it is obvious that the maximum wind statistic is important, especially for the subtropical jet stream, where four of twenty values (twenty percent) are

significant at the two percent level and eight of twenty values (fourty percent) are significant at the ten percent level. Thus, El Nino instigates an increase in the speed of the subtropical jet, regardless of the days examined. This is especially true for October (179, 242) as compared to December. The polar jet stream maximum wind speed is a close second with three out of twenty values (fifteen percent) are significant at the two percent level. The location of the jet streams in the form of latitude and longitude contribute many significant T-Test statistics as well. Especially, the latitude and longitude of the polar jet stream and the longitude of the subtropical jet stream,where a combined ten of sixty values (seventeen percent) are significant at the ten percent level. Tilt has the least evidence towards a significant change between phases of ENSO using the T-Test statistic. Though at the polar jet stream, two of twenty (ten percent) of the tilt statistics are significant at the two percent level.

A few other patterns become obvious with close inspection of the T-Test values chart (Table 6). Grid box L_179 is significant for the 24 hour bin for maximum wind speed and latitude for both jet streams, combining for fifty percent of the variables examined. Grid 348 is significant at all bins for the polar jet stream maximum wind speed, which skews the totals found at the bottom of the chart (Table 6). Also interesting, that grid box 242 contributes three significant values at the one percent level to the subtropical jet stream maximum winds. Though this does skew the totals for the number of significant values similar to grid 348, it's not as much of a concern, as all but two grid boxes contribute at least one significant T-Test statistic to the total values.

Another trend between grids 348 and 371 becomes apparent. Notice how 348 (high rates of precipitation) has nearly all significant differences for the polar jet stream portion of the

synoptic analysis, while grid 371 (low rates of precipitation) has nearly all significant differences occuring for the subtropical jet stream synoptic analysis. This suggests that for ENSO forced precipitation over this region, low precipitation rates are predominately forced by changes in the subtropical jet, while high precipitation rates are caused by changes in the polar jet stream structure.

Actual	NINO		NINA		Actual		MONTHLY
	T. Storm	Hurricane	T. Storm	Hurricane	T. Storm	Hurricane	TOTAL
AUG	6	3	2	5	8	8	16
SEP	3	8	4	7	7	15	22
OCT	1	2	1	3	2	5	7
NOV	0	0	1	1	1	1	2
DEC	0	0	1	0	1	0	1
TOTAL	10	13	9	16	19	29	48

Adjusted	NINO		NINA	
	T. Storm	Hurricane	T. Storm	Hurricane
AUG	6	3	2.67	6.67
SEP	3	8	5.33	9.33
OCT	1	2	1	3
NOV	0	0	1	1
DEC	0	0	1	0
TOTAL	10	13	11	20

Table 7. ENSO Tropical Cyclone Count (Top). Adjusted Tropical Cyclones (Bottom).

4.7.5 Tropical Cylcones

4.7.5.a Summary

The ENSO tropical cyclone chart (Table 7) counts all tropical storms and hurricanes that occured during an ENSO month between 1997 and 2009 that intersect any part of the study region. The intensity is based off of the maximum strength reached during the tropical cyclones life cycle, disregarding intensity through the Gulf of Mexico region. From August through October the frequency of tropical cyclones is very similar between El Nino and La Nina composites. November and December yield a total of three tropical cyclones, three more then during El Nino during the same two months. Month by month frequency of tropical cyclones combining the two composites shows a typical distribution of tropical cyclones during the summer with a peak in activity in September (22), followed closely by August (16) and then falling off for the last three months of the year (7, 2, 1). Overall La Nina records two more tropical cyclones and three more hurricanes, in spite of a shorter composite.

Adjusting the tropical storm and hurricane frequency to account for difference in the number of months between ENSO phases further skews tropical cyclone activity towards La Nina months. Under the adjusted values (Table 7) notice that La Nina now has 7 more hurricanes, a 54 percent increase in hurricanes and 8 more tropical cyclones, a 35 percent increase. This points to a substantial influence from ENSO on tropical cyclone precipitation across the Gulf of Mexico region.

4.7.5.b Hurricane Irene – Grid 242

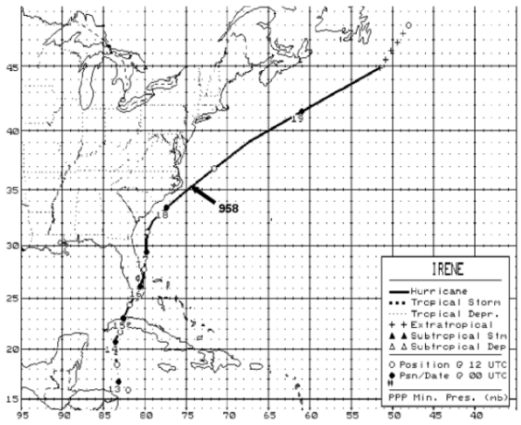

Figure 49. Hurricane Irene Storm Track. Courtesy of NOAA.

There was only one strom during October or December that significantly effected a grid boxed selected. Hurricane Irene (Figure 48) passed nearby grid box 242 October 15th and 16th 1999 during La Nina. The storm maxed out with winds of 95 knots and a minimum pressure of 958 millibars. The storm produced GPCP satellite estimated precipitation amounts of 105.7 mm/day, 131.5 mm in two days, and a storm total of 146 mm (5.75 inches) over a three day period. This single storm has a significant impact on the ENSO precipitation distribution. In October of 98, 99, 00, and 07 (La Nina months), this was the highest precipitation event by 43.8 mm. Even more impressive, this event beats out any El Nino event by almost 70 mm. Irene provide one example of how important tropical cyclones can be to precipitation distributions and providing needed water to humanity. The impact of Irene puts into question the results for grid box 242, as discussed in the synoptic analysis section of the discussion.

5. Discussion

Here the research questions are revisted and answered in order.

Research Questions

1) What are the changes in the precipitation distributions for ENSO events in the Gulf of Mexico region?

2) How do changes relate to:

a) characteristics of the subtropical jet streams

b) characteristics of polar jet streams

c) interaction of the jet streams

To address each research question each section of the results with be summarized while making some assertions as to the importance of each analysis towards better understanding ENSO in the Gulf of Mexico.

5.1 Precipitation Distributions

In addressing the first research question the independent grid box and spatial analysis of D values and the spatial analysis of precipitation rates are examined. Similar to Curtis (2007) and Ropelewski (1995) the Gulf of Mexico exhibits an ENSO signal which will be described below.

5.1.1 Independent Grid Box Analysis

The independent grid box analysis of D values from August through January provides important information about independent changes in precipitation. Displayed grid boxes are

significant at the five percent level. This contributes a ninety-five percent confidence that these grid boxes have received significantly different precipitation distributions between El Nino and La Nina.

At the 24 hour bin length there is a minimal number of grid boxes that are significant at any month. Most notably August, September and January all show little difference between the phases of ENSO except at a few select grid boxes. In October and December and to a lesser extent November this is far from the case, with large scale areas covered in significant grid boxes. At the 24 hour bin, and especially larger bins, spatial patterns between grid boxes becomes clear, even if it is not the sole purpose of the independent grid box analysis.

At larger bins, the number of significant grid boxes increases substantially and in October and December in particular, they continue to draw large regions of similar D values. The D values themselves also generally increase at larger bins. There are likely two mechanisms at work here. One, the temporal patterns of precipitation are likely different in each phase of ENSO. So, expanding the 24 hour bin to 48 and 72 hours will likely emphasize the precipitation distributions in the form of a changing D statistic. Two, and likely the stronger of the two forces at work, is an increase of the number of precipitation events due to the running 48 and 72 hour bins, effectively compounding the difference between the ENSO precipitation distributions.

5.1.1.a Trend of D Values

Looking at the D values as a whole, there is a decreasing trend for region-wide averaged D values. The standard deviation of D values also decreases markedly going into the cold season. We will explore this further in the next section.

5.1.2 Hotspot Analysis

5.1.2.a D Values

A hotspot analysis of the D values confirms what we already witnessed from the independent grid box analysis of D values. Large areas of positive spatial autocorrelation dominate the months of October and December. November in particular sticks out as it has relative poor spatial autocorrelation when compared with October and December. October and December have similar spatial patterns according to the hotspot analysis. Negative D values across the northern Gulf of Mexico into parts of the southern United States indicates that there are more extreme precipitation events and more precipitation during an El Nino, as shown by the mean precipitation hot spot analysis. In December another area of negative D values is centered over Florida, east into the adjacent portion of the Atlantic Ocean. Positive D values persist across the southeastern portion of the study region. In general negative D values (more extremes in El Nino) typically occurred over land while positive D values (more extremes in La Nina) persisted over water. November and January are outliers of this trend.

5.1.2.b Precipitation rate at D

As described earlier a northward trend and expansion of high rates of precipitation that occur at the D statistic occurs from August through December, with a slight regression southward in January. The beginning portion of this trend is likely sparked by tropical convection across the Gulf of Mexico in September and even into October. By November and especially December tropical disturbances are extremely rare. A possible cause for the migration of these high values into the northern Gulf of Mexico and eventually in the Texas Louisiana area is the formation of Gulf Lows and the establishment of a stronger and northward position of the subtropical jet stream across the region during El Nino, sometimes working in concert to produce

high precipitation events. The southward movement of high precipitation rates in January may be explained by a southward progression of the polar jet and associated polar high pressure systems.

5.2 Synoptic Analysis

5.2.1.a Jet Streams

Polar and subtropical jet streams experienced a significant change in position according to the synoptic analysis. Additionally, maximum wind speeds were strongly affected by the presence of ENSO. Subtropical jet stream winds are in particular faster during El Nino than La Nina. The only notable exceptions are grid boxes 348 and 371 which had the reverse effect. From a physical standpoint, ENSO forced changes in jet stream configurations seems all but certain.

Warming SSTs at the equator during El Nino does appear to increase max jet winds, likely from an influx of energy and increased interaction between the polar and subtropical jet streams. Furthermore, strong equator heating present during El Nino increases poleward energy transport in the subtropical jet and increases the likelihood of a single jet state (Lee and Kim 2003). Both of these mechanisms increase the likelihood of a stronger jet stream. A stronger jet subsequently fuels stronger and more frequent surface low pressure systems. This change in storm intensity, coupled with the tendency for a shift in position for both jet streams explains the changes in precipitation patterns across the region. This effectively mirrors the information gathered about the precipitation distributions for each grid box. There is a change in both precipitation distributions and jet stream strength and location.

5.2.1.b Grid Box Summary

Grid 179 is located on the coast of Texas and has a negative D, indicating that El Nino would have more extreme precipitation (denoted as; El Nino > La Nina). This is consistent with the faster jet. At the low precipitation end, the latitude of the subtropical jet shifts north, to a similar latitude as grid 179 further emphasizing the impact of the jet stream. Also, the polar jet and subtropical jet are in close proximity (latitude) suggesting interaction between the jets, which could lead to widespread light rain with an increased likelihood for heavy precipitation events.

Grid 242 is located on the west coast of Florida and has a positive D (La Nina > El Nino). This grid box has a strong increase in subtropical jet stream winds at all bin sizes at the one percent level. This is counterintuitive to the expected result. Typically a stronger jet results in heavier precipitation. A westward shift of both jet streams may be the culprit. More likely ENSO forced CDF distributions were skewed because of the extreme precipitation (105.7 mm) produced by Irene as discussed previously.

Grid 25 is located in North Texas and has a negative D (El Nino > La Nina). A slight increase in both jet stream max winds is evident, though neither distributions show a significant difference at any bin size. The polar jet stream shifts to the south in El Nino. The southward shift places the polar jet closer to this area and closer to the subtropical jet, increasing the likelihood of important precipitation during El Nino.

Grid 170 is located on the east coast of Florida and has a negative D (El Nino > La Nina). Subtropical jet strength is important, but the location is shifted far to the east in El Nino. Also notable, the polar jet shifts to the south, increasing the likelihood of a coupling of the jet streams. The increased jet stream winds and eastward movement of the subtropical jet stream along with a

southward progression of the polar jet stream increases the chances for large precipitation events in El Nino.

Grid 348 is located on the northern side of Cuba and has a positive D (La Nina > El Nino). This is the only grid box that displays no significant difference for subtropical jet stream winds. However, the polar jet stream is weaker in El Nino. This could in part, explain more extremes during La Nina.

Grid 371 is located on the southern side of Cuba and has a positive D (La Nina > El Nino). For this grid box there is no difference in the polar jet stream maximum winds. The subtropical jet is faster in El Nino. However, it is further west, away from the location. This may explain the decrease in extreme precipitation during El Nino.

Grid boxes 348 and 371 are an interesting case. They are diagonally adjacent in the same area of positive D values (La Nina > El Nino) but according to the synoptic analysis precipitation at the high precipitation range (348) and low precipitation range (371) have different atmospheric drivers. At Grid box 348, polar jet changes significantly for maximum winds, tilt, and longitudinal position while there is little change to subtropical jet stream components. In contrast, grid box 371 shows a significant difference in subtropical jet stream maximum winds, tilt, and longitude.

This may somehow be related to the position of the grid boxes on either side of Cuba. Grid box 348 is exposed to the north making the progression of cold fronts and associated precipitation important. Conversely, the large mountain range to the north of grid box 371 may reduce the impact from cold fronts related to the polar front, while exposing the area to subtropical jet stream induced precipitation.

5.2.2 Tropical Cyclones

Tropical disturbances produce copious amounts of precipitation over the time scale that is investigated in this research. From August through December nearly the same number of tropical cyclones occurred in each phase of ENSO. However, La Nina experienced three more hurricanes and two more tropical cyclones despite fewer La Nina ENSO months. The adjusted numbers magnify the difference between La Nina and El Nino, contributing seven more hurricanes and eight more tropical cyclones during La Nina. This strong bias for large scale tropical precipitation events during the late summer for La Nina may explain the spatial patterns during this time. It may also partially explain the discontinuity in spatial patterns of precipitation shifting from the warm to cold season.

5.3 Conclusion

The independent grid box and spatial analysis, synoptic analysis and tropical cyclone frequency work in concert to describe ENSO forced changes in precipitation distributions.

The independent grid box and spatial analysis of the D values and of the precipitation rates creates a picture of the areas influenced the greatest by ENSO. Understanding these precipitation distributions at each grid box and spatially are paramount to understanding what large scale systems(s) may be responsible for the ENSO signal. The spatial analysis of precipitation rates at D, coupled with synoptic scale analysis provides telling clues from October through January. The northward progression of high rates of precipitation across an area with higher El Nino extremes suggests heavy precipitation events occur more often and are more important for describing differences between the two phases of ENSO. Increased winds of the

subtropical jet suggest a more active weather pattern during El Nino, resulting in increased precipitation over areas impacted the greatest by the mid-latitude westerlies.

Precipitation rates at D display a trend of northward progression in heavy rainfall. A possible explanation for this is the poleward movement of the subtropical jet. In December the area of high precipitation rates stall and move slightly southward in January. This area coincides with a southern storm track (Gulf Lows) which may be favored during El Nino possibly due to a more active subtropical jet stream.

This provides explanation for much of the cold season, but it does not explain patterns found in the late summer. This is where the tropical cyclone frequency becomes important. In August an area of positive D values are present in the independent grid box and spatial analysis. In September a similar area appears off the east coast. Tropical disturbances are prevalent in both areas. The signal likely shows up because a high frequency of intense storms moved through the region skewing the CDF of the La Nina precipitation distributions at these locations towards higher precipitation rates. The overall Moran's I is weaker in August and September, correctly indicating that the spatial patterns of precipitation are more variable than October or December. One explanation could be the sporadic nature of warm season convection in general.

The transition to stronger spatial trends in October, or a greater difference in ENSO phases over large areas, may be due to a general lack of precipitation during La Nina across the region with a limited tropical precipitation signal. By November there is a weak trend spatially. This could be related to the progression of cold fronts that generally produce small scale (spatial and temporal) light precipitation events every few days/weeks. Another argument might be that the progression of the subtropical jet stream poleward and the polar jet stream equatorward

during this month dilutes the overall signal over a larger area. Both theories are supported by the hotspot analysis of D values, with the large area of blue (El Nino > La Nina extremes) values spread across the eastern half of the study region for November. By December tropical cyclones are all but out of the picture. The polar jet stream and subtropical jet stream become more active over the region as evidenced by the stronger winds for selected December grid boxes. This is likely accompanied by an increase in the frequency of extra-tropical cyclone development and movement across the northern tier of the study region.

5.3.1 Final Remarks

The general findings described here indicate that ENSO forced changes at the synoptic scale during the warm and cold season impact precipitation distributions at smaller scales, both locally and spatially. This has important implications for local emergency management. People are largely susceptible to seasonal changes in precipitation. Seasonal averages and individual storm contributions are important towards economic and hazard preparation. Finally, changes in global and regional circulations and precipitation distributions forced by ENSO may provide an analogue to describe potential changes in a warming climate. This may in turn help people adapt for future changes in climate.

References:

Allan, R. P., and B. J. Soden. 2008. Atmospheric Warming and the Amplification of Precipitation Extremes. *Science*. 321: 1481-1484. DOI: 10.1126/science.1160787.

Allen, R. M., and W. J. Ingram. 2002. Constraints on Future Changes in Climate and the Hydrologic Cycle. *Nature*. 419: 224-232.

Adler, R.F., G.J. Huffman, A. Chang, R. Ferraro, P. Xie, J. Janowiak, B. Rudolf, U. Schneider, S. Curtis, D. Bolvin, A. Gruber, J. Susskind, and P. Arkin, 2003: The Version 2 Global Precipitation Climatology Project (GPCP) Monthly Precipitation Analysis (1979-Present). *Journal of Hydrometeorology*. 4,1147-1167.

Anselin, Luc, 2003: GeoDa 0.9 User's Guide. *Spatial Analyst Laboratory*. 1-115.

Arkin, P. A. 1982. The Relationship between Interannual Variability in the 200 mb Tropical Wind Field and the Southern Oscillation. *Monthly Weather Review*. 110: 1393-1404.

Arkin, P. A., and B. N. Meisner. 1987. The Relationship between Large-Scale Convective Rainfall and Cold Cloud over the Western Hemisphere 1982–1984. *Monthly Weather Review.* 115 (1): 51-74.

Bjerkness, J. 1969. Atmospheric teleconnections from the equatorial Pacific. *Monthly Weather Review.* 97: 163-172

Cayan, D.R., K. T. Redmond, and L. G. Riddle. 1999. ENSO and Hydrologic Extremes in the Western United States. *Journal of Climate*. 12: 2881-2893.

Curtis, S. 2006. Developing a Climatology of the South's 'Other' Storm Season. *Southeastern Geographer*. 46 (2): 231-244.

Curtis, S., A. Salahuddin, R. F. Adler, G. J. Huffman, G. Gu, and Y. Hong. 2007. Precipitation Extremes Estimated by GPCP and TRMM: ENSO Relationships. *Journal of Hydrometeorology*. 8 (4): 678-689. DOI: 10.1175/JHM601.1.

Eichler, T. and W. Higgins. 2006. Climatology and ENSO-Related Variability of North American Extratropical Cyclone Activity. *Journal of Climate*. 19 (10): 2076-2093.

Gastineau, G., Li L. and H. Le Treut. 2009. The Hadley and Walker Circulation Changes in Global Warming Conditions Described by Idealized Atmospheric Simulations. *Journal of Climate.* 22:14, 3993-4013.

Gershunov, A., and T. P. Barnett. 1998. ENSO Influence on Intraseasonal Extreme Rainfall and Temperature Frequencies in the Contiguous United States: Observations and Model Results. *Journal of Climate*. 11 (7): 1575-1586.

Held, I. M., and A. Y. Hou. 1980. Nonlinear Axially Symmetric Circulations in a Nearly Inviscid Atmosphere. *Journal of the Atmospheric Sciences*. 17: 515-533.

Hoerling, M., and Arun Kumar. 2003. The Perfect Ocean for Drought. *Science*. 299: 691.

Horel, J. D., and J. M. Wallace. 1981. Planetary-Scale Atmospheric Phenomena Associated with the Southern Oscillation. *Monthly Weather Review*. 109: 813-829.

Huffman, G. J., R. F. Adler, M. M. Morrissey, S. Curtis, R. Joyce, B. McGavock, J. Susskind. 2001. Global Precipitation at One-Degree Daily Resolution from Multisatellite Observations. Journal of Hydrometeorology. 2 (1): 36-50.

Huffman, G.J., R.F. Adler, D.T. Bolvin, G. Gu, E.J. Nelkin, K.P. Bowman, Y. Hong, E.F. Stocker, D.B. Wolff, 2007: The TRMM Multi-satellite Precipitation Analysis: Quasi-Global, Multi-Year, Combined-Sensor Precipitation Estimates at Fine Scale. *Journal of Hydrometeorology*, 8(1), 38-55.

Kalnay, E., M. Kanamitsu, R. Kistler, W. Collins, D. Deaven, L. Gandin, M. Iredell, S. Saha, G. White, J. Woollen, Y. Zhu, M. Chelliah, W. Ebisuzaki, W. Higgins, J. Janowiak, K. C. Mo, C. Ropelewski, J. Wang, A. Leetmaa, R. Reynolds, R. Jenne, and D. Joseph. 1996. The NCEP/NCAR 40-year reanalysis project. *Bulletin of the American Meteorology Society*. 77 (): 437–471

Kumar, A., and M. P. Hoerling. 1998. Annual Cycle of Pacific-North American Seasonal Predictability Associated with Different Phases of ENSO. *Journal of Climate*. 11 (12): 3295-3308.

Lee, S., and H. Kim. 2003. The Dynamical Relationship between Subtropical and Eddy-Driven Jets. *Journal of the Atmospheric Sciences*. 60 (12): 1490.

L'Heureux, M. L., and D. W. J. Thompson. 2006. Observed Relationships between the El Nino-Southern Oscillation and the Extratropical Zonal-Mean Circulation. *Journal of Climate*. 19 (2): 276-287.

Lu, J., Chen, G., and D. M. W. Frierson. 2008. Response of the Zonal Mean Atmospheric Circulation to El Niño versus Global Warming. *Journal of Climate*. 21:22, 5835-5851.

Mantua, N. J., S. R. Hare, Y. Zhang, J. M. Wallace, and R.C. Francis. 1997. A Pacific Interdecadal Climate Oscillation with Impacts on Salmon Production. *Bulletin of the American Meteorological Society*. 78: 1069-1079.

McKee, T. B., N. J. Doesken, and J. Kleist, 1993. The Relationship of Drought Frequency and Duration to Time Scales. *Preprints, 8th Conference on Applied Climatology, 17-22 January, Anaheim, CA*. 179-184.

Meehl, G. A., F. Zwiers, J. Evans, T. Knutson, L. Mearns, and P. Whetton. 2000. Trends in Extreme Weather and Climate Events: Issues Related to Modeling Extremes in Projections of Future Climate Change. *Bulletin of the American Meteorologic Society*. 81 (3): 427-436.

Rasmusson, E. M., and T. H. Carpenter. 1982. Variations in Tropical Sea Surface Temperature and Surface Wind Fields Associated with the Southern Oscillation/El Nino. *Monthly Weather Review*. 110: 354-384.

Ropelewski, C.F., and M.A. Bell, 2008: Shifts in the Statistics of Daily Rainfall in South America Conditional on ENSO Phase. *Journal of Climate*, 21 (5): 849–865.

Ropelewski, C. F., and M. S. Halpert. 1986. North American Precipitation and Temperature Patterns Associated with the El Nino/Southern Oscillation (ENSO). *Monthly Weather Review*. 114 (12): 2352-2362.

Ropelewski, C. F., and M. S. Halpert. 1987. Global and Regional Scale Precipitation Patterns Associated with the El Nino/Southern Oscillation. *Monthly Weather Review*. 115 (8): 1606-1626.

Ropelewski, C. F., and M. S. Halpert, 1989: Precipitation patterns associated with the high index phase of the Southern Oscillation. *Journal of Climate*, 2, 268-284.

Ropelewski, C. F., and M. S. Halpert. 1996. Quantifying Southern Oscillation-Precipitation Relationships. *Journal of Climate*. 9 (5): 1043-1059.

Seager, R., N. Harnik, Y. Kushnir, W. Robinson, and J. Miller. 2003. Mechanisms of Hemispherically Symmetric Climate Variability. *Journal of Climate*. 16 (18): 2960-2978.

Son, S.-W., and S. Lee. 2005. The Response of Westerly Jets to Thermal Driving in a Primitive Equation Model. *Journal of Atmospheric Sciences*. 62 (10): 3741-3757.

Susskind, J., P. Piraino, L. Iredell, and A. Mehta. 1997. Characteristics of the TOVS Pathfinder Path A Dataset. *Bulletin of the American Meteorological society*. 78 (7): 1449-1472.

Wentz, F. J., L. Ricciardulli, K. Hilburn, and C. Mears. 2007. How Much More Rain Will Global Warming Bring? *Science*. 317: 233-235. DOI: 10.1126/science.1140746.

Zhang, Y., J.M. Wallace, and D.S. Battisti. 1997. ENSO-like Interdecadal Variability. *Journal of Climate*. 10: 1004-1020.

Zipser, E. J., D. J. Cecil, C. Liu, S. W. Nesbitt, and D. P. Yorty. 2006. Where are the Most Intense Thunderstorms on Earth? *Bulletin of the American Meteorological Society*. 87 (8): 1057-1071.